Evidence for a Positive Tropical High-Cloud Feedback

Dissertation
with the aim of achieving a doctoral degree
at the Faculty of Mathematics, Informatics and Natural Sciences
Department of Earth System Sciences
at Universität Hamburg

submitted by
Jakob Emanuel Deutloff

Hamburg 2026

Department of Earth System Sciences

Date of Oral Defense:
Reviewers:
Members of the Examination Commission:

ABSTRACT

The overarching goal of this thesis is to improve the understanding of the tropical high-cloud feedback and thereby reduce uncertainty in climate sensitivity. Limited understanding of cloud feedbacks remains the main source of uncertainty in climate sensitivity, and the feedback from tropical high clouds is the least constrained. Progress in narrowing down the uncertainty of cloud feedbacks has been slow, also because of the crude representation of clouds in conventional general circulation models and the limited availability of satellite observations. General circulation models with horizontal grid spacings of $\mathcal{O}(100\ \mathrm{km})$ do not resolve individual clouds or convection, and reliable satellite observations of cloud thickness require co-located radar and lidar measurements, which are sparse.

My analysis is based on recent advancements in climate modelling and satellite data analysis that allow me to resolve the full spectrum of tropical high clouds by cloud thickness. I use global storm-resolving simulations with a horizontal grid spacing of $\mathcal{O}(1\ \mathrm{km})$ that simulate convection explicitly. In addition, I use satellite observations of cloud thickness, which became widely available thanks to machine learning algorithms that retrieve cloud thickness from passive satellite observations. I conduct three aquaplanet simulations at different global mean surface temperatures and evaluate their results against internal variability in satellite observations of cloud thickness.

I find that the tropical high-cloud feedback is positive, rather than negative as previously expected. The positive tropical high-cloud feedback that I find consists of three components, ranging from previously expected to newly identified: a positive feedback from the isothermal rise of all high clouds to higher altitude, a small feedback from the reduction of anvil-cloud amount, and a positive feedback from a change in the diurnal cycle of deep convection. That the high-cloud altitude feedback is positive is a scientific consensus, but I show that it is stronger than previously expected due to the unrealistic treatment of ozone in general circulation models. It was debated for more than two decades whether the anvil-cloud amount feedback is negative, but I find it to be small. A negative feedback from the reduction of thin, warming clouds is cancelled by a positive feedback from the reduction of thick, cooling clouds. Part of the tropical deep convection shifts from day to night in response to surface warming, causing a decrease in albedo and hence a positive feedback. Overall, my results imply a higher climate sensitivity. When updated for my estimate of the tropical high-cloud feedback, the central estimate of the World Climate Research Programme for the global warming that results from a doubling of atmospheric $\mathrm{CO_2}$ increases from 3.1 K to 4.3 K.

Resolving the spatial scale of individual clouds and the temporal scale of the diurnal cycle proves vital for understanding why the tropical high-cloud feedback is positive. It is necessary to capture that thin clouds are warming, and thick clouds are cooling the Earth, to understand why the anvil-cloud amount feedback is small. It is necessary to resolve deep convection and its diurnal cycle to capture the positive feedback from changes in the diurnal cycle of deep convection.

ZUSAMMENFASSUNG

Das übergeordnete Ziel meiner Arbeit ist es, die Rückkopplung hoher Wolken in den Tropen auf die Erderwärmung besser zu verstehen und dadurch die Unsicherheit der Klimasensitivität zu verringern. Nach wie vor stellt das begrenzte Verständnis von Wolkenrückkopplungen die Hauptquelle dieser Unsicherheit dar, wobei die Rückkopplung von hohen Wolken in den Tropen als am schlechtesten verstanden gilt. Fortschritte bei der Reduktion dieser Unsicherheit sind bislang nur langsam erzielt worden. Dies ist unter anderem auf die grobe Darstellung von Wolken in allgemeinen Zirkulationsmodellen sowie auf die begrenzte Verfügbarkeit geeigneter Satellitenbeobachtungen zurückzuführen. Allgemeine Zirkulationsmodelle mit einem horizontalen Gitterabstand von $\mathcal{O}(100\ \mathrm{km})$ können einzelne Wolken und konvektive Prozesse nicht auflösen, während präzise Beobachtungen der Wolkendicke Radar- und Lidar-Messungen erfordern, die nur eingeschränkt verfügbar sind.

Meine Analyse baut auf jüngsten Fortschritten in der Modellierung und Satellitenauswertung auf, die es ermöglichen, das gesamte Spektrum von hohen tropischen Wolken zu erfassen. Hierfür nutze ich globale, sturmauflösende Simulationen mit einem horizontalen Gitterabstand von $\mathcal{O}(1\ \mathrm{km})$, in denen Konvektion explizit dargestellt wird. Ergänzend verwende ich Satellitenbeobachtungen der Wolkendicke, die dank maschinellem Lernen aus passiven Messungen abgeleitet werden können und daher in großer Zahl verfügbar sind. Ich führe drei Aquaplanet-Simulationen mit unterschiedlichen mittleren Oberflächentemperaturen durch und teste die Ergebnisse anhand der internen Variabilität in den Satellitenbeobachtungen.

Meine Ergebnisse zeigen, dass die Rückkopplung hoher tropischer Wolken positiv ist, was im Gegensatz zu früheren Annahmen steht. Diese positive Rückkopplung setzt sich aus drei Komponenten zusammen, mit in dieser Reihenfolge abnehmender Erwartbarkeit: Erstens ergibt sich eine positive Rückkopplung durch den isothermen Aufstieg hoher Wolken in größere Höhen. Zweitens zeigt sich eine schwache Rückkopplung infolge einer Abnahme der Ambosswolken. Drittens entsteht eine weitere positive Rückkopplung durch Veränderungen im Tageszyklus der tiefen Konvektion. Die positive Rückkopplung durch den isothermen Aufstieg hoher Wolken entspricht dem wissenschaftlichen Konsens; meine Ergebnisse deuten jedoch darauf hin, dass diese Rückkopplung aufgrund der vereinfachten Ozon-Darstellung in herkömmlichen allgemeinen Zirkulationsmodellen bislang unterschätzt wurde. Es wurde seit über zwei Jahrzehnten diskutiert, ob die Rückkopplung durch eine Abnahme der Ambosswolken negativ ist, aber meine Ergebnisse zeigen, dass sie schwach ist. Eine negative Rückkopplung resultierend aus der Abnahme dünner, wärmender Wolken wird weitgehend durch eine positive Rückkopplung resultierend aus der Abnahme dicker, kühlender Wolken kompensiert. Darüber hinaus verschiebt sich ein Teil der tropischen Tiefkonvektion im Zuge der Erwärmung von den Tages- in die Nachtstunden. Diese Verschiebung führt zu einer Verringerung der Albedo und damit zu einer zusätzlichen positiven Rückkopplung. Insgesamt weisen meine Ergebnisse somit auf eine höhere Klimasensitivität hin. Unter Berücksichtigung meiner Abschätzung der Rückkopplung von hohen tropischen Wolken erhöht sich der zentrale Schätzwert

des World Climate Research Programme für die Erwärmung resultierend aus einer Verdopplung des atmosphärischen CO_2 von 3,1 K auf 4,3 K.

Die Auflösung der räumlichen Skala einzelner Wolken und der zeitlichen Skala des Tageszyklus erweist sich als entscheidend für das Verständnis, warum die Rückkopplung durch hohe tropische Wolken positiv ist. Es ist notwendig zu erfassen, dass dünne Wolken die Erde wärmen und dicke Wolken sie kühlen, um zu verstehen, warum die Rückkopplung durch eine Abnahme der Ambosswolken gering ist. Es ist notwendig, die tiefe Konvektion und ihren Tageszyklus aufzulösen, um die positive Rückkopplung durch Veränderungen im Tageszyklus der tiefen Konvektion zu erfassen.

PUBLICATIONS

The following four first-author publications are part of this thesis and included in the appendix:

J. Deutloff, S. A. Buehler, M. Brath, and A. K. Naumann (2025a). "Insights on Tropical High-Cloud Radiative Effect From a New Conceptual Model." In: *Journal of Advances in Modeling Earth Systems* 17.2, e2024MS004615. DOI: 10.1029/2024MS004615

J. Deutloff, S. A. Buehler, J. Windmiller, and A. K. Naumann (2026a). "Facets of the Tropical High-Cloud Feedback in a Global Storm-Resolving Model." Preprint, under revision at npj Climate and Atmospheric Science. DOI: 10.21203/rs.3.rs-9133974/v1

J. Deutloff, S. A. Buehler, J. Windmiller, and A. K. Naumann (2026b). "Observed Diurnal Cycle Change of Tropical Deep Convection Amplifies Surface Warming." Preprint, under revision at Nature Geoscience. DOI: 10.21203/rs.3.rs-9293749/v1

J. Deutloff, S. A. Buehler, J. Windmiller, and A. K. Naumann (2026c). "Weak Positive Feedback from Observed Reduction of Tropical Anvil Clouds." In preparation

As a PhD student, I contributed to two further publications. The first one is a first-author publication based on the results from my master's thesis. The second one describes the persistent EarthCare underflight studies of the ITCZ and organized convection (PERCUSION) measurement campaign, which I participated in. I operated the radar and radiometers onboard the HALO aeroplane, processed the data and led one flight as a principal investigator.

J. Deutloff, H. Held, and T. M. Lenton (2025b). "High probability of triggering climate tipping points under current policies modestly amplified by Amazon dieback and permafrost thaw." In: *Earth System Dynamics* 16.2, pp. 565–583. DOI: 10.5194/esd-16-565-2025

Windmiller et al. (2026). "PERCUSION's contribution to ORCESTRA". In preparation.

ACKNOWLEDGMENTS

Many people have contributed to my work, enabled me to work, and made my PhD a good experience, which might be most important.

I thank my supervisors, who I am lucky enough to have plenty of. Stefan has been the constant throughout my PhD, who was there from the beginning to the end. I learned a lot from Stefan about the climate and the right amount of pragmatism in science. I thank Ann Kristin for her continued support, even though she had to move to Munich in the middle of my PhD. She guided my initial ideas and was always the first to give me feedback on any draft. Julia adopted me in the middle of my PhD under the condition that I should start using observations, which turned out to be a great idea. I am thankful for her advice and her empathy. I felt very well supervised throughout my PhD and want to thank all my supervisors for making so many cool things possible. Highlights are the ORCESTRA campaign and my research stay in Australia, but they also gave me the freedom to work on my own terms, which I very much appreciate. I also thank Johanna for chairing my panel and keeping a good overview.

I received a lot of technical and administrative support that I am thankful for. Lukas, Tobi and Sebastian helped me to run my ICON simulations and to process the radar and radiometer measurements from the ORCESTRA campaign. Freddy was my number one contact for questions regarding ARTS, and Oliver helped me out when I was struggling with programming or just my computer in general. The IMPRS office, personified by Florian, Michaela, Connie and formerly Antje, supported me with all administrative issues that I had and always found a way to make things possible.

I am very thankful to my peers and friends, two groups that became less distinguishable with time, for making these last three years fun and for giving me emotional support when I needed it. I enjoyed our coffee breaks, Bergfeste, and all the other fun excuses we invented to spend time together. Among a large group of great people, I want to single out my three favourite office mates: Janina, Ravi and Marius, and everyone else who helped proofread my thesis: Lennea, Katharina, Henning and Arim.

I thank my family for their unlimited encouragement. My mother, Cornelia and my father, Sebastian, for never pushing me into a particular direction but supporting any decision that I made, my siblings, Elisa, Johann and Magdalena, for their companionship, and my grandparents, Angelika and Rolf, for sparking my interest in academia and supporting my early education.

Lastly, I thank Franca for sharing my highs, absorbing my lows, and always believing in me.

CONTENTS

I UNIFYING ESSAY 1

1 INTRODUCTION 3

2 BACKGROUND 7
- 2.1 The Forcing-Feedback Framework 7
- 2.2 Clear-Sky Controls of Tropical High Clouds 8
- 2.3 Estimates of the Tropical High-Cloud Feedback 11

3 RESOLVING TROPICAL HIGH CLOUDS WITH SIMULATIONS AND OBSERVATIONS 15

4 ICE WATER PATH FRAMEWORK 19

5 POSITIVE TROPICAL HIGH-CLOUD FEEDBACK 23
- 5.1 High-Cloud Altitude Feedback 23
- 5.2 Anvil-Cloud Amount Feedback 25
- 5.3 Diurnal Cycle Feedback 26

6 HIGHER CLIMATE SENSITIVITY 31

7 CLOSING THOUGHTS 35
- 7.1 Summary 35
- 7.2 Looking Forward 36
- 7.3 Conclusion 38

II APPENDIX 41

A INSIGHTS ON TROPICAL HIGH-CLOUD RADIATIVE EFFECT FROM A NEW CONCEPTUAL MODEL 43
- A1 Introduction 46
- A2 Model Setup 47
- A3 Ice Water Path Framework 48
- A4 Conceptual Model of the High-Cloud Radiative Effect 51
- A5 Key Ingredients of the High-Cloud Radiative Effect 52
- A6 Low Clouds Render the High-Cloud Radiative Effect Positive 55
- A7 Towards a Better Understanding of Tropical High-Cloud Feedbacks 56
- A8 Summary and Conclusion 57
- A9 Methods 59
  - A9.1 Choosing the Right Predictor for the High-Cloud Radiative Effect 59
  - A9.2 Connectedness of Clouds 61
  - A9.3 Conceptualising Albedo 62
  - A9.4 Parameterizing the Conceptual Model 63

B FACETS OF THE TROPICAL HIGH-CLOUD FEEDBACK IN A GLOBAL STORM-RESOLVING MODEL 69
- B1 Introduction 71
- B2 Resolving High Clouds at km-Scale 72
- B3 Positive High-Cloud Feedback 73

B4 Fixed High-Cloud Temperatures 76
B5 Stability Iris and Radiative Heating 77
B6 Intensification of the Diurnal Cycle of Deep Convection 78
B7 Conclusion 80
B8 Methods 80
B8.1 Aquaplanet Simulations 80
B8.2 Handling Big Data 81
B8.3 High-Cloud Radiative Effect 81
B8.4 Feedback Partitioning 83
B8.5 High-Cloud Temperature 83
B8.6 Stability Iris Analysis 83
B.S1 Supplement 85
B.S1.1 Influence of Time of Occurrence on High-Cloud Radiative Effect 85
B.S1.2 Congestus Feedback 86
B.S1.3 Albedo and Emissivity of High Clouds 87
B.S1.4 Constant Ozone Simulation 88
B.S1.5 Stability Iris 89
B.S1.6 Heating Rates 90
B.S1.7 Testing Convergence of Statistics 91
B.S1.8 Sensitivity to Connectedness of Liquid and Frozen Clouds 92
B.S1.9 Liquid Clouds at the Transition to Deep Convection 93
C OBSERVED DIURNAL CYCLE CHANGE OF TROPICAL DEEP CONVECTION AMPLIFIES SURFACE WARMING 95
C1 Introduction 96
C2 Identifying Clouds Produced by Deep Convection 97
C3 Diurnal Cycle of Deep Convection 99
C4 Reduction of Daytime Deep Convection 100
C5 Positive Diurnal-Cycle Feedback 101
C6 Conclusion 103
C7 Methods 104
C7.1 Histograms and Cloud Fraction 104
C7.2 Regression 105
C7.3 Feedback 105
C7.4 Bootstrapping 106
C.S1 Supplement 107
C.S1.1 Relation of Brightness Temperature and Ice Water Path 107
C.S1.2 Total Change in Deep Convective Clouds 108
C.S1.3 Diurnal Cycle of Radiative Fluxes 109
C.S1.4 Albedo 110
C.S1.5 Bootstrapping of Regression 111
D WEAK POSITIVE FEEDBACK FROM OBSERVED REDUCTION OF TROPICAL ANVIL CLOUDS 113
D1 Introduction 115
D2 Ice Water Path Framework 116
D3 Satellite Observations of Ice Water Path 116

D4 Reduction of Anvil Clouds 118
D5 Weak Positive Feedback 119
D6 Lingering Questions 120
D7 Conclusion 121
D8 Methods 122
D8.1 Histograms of Ice Water Path 122
D8.2 Change of Ice Water Path Frequency with Temperature 122
D8.3 Feedback 123

BIBLIOGRAPHY 125

Part I

UNIFYING ESSAY

1 INTRODUCTION

How much will the Earth warm for a given increase in atmospheric greenhouse gas concentration? This question about the sensitivity of Earth's climate is of central importance to society, but the answer remains uncertain. The overarching goal of this thesis is to reduce this uncertainty.

First estimates of climate sensitivity date back to the beginnings of climate science. Svante Arrhenius was the first to quantify climate sensitivity in 1896. Based on measurements of the radiative absorption of CO_2 and water vapour, he estimated that the global mean surface temperature would increase by 5 K to 6 K in response to a doubling of atmospheric CO_2 concentration (Arrhenius, 1896). He later revised this value to 4 K. His approach led to the development of the concept of equilibrium climate sensitivity, which is defined as the global mean surface temperature increase after a doubling of atmospheric CO_2 concentration once the Earth has reached its new thermal equilibrium. Climate science has advanced rapidly since the days of Arrhenius, and several approaches have been developed to estimate equilibrium climate sensitivity. Despite this effort, climate sensitivity remains uncertain. In their latest report, the Intergovernmental Panel on Climate Change (IPCC) combined all available lines of evidence and concluded that the equilibrium climate sensitivity is very likely between 2 K and 5 K (Forster et al., 2021).

Uncertainty of climate sensitivity complicates planning for mitigation of and adaptation to climate change. Climate change impacts increase with global mean surface temperature (Pörtner et al., 2022) and will be much more drastic for a 5 K warming compared to a 2 K warming. Reducing the uncertainty in climate sensitivity is therefore crucial to anticipate the consequences of current greenhouse gas emissions.

The key source of uncertainty in climate sensitivity is the limited understanding of climate feedbacks (Forster et al., 2021). Climate feedbacks are defined as changes in the climate system that either dampen or amplify the surface warming caused by the increase in atmospheric greenhouse gas concentration. A simple example is the surface-albedo feedback. If the Earth's surface albedo reduces in response to warming, say due to melting snow exposing darker surfaces, this will amplify the warming since the Earth absorbs more solar radiation. Since the initial warming is amplified by the surface-albedo feedback, it is defined as a positive feedback. The strongest negative climate feedback that limits global warming is the Planck feedback. As the Earth warms, it emits more thermal radiation, which dampens the initial warming. Other prominent climate feedbacks arise from changes in atmospheric water vapour, changes in vegetation, changes in the chemical composition of the atmosphere other than CO_2 and water vapour and changes in clouds.

Among all climate feedbacks considered by the IPCC, the cloud feedback is the most uncertain, making it the main cause of uncertainty in climate sensitivity. Clouds affect the Earth's temperature by interacting with radiation in two ways: They cool the Earth by reflecting solar radiation, and they warm the Earth by absorbing thermal radiation emitted from below the clouds. If clouds change in response to global

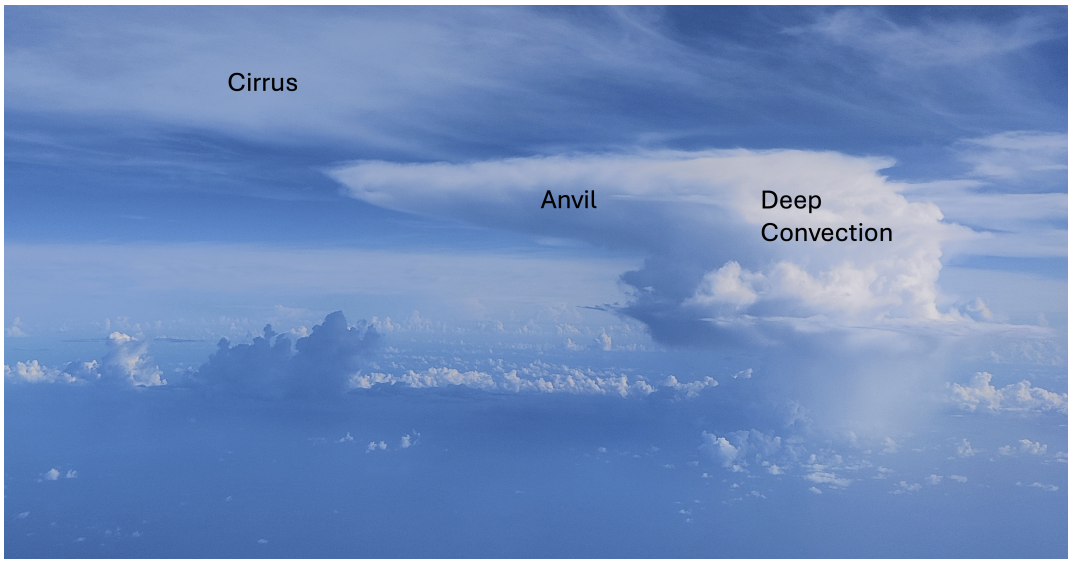


Figure 1: Picture of tropical high clouds taken during the ORCESTRA campaign.

warming, this can affect the magnitude of both their cooling and their warming effect, and thereby cause a climate feedback. Predicting such changes of clouds in response to warming is difficult due to the multiscale nature of clouds, spanning from the microscale of individual droplets to the synoptic scale of weather systems. Numerous mechanisms govern the formation and lifetime of clouds, ranging from the microphysics of cloud droplets, over radiative heating or cooling of clouds, to large-scale controls such as atmospheric stability and winds. To better understand how clouds will respond to surface warming, it has proven helpful to distinguish cloud types governed by similar physical processes.

High clouds are abundant in the tropics (30°S to 30°N), and their climate feedback is highly uncertain. High surface temperatures in the tropics stimulate the formation of deep convection reaching up to near the tropopause, where moist air spreads horizontally, forming anvil and cirrus clouds (Figure 1). In an extensive review on climate sensitivity carried out as part of the World Climate Research Programme (WCRP), the climate feedback from tropical high clouds is assessed to be most uncertain among all cloud feedbacks (Sherwood et al., 2020).

Progress in narrowing down the uncertainty of cloud feedbacks has been difficult, also because the conventional general circulation models (GCMs) have limited ability to capture the details of convection. With a horizontal grid spacing of $\mathcal{O}(100\ \mathrm{km})$, those models do not resolve convection but rely on parameterisations, which cause vast inter-model differences in the cloud response to surface warming (Stevens and Bony, 2013).

There is hope to overcome the shortcomings of GCMs with the development of global storm-resolving models (GSRMs). By moving to a horizontal grid spacing of $\mathcal{O}(1\ \mathrm{km})$, GSRMs simulate convection explicitly, eliminating parameterisations of convection as a source of uncertainty. GSRMs indeed represent some aspects of the tropical climate more accurately than GCMs: the diurnal cycle of precipitation is better captured (Stevens et al., 2020; Song et al., 2024), the representation of equatorial waves is improved (Judt and Rios-Berrios, 2021), and the inter-model

spread of relative humidity is reduced (Lang et al., 2021). However, higher spatial resolution is not the ultimate cure for model biases. Convective systems in GSRMs are too small and too short-lived (Becker et al., 2021; Feng et al., 2025) and the representation of clouds is highly sensitive to the parameterisation of microphysics (Atlas et al., 2024). Overall, GSRMs hold great promise to advance the understanding of cloud feedbacks, not only because of the above-mentioned improvements compared to GCMs, but also because their high spatial resolution allows for new perspectives on cloud feedbacks.

I use GSRMs and satellite observations to show why the tropical high-cloud feedback is more positive than previously assumed. I derive this insight by resolving the spectrum of tropical high clouds, ranging from deep convective clouds to thin cirrus. Sorting tropical high clouds by their thickness creates a space that aligns with the physics governing the clouds. Deep convective clouds depend on the deep convection itself, while anvil clouds mostly depend on the convective outflow near the tropopause, and cirrus are more sensitive to processes that affect the cloud lifetime (Gasparini et al., 2023). Resolving the spectrum of tropical high clouds allows me to understand how high clouds with different thicknesses respond to surface warming. Resolving tropical high clouds by their thickness is also crucial to understand their climate feedback, since their radiative effect strongly depends on cloud thickness. Deep convective clouds are cooling the Earth since they reflect more solar radiation than they absorb thermal radiation. This balance shifts for thinner clouds, which are more transparent to solar radiation but still effective at absorbing thermal radiation and hence warm the Earth. To understand the feedback from changes in tropical high-cloud amount, it is therefore crucial to know whether thick, cooling clouds or thin, warming clouds change in frequency.

This thesis is structured as follows: I provide background on the framework used to analyse climate sensitivity and the known mechanisms that control the response of tropical high clouds to surface warming, and summarise previous estimates of the tropical high-cloud feedback in Chapter 2. I introduce the simulations and satellite observations on which my analysis is based in Chapter 3. I explain my method of sorting tropical high clouds by their thickness to diagnose their feedback in Chapter 4. I explain my key finding of a positive tropical high-cloud feedback, and show that the feedback consists of three components in Chapter 5. I summarise my estimates of the tropical high-cloud feedback and show that my findings imply a higher climate sensitivity than previously expected in Chapter 6. I conclude the thesis with Chapter 7.

2

BACKGROUND

In this chapter, I introduce the common framework for analysing climate sensitivity, the known mechanisms governing the response of tropical high clouds to surface warming, and previous estimates of the tropical high-cloud feedback.

2.1 THE FORCING-FEEDBACK FRAMEWORK

A useful and well-established approach to think about Earth's climate sensitivity is the forcing-feedback framework. I give a general overview of the framework in this section, but a more detailed derivation can be found in Ghil and Lucarini (2020).

Within the forcing-feedback framework, the global mean energy imbalance (ΔN) at the top of the atmosphere is given by the sum of a radiative forcing (F) and the radiative response to that forcing. The radiative response is defined as the change in global mean surface temperature (ΔT) times the climate feedback parameter (λ), so the energy imbalance is written as

$$\Delta N = F + \lambda \Delta T.$$

The climate feedback parameter is defined as the sensitivity of N to a change in T:

$$\lambda = \frac{\mathrm{d}N}{\mathrm{d}T}.$$

In climate science, radiative fluxes are usually defined as positive downward. An increase in CO_2 reduces the upward radiative flux, hence the resulting forcing is positive. This means that λ needs to be negative for the system to be stable.

The forcing-feedback framework facilitates the understanding of global warming by separating the radiative forcing, which is independent of surface temperature, and the temperature-dependent radiative response. For a clean separation, the forcing definition must include adjustments of the atmosphere to an increase in CO_2 that affect N but are independent of T. To satisfy this condition, the effective radiative forcing is defined, which includes fast (up to monthly) radiative adjustments that are independent of surface temperature.

The Earth will warm in response to a positive radiative forcing until a new equilibrium state with $\Delta N = 0$ is reached. The equilibrium climate sensitivity (E) is defined as the equilibrium warming that results from the effective radiative forcing from a doubling of atmospheric CO_2 concentration (F_{2xCO_2}):

$$E = -\frac{F_{2xCO_2}}{\lambda}. \tag{1}$$

A more negative λ, therefore, results in a smaller E.

The climate feedback parameter consists of different components, which are assumed to be independent:

$$\lambda = \sum \lambda_i.$$

If the Earth was a perfect blackbody without an atmosphere, λ would just be the Planck feedback with $\lambda = -4\sigma T^3$, where σ is the Stefan-Boltzmann constant. However, the response of the atmosphere and the surface to surface warming adds to λ, rendering it less negative than the Planck feedback. The most prominent components of λ that add to the Planck feedback are the surface-albedo feedback, the lapse rate and water vapour feedback, biogeophysical feedbacks and the cloud feedback (Forster et al., 2021). Since the response of clouds to surface warming is diverse, it has proven helpful to further decompose the cloud feedback into contributions from different cloud types, one of which are tropical high clouds (e.g. Sherwood et al., 2020; Zelinka et al., 2022).

I use the forcing-feedback framework to assess how the tropical high-cloud feedback affects climate sensitivity.

2.2 CLEAR-SKY CONTROLS OF TROPICAL HIGH CLOUDS

The current understanding of how tropical high clouds will respond to surface warming is based on the idea that radiatively driven subsidence in clear-sky regions controls the formation of high clouds via mass balance. If air subsides due to radiative cooling in clear-sky regions, it must rise in convective regions, where it eventually forms high clouds. How clear-sky radiative subsidence responds to surface warming is well understood and allows for two conclusions about the change of high clouds: anvil clouds should rise isothermally, and the amount of anvil clouds should decrease in response to surface warming. The fixed anvil temperature (FAT) theory, explaining the isothermal rise of anvil clouds, was developed by Hartmann and Larson (2002). They were the first to link clear-sky radiative cooling and the formation of high clouds. Their theory was developed further by Bony et al. (2016) to explain that the amount of tropical anvil clouds is expected to decrease due to an increase in atmospheric stability as a result of surface warming, which is known as the stability iris theory.

The two key ingredients that are necessary to understand how radiative subsidence and tropical high clouds change in response to surface warming are the thermal expansion of the troposphere and the Clausius-Clapeyron (CC) relationship. As the surface warms, so does the troposphere above, causing it to expand. This means that for a warmer surface, the same air temperature will occur at a higher altitude and lower pressure, i.e., the isotherms shift upwards. Since the amount of water vapour is tied to temperature via the CC relationship, the water vapour follows the upward migration of the isotherms. Radiative cooling in clear-sky regions to first order depends on the amount of water vapour and hence also follows the upward migration of the isotherms. In the following, I explain how high clouds are tied to radiative cooling via mass balance to explain the FAT and the stability iris theory. Since radiative cooling and hence high clouds remain approximately constant on isotherms, it has proven useful to choose temperature as the vertical coordinate (Jeevanjee, 2022).

Central to FAT and the stability iris is the assumption that horizontal divergence in cloudy regions ($\nabla_\mathrm{h}\mathbf{v}_\mathrm{cld}$), which detrains anvil clouds from deep convection, is con-

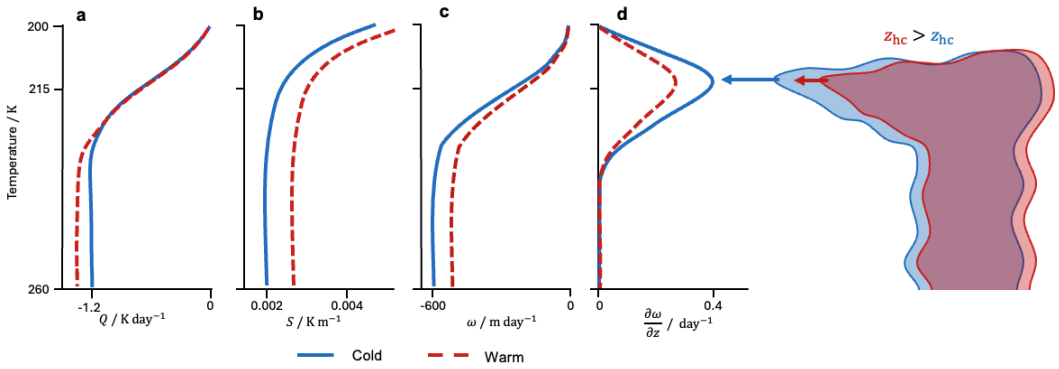


Figure 2: Schematic of fixed anvil temperature and stability iris mechanism. From left to right, the panels show radiative cooling (Q), stability (S), radiative subsidence (ω) and vertical divergence of the radiative subsidence, all plotted against temperature. The arrows connected to the clouds visualise detrainment from deep convection. High-cloud altitude z_{hc} increases as the surface warms.

strained by horizontal convergence in clear-sky regions ($-\nabla_h \mathbf{v}_{clear}$) via mass balance:

$$\nabla_h \cdot \mathbf{v}_{cld} = -\nabla_h \cdot \mathbf{v}_{clear}. \tag{2}$$

The horizontal convergence can be written as the divergence of the vertical velocity, which in clear-sky regions is approximately equal to the radiative subsidence (ω), calculated as the radiative cooling (Q) divided by the atmospheric stability (S):

$$-\nabla_h \cdot \mathbf{v}_{clear} \approx \frac{\partial \omega}{\partial z} = \frac{\partial}{\partial z}\frac{Q}{S}, \tag{3}$$

where z is the height. This relationship can be derived from the conservation of dry static energy, invoking the assumption that horizontal temperature gradients are zero in the tropics (Jenney et al., 2020; Jeevanjee, 2022). I neglect the latent cooling from the evaporation of cloud droplets in agreement with earlier studies (Bony et al., 2016; Saint-Lu et al., 2022).

The FAT theory is based on the assumption that the anvil clouds are detrained from deep convection at the altitude (z_{hc}) where $\nabla_h \cdot \mathbf{v}_{cld}$ maximises, which by Eq. 2 is the height at which $-\nabla_h \cdot \mathbf{v}_{clear}$ maximises. By invoking Eq. 3, this can be written as

$$z_{hc} = \arg\max_z \left(\frac{\partial \omega}{\partial z}\right) = \arg\max_z \left(\frac{\partial}{\partial z}\frac{Q}{S}\right). \tag{4}$$

This can be boiled down to the simple statement that anvil clouds form at the altitude where radiative subsidence sets in.

Anvil clouds are expected to follow the thermal expansion of the troposphere and remain at fixed temperature in response to surface warming, since radiative subsidence depends on the amount of water vapour, which is tied to temperature via the CC relationship (Hartmann and Larson, 2002). The temperature below which Q and hence ω sets in stays approximately fixed despite surface warming (Fig. 2a, c). Therefore, $\partial\omega/\partial z$ also remains at fixed temperature (Figure 2d). Since anvil clouds

are tied to the maximum of $\partial\omega/\partial z$ via Eq. 4, they must also rise to remain at fixed temperature. That tropical anvil clouds do indeed follow the upward shift of $\partial\omega/\partial z$ to stay at approximately fixed temperature was shown with satellite observations (Zelinka and Hartmann, 2011).

The upward shift of anvil clouds is not strictly isothermal in most GCMs, which disagrees with the FAT theory and led to the development of the proportionately higher anvil temperature (PHAT) theory (Zelinka and Hartmann, 2010). Anvil clouds are warming in GCMs as the surface temperature increases by about 0.33 K per K surface warming (Ceppi et al., 2017). The PHAT theory explains this warming of the anvil clouds with the increase in S. However, the warming of anvil clouds might also be a bias from ozone being prescribed to be constant on pressure levels within GCMs (Taylor et al., 2012; Eyring et al., 2016). This hypothesis was brought up by Seidel and Yang (2022), who claim that prescribed ozone leads to an artificial warming of tropical anvil clouds.

The stability iris theory expands on the FAT theory and states that the amount of anvil clouds (A) detrained from deep convection is proportional to the magnitude of $\nabla_\mathrm{h} \cdot \mathbf{v}_\mathrm{cld}$. The stronger the horizontal divergence, the more anvil clouds will form. By invoking Eq. 2 and 3, this can be written as

$$A \propto \max\left(\frac{\partial\omega}{\partial z}\right) = \max\left(\frac{\partial}{\partial z}\frac{Q}{S}\right). \tag{5}$$

Atmospheric stability can be written as the difference between the dry adiabat (Γ_d) and the actual lapse rate (Γ):

$$S = \Gamma_\mathrm{d} - \Gamma \tag{6}$$

In the tropics, Γ approximately follows a moist adiabat, which is set in convective regions and communicated throughout the tropics by gravity waves, establishing weak horizontal temperature gradients (Charney, 1963).

The amount of anvil clouds is expected to decrease in response to surface warming due to an increase in S (Bony et al., 2016). The increase in S results from the pressure dependence of the moist adiabat. While Γ_d is a constant, the moist adiabat and hence Γ decreases at a fixed isotherm due to the decrease in pressure that results from the thermal expansion of the troposphere. The increase in S (Figure 2b) causes a decrease in ω (Figure 2c) and hence $\max(\partial\omega/\partial z)$ (Figure 2d), which is thought to cause a decrease in A (Eq. 5). The existence of the link between $\max(\partial\omega/\partial z)$ and A was proven with ERA5 data and satellite observations (Saint-Lu et al., 2020). The decrease in ω from an increase in S is partly cancelled by an increase in Q, but the increase in S dominates (Figure 2). This partial cancellation was also found in GCMs (Bony et al., 2016).

My results agree with the FAT and the stability iris theory. I show that in GSRM simulations, all tropical high clouds rise isothermally to higher altitudes as the surface warms, in agreement with the FAT theory (Chapter 5.1). Prescribing ozone to be constant on pressure levels does indeed lead to an artificial warming of high clouds in these simulations, casting doubt on the PHAT theory. I furthermore show that the amount of anvil clouds reduces in response to surface warming in GSRM simulations and satellite observations, in agreement with the stability iris theory (Chapter 5.2).

2.3 ESTIMATES OF THE TROPICAL HIGH-CLOUD FEEDBACK

The WCRP assessment of climate sensitivity includes an expert assessment of tropical high-cloud feedback (λ_{hc}), which I use as a reference for comparison with my results. This assessment draws on evidence from GCMs, cloud-resolving models, and satellite observations available at the time.

All feedback estimates in the WCRP study and in my unifying essay are global mean values. Feedbacks that only act in the tropics must be scaled by the area fraction of the tropics, $1/2$, to yield the global mean feedback values, since they are assumed to be zero outside of the tropics. Using global mean feedback values of the tropical high-cloud feedback has the advantage that all feedback estimates can be directly compared and added to the global climate sensitivity parameter.

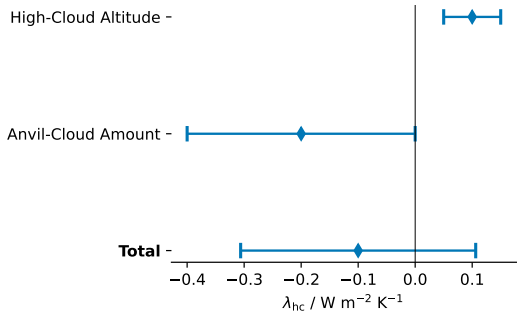


Figure 3: Tropical high-cloud feedback (λ_{hc}) from the WCRP assessment (Sherwood et al., 2020). I derive the tropical high-cloud altitude feedback from the WCRP value that includes all latitudes and calculate the uncertainty of the total feedback as the root-sum-square of the individual uncertainties. All feedback values are global means.

There is agreement among all lines of evidence that high clouds will rise to higher altitude near-isothermally in response to surface warming and thereby produce a positive feedback (e.g. Hansen et al., 1984; Wetherald and Manabe, 1988; Bretherton et al., 2014; Zelinka et al., 2016; Ceppi et al., 2017; Vaillant de Guélis et al., 2018). The feedback from the increase in cloud altitude is positive because high clouds mask the Planck feedback. A warmer surface and lower atmosphere emit more longwave (LW) radiation according to the Stefan-Boltzmann law. High clouds absorb this LW radiation and emit LW radiation depending on their temperature. If high clouds are isothermal as suggested by the FAT theory, the outgoing LW radiative flux does not change with surface warming in regions with high clouds, preventing the cooling of the Earth from the Planck feedback. The magnitude of this high-cloud altitude feedback depends on the temperature change of high clouds in response to warming.

The WCRP assessment of the high-cloud altitude feedback is entirely based on GCMs. High clouds are warming in those GCMs, but less than the surface, giving rise to a positive feedback of 0.2 ± 0.1 W m^{-2} K^{-1} (Zelinka et al., 2016). The second estimate mentioned in the WCRP assessment is based on internal variability within satellite observations (Vaillant de Guélis et al., 2018), which yields a feedback of 0.35 ± 0.2 W m^{-2} K^{-1} when scaled to the long-term warming trend.

I scale the estimate of the high-cloud altitude feedback from the WCRP, which includes clouds at all latitudes, to the tropical high-cloud altitude feedback. Even though the FAT theory only applies to tropical high clouds (Hartmann and Larson, 2002), the near-isothermal rise of high clouds occurs at all latitudes in the GCMs the WCRP assessment is based on. The magnitude of the resulting feedback is similar inside and outside of the tropics (Figure 5d in the WCRP assessment). Therefore, I multiply the high-cloud altitude feedback and its uncertainty from the WCRP assessment by the area fraction of the tropics, $1/2$, to ignore the feedback from outside the tropics. This yields the global mean feedback value of the tropical high-cloud altitude feedback (Figure 3).

It was debated for more than two decades whether a strong negative feedback from a reduction of tropical anvil clouds exists. This hypothesis was first proposed by Lindzen et al. (2001), who argue that precipitation efficiency increases with warming, leaving less cloud condensate available to form anvil clouds. They assume that the reduction in anvil-cloud cover would cool the Earth by allowing more LW radiation to escape to space. They refer to this mechanism as the infrared iris. The infrared iris hypothesis was heavily debated (Hartmann and Michelsen, 2002; Lindzen et al., 2002; Fu et al., 2002; Lin et al., 2004; Chou and Lindzen, 2005; Mauritsen and Stevens, 2015; Lindzen and Choi, 2022) and eventually superseded by the stability iris as the prevailing explanation for the reduction in anvil-cloud amount in response to surface warming (Bony et al., 2016). However, the stability iris only predicts a decrease of anvil clouds in response to surface warming, but does not quantify the resulting feedback. Quantifying the tropical anvil-cloud amount feedback proved to be more complex than proposed by Lindzen et al. (2001) since a reduction of anvil-cloud amount does not only cool the Earth by allowing for more LW radiation to escape to space, but also warms the Earth since less shortwave (SW) radiation is reflected (Sokol et al., 2024).

Given the sparsity of reliable estimates of the tropical anvil-cloud amount feedback, the WCRP largely bases their estimate on a single study that uses internal variability within satellite observations (Williams and Pierrehumbert, 2017). The WCRP estimates the tropical anvil-cloud amount feedback to be negative but highly uncertain at -0.2 ± 0.2 W m^{-2} K^{-1} (Figure 3). Among all cloud feedbacks included in the WCRP assessment, the tropical anvil-cloud amount feedback is most uncertain.

Cloud radiative kernels (Zelinka et al., 2012a; Zelinka et al., 2012b) have emerged as one of the most common tools for diagnosing cloud feedbacks and hence strongly influence their nomenclature, causing some confusion that I aim to resolve here. Cloud radiative kernels separate changes of cloud properties from changes in the clear-sky atmosphere to cleanly calculate the cloud feedback. The central idea of this method is that the cloud feedback (λ_{cl}) can be decomposed into the sensitivity of the net radiative flux at the top of the atmosphere (N) to the change in cloud fraction (f) times the change in cloud fraction (Δf):

$$\lambda_{\mathrm{cl}} = \frac{\mathrm{d}N}{\mathrm{d}f}\Delta f.$$

The sensitivity of N to f is referred to as the cloud radiative kernel (K). The advantage of this method is that K is calculated with radiative transfer simulations in which only f is changed. This allows to disentangle the cloud feedback from clear-sky

effects such as the increase in water vapour concentration. To distinguish different cloud types, K and Δf are calculated for several optical depth (τ) and cloud top pressure (p_{cld}) bins. The cloud feedback calculated from $K(\tau, p_{\mathrm{cld}})$ and $\Delta f(\tau, p_{\mathrm{cld}})$, is decomposed into feedbacks from the change in mean cloud area, changes in cloud altitude and changes in cloud optical depth (Zelinka et al., 2016). Within this framework, a reduction of tropical anvil clouds would be decomposed into an area feedback and an optical depth feedback. The WCRP assessment refers to the feedback from changes in the amount of tropical anvil clouds as the tropical anvil-cloud area feedback, giving the impression that they only include the area feedback, but not the optical depth feedback. This impression is incorrect. The WCRP assessment includes both the area and the optical depth feedback (personal correspondence with Steven Sherwood), as does the study their feedback estimate is based on (Williams and Pierrehumbert, 2017). I refer to this feedback as the tropical anvil-cloud amount feedback, which includes both the area and the optical depth feedback.

The total λ_{hc} from the WCRP assessment is slightly negative and highly uncertain at -0.1 ± 0.21 W m^{-2} K^{-1} (Figure 3). I calculate the error of the total feedback as the root-sum-square of the individual errors, assuming they are independent (personal correspondence with Steven Sherwood).

My results confirm a positive feedback from an isothermal rise of tropical high clouds to higher altitude, but disagree with a negative feedback from changes in tropical anvil-cloud amount. I show that the feedback from changes in tropical anvil-cloud amount is small, which is in agreement with other recent studies (McKim et al., 2024; Sokol et al., 2024; Raghuraman et al., 2024; Wilson Kemsley et al., 2025).

3

RESOLVING TROPICAL HIGH CLOUDS WITH SIMULATIONS AND OBSERVATIONS

My analysis of the tropical high-cloud feedback is based on two major recent advancements in climate science that are fuelled by the increase in computational power: GSRMs, and machine learning for satellite retrievals. Both tools allow for resolving the spectrum of tropical high-cloud thickness. In this chapter, I introduce the GSRM simulations and the satellite retrievals that I use for my analysis. More details can be found in the publication in Appendix B for the simulations, and the publications in Appendix C and D for the satellite retrievals.

A major advantage of GSRMs over GCMs is that they explicitly resolve clouds, enabling more direct comparison with satellite observations. The horizontal grid spacing of GCMs of $\mathcal{O}(100\ \mathrm{km})$ is too coarse to resolve individual clouds, calling for the use of cloud fractions. The cloud fraction defines the fraction of the grid box that is considered cloudy, while the rest is considered cloud-free. Therefore, assumptions about the overlap of clouds at different heights are required to decide whether an entire column of a GCM is cloudy (Geleyn and Hollingsworth, 1979; Pincus et al., 2005). This complicates the interpretation of clouds in GCMs. The fine horizontal grid spacing of GSRMs and the satellite observations used in this thesis of $\mathcal{O}(1\ \mathrm{km})$ allows for a more natural perspective on clouds that does not invoke cloud fractions. In both GSRMs and satellite observations, clouds are defined by the cloud condensate within a grid box. If condensate exists, it is assumed to be evenly distributed in the grid box and the whole grid box is considered cloudy. Therefore, no assumptions about cloud overlap are required. A column is considered cloudy if it contains condensate, and the total mass of condensate within a column can be used as a measure of cloud thickness. I use this common perspective of GSRMs and satellite observations on clouds to analyse how tropical high clouds respond to surface warming.

I resolve the spectrum of tropical high clouds by cloud thickness. I use the ice water path (I), defined as the total mass of ice condensate within a column, as a measure of cloud thickness, which is available from GSRMs and satellite observations.

Simulations with GSRMs remain at the edge of computational feasibility; hence, I conduct idealised simulations that allow for short simulation periods. I use an aquaplanet setup (Blackburn et al., 2013; Peinado Bravo et al., 2026), which assumes the Earth is fully covered by water and has no seasonal cycle. Given the lack of a seasonal cycle, three months of simulation are sufficient to reach a statistically stable state. Despite their reduced complexity, aquaplanet simulations reproduce key features of the Earth's atmosphere, and have proven useful for studying cloud feedbacks (Medeiros et al., 2015).

I conduct three aquaplanet simulations with prescribed zonally symmetric sea surface temperatures (SSTs): a control simulation, a simulation with a 2 K uniform SST increase and a simulation with a 4 K uniform SST increase. I use the ICOsahedral Nonhydrostatic (ICON) model (Hohenegger et al., 2023), with parameterised turbu-

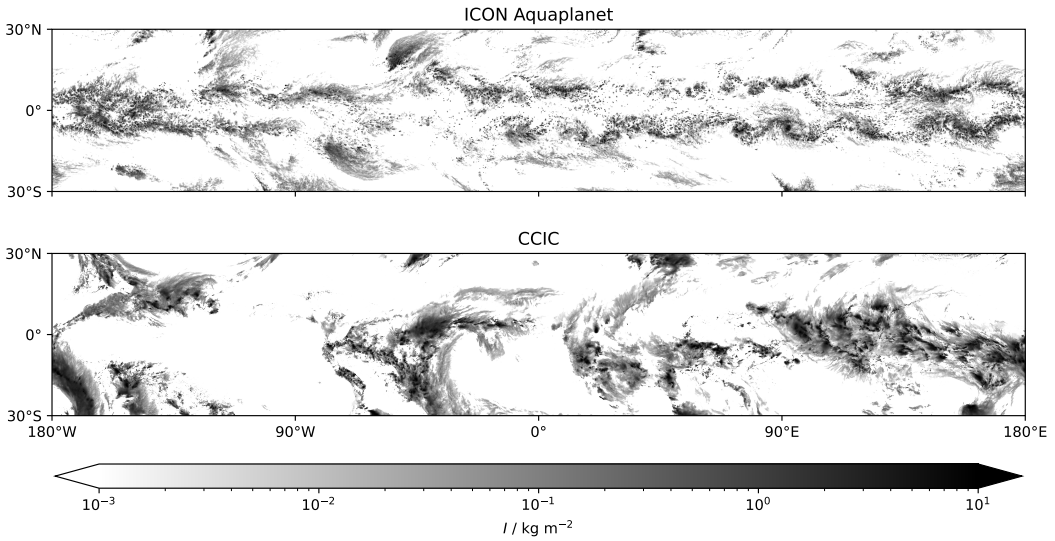


Figure 4: Snapshots of ice water path (I) from the ICON control simulation and random day of the CCIC satellite observations (2022-01-01 22:00).

lence (Smagorinsky, 1963), cloud microphysics (Baldauf et al., 2011) and interactive ozone (Cariolle and Teyssèdre, 2007).

The most accurate satellite retrievals of I use collocated radar and lidar measurements, but such measurements are sparse (Eriksson et al., 2026). I use two retrievals of I that are based on collocated radar and lidar measurements: 2C-ICE R05 (Deng et al., 2010) and DARDAR v3.1 (Cazenave et al., 2019). Both retrievals use the same radar and lidar measurements but employ different algorithms to retrieve I. Since the satellites carrying the radar and the lidar fly on a sun-synchronous polar orbit, I from DARDAR and 2C-ICE is only available along the satellite path at 1:30 AM and 1:30 PM local time.

The sparsity of I retrieved from active satellite measurements is overcome with recently developed machine learning algorithms that retrieve I from widely available passive satellite measurements. I use the Chalmers Cloud Ice Climatology (CCIC) (Amell et al., 2024; Pfreundschuh et al., 2025) that employs a machine learning algorithm trained on 2C-ICE to infer I from the spatial structure of brightness temperatures observed by geostationary satellites. I also use the Synergistic Passive Atmospheric Retrieval Experiment-ICE (SPARE-ICE) (Holl et al., 2014), which employs a machine learning algorithm to retrieve I from infrared and microwave radiances. The algorithm of SPARE-ICE is also trained on 2C-ICE. If possible, I test my results from the machine learning retrievals of I with active measurements of I. If this is not possible, I use the underlying passive satellite measurements to test whether they support the results from the machine learning retrievals of I. Those tests generally confirm the results from CCIC and SPARE-ICE, fostering confidence in the usefulness of machine learning for expanding satellite observations.

The direct comparison of high clouds from the ICON aquaplanet simulations and CCIC satellite observations reveals a broad resemblance, but major differences remain (Figure 4). Such differences are to some extent expected. Clouds over a global ocean with zonally symmetric surface temperature will always look different from

clouds in the real world, but model biases add to this discrepancy. Convective systems in GSRMs are not aggregated enough and too short-lived in GSRMs (Becker et al., 2021; Feng et al., 2025). Furthermore, the majority of clouds form in two distinct lines north and south of the equator in my simulations, while the real structure of clouds in the tropics is more varied. This is a known bias of GSRMs (Peinado Bravo et al., 2026; Segura et al., 2025b) which can be improved by changing the parameterisation of surface heat fluxes (Segura et al., 2025a). These limitations highlight the importance of testing the simulation results with observations.

I use the simulations to explore ideas about the response of tropical high clouds to surface warming, which I test with internal variability within satellite observations. To this end, I analyse the response of tropical high clouds to the internal variability of the tropical mean surface temperature, which is mostly driven by the El Niño-Southern Oscillation (ENSO). Internal variability has been used before to assess the response of tropical high clouds to surface warming (Zelinka and Hartmann, 2011; Vaillant de Guélis et al., 2018; Saint-Lu et al., 2022) and to constrain high-cloud feedbacks (McKim et al., 2024). I find general agreement between the high-cloud response to a uniform surface warming in aquaplanet simulations and the observed high-cloud response to warming from internal variability, lending confidence to my results.

4

ICE WATER PATH FRAMEWORK

Resolving the spectrum of tropical high clouds by cloud thickness facilitates the understanding of the tropical high-cloud feedback because the high-cloud radiative effect and the physical processes governing cloud evolution primarily depend on cloud thickness. I use the ice water path, I, as a measure of cloud thickness. In the following, I outline how this ice water path framework works and why it is useful. Details can be found in the publications in Appendix A and B.

I define high clouds as all clouds that contain frozen condensate, and I define liquid condensate as part of the high clouds if it sufficiently overlaps with the frozen condensate. This avoids artificial separation of liquid and frozen clouds. At high I, liquid condensate often overlaps with frozen condensate, and both are part of the same cloud (Figure 5a). This changes for low I, since cirrus clouds usually do not contain liquid and are distinct from liquid clouds below.

The physical mechanisms governing high clouds vary across the I range. The thickest clouds are formed by deep convection, anvil clouds are detrained from the deep convection, and thin cirrus can either form in situ or as remnants of anvil clouds (Gasparini et al., 2023). Sokol and Hartmann (2020) define I ranges for those different cloud types that I adopt: deep convective clouds ($I > 1$ kg m^{-2}), anvil clouds (1 kg m$^{-2} \geq I > 10^{-2}$ kg m^{-2}) and thin cirrus ($I \leq 10^{-2}$ kg m^{-2}).

The I of high clouds to first order determines their cloud radiative effect (C). The net $C(I)$ is positive for small I and negative for high I with the sign change occurring at $I \approx 2 \cdot 10^{-1}$ kg m^{-2} (Figure 5b). This shape of $C(I)$ was also diagnosed from satellite observations (Gasparini et al., 2022) and radiative convective equilibrium simulations (Sokol et al., 2024). While the sign change of $C(I)$ is robust, the exact I at which it occurs is sensitive to the methodology and the radiative transfer scheme used to derive $C(I)$.

The mean high-cloud radiative effect ($\overline{C}$) is calculated as the sum of $C(I)$ weighted by the high-cloud frequency (P):

$$\overline{C} = \sum_I C(I) \cdot P(I), \tag{7}$$

where $P(I)$ should be interpreted as the I-resolved high-cloud fraction. The sum of $P(I)$ over a given I range yields the area fraction covered by clouds within that I range. Thin clouds with a weakly positive $C(I)$ are much more frequent than thick clouds with a strongly negative $C(I)$ (Figure 5c). Therefore, $\overline{C}$ is small in ICON (Figure 5d), which is consistent with satellite observations (Hartmann, 2016; L'Ecuyer et al., 2019; McKim et al., 2024).

The ice water path framework allows me to analyse how high clouds with different thickness contribute to the tropical high-cloud feedback (λ_{hc}). The total λ_{hc} is calculated as the change in $\overline{C}$ per unit warming:

$$\lambda_{\mathrm{hc}} = \frac{1}{2}\frac{\Delta\overline{C}}{\Delta T} \approx \sum_I \underbrace{\frac{1}{2}P(I)\frac{\Delta C(I)}{\Delta T}}_{\lambda_{\mathrm{C}}(I)} + \sum_I \underbrace{\frac{1}{2}\frac{\Delta P(I)}{\Delta T}C(I)}_{\lambda_{\mathrm{P}}(I)}, \tag{8}$$

with T being the mean surface temperature, and Δ the difference between the warm and the cold climate. This linearised chain rule separates the feedback contributions from changes in high-cloud frequency and changes in the high-cloud radiative effect, referred to as λ_{P} and λ_{C} respectively. The factor $1/2$ accounts for the area fraction of the tropics and scales the feedback to a global mean value. It should be noted that this scaling is not applied in the publications in Appendix B, C and D.

The ice water path framework is based on previous studies, but I advance its usefulness and apply it to GSRM simulations and satellite observations. Sorting high clouds and their radiative effect by I has been done before for satellite observations

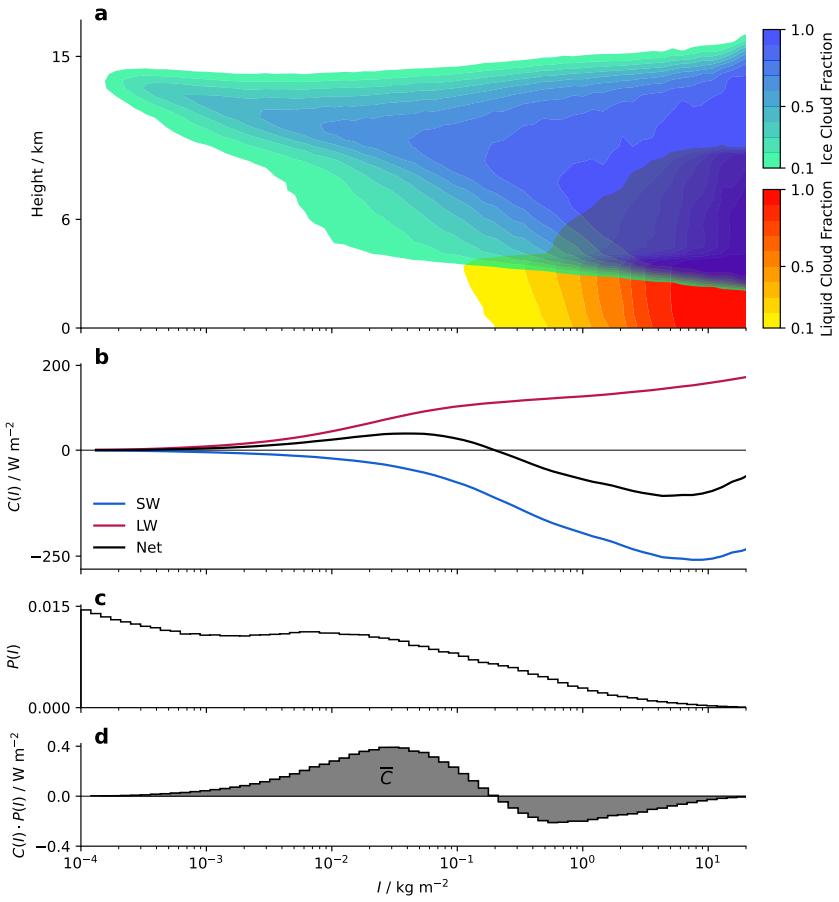


Figure 5: Tropical high clouds and their radiative effect in the ICON control simulation. (**a**) Cloud fraction of high clouds, (**b**) high-cloud radiative effect (C), (**c**) high-cloud frequency (P), (**d**) net C times P, all plotted as a function of ice water path (I). The area under the curve of $P \cdot C$ is proportional to the mean high-cloud radiative effect ($\overline{C}$).

(Berry and Mace, 2014; Gasparini et al., 2022) and the ice water path framework was used to analyse λ_{P} from RCE simulations (Sokol et al., 2024). I advance the usefulness of the ice water path framework by showing that the high-cloud radiative effect can be understood by conceptualising high clouds as a single layer, whose emissivity, albedo and temperature are functions of I. This allows me to understand changes in the high-cloud radiative effect in response to warming and hence λ_{C}.

5 POSITIVE TROPICAL HIGH-CLOUD FEEDBACK

Resolving the spectrum of tropical high clouds by cloud thickness reveals why the tropical high-cloud feedback is positive. I find three components of the tropical high-cloud feedback: a positive LW feedback from the isothermal rise of all high clouds to higher altitude, a small feedback from the reduction of tropical anvil-cloud amount and a positive SW feedback from a change in the diurnal cycle of deep convection. In this chapter, I explain each component of the tropical high-cloud feedback based on the ICON aquaplanet simulations and show that a small anvil-cloud amount feedback and a positive diurnal cycle feedback are supported by satellite observations. All results are limited to the tropics, defined as 30°S to 30°N for the observations and 20°S to 20°N for the aquaplanet simulations, in which the tropics are less wide since no seasonal cycle exists. Details on the results from the aquaplanet simulations can be found in the publication in Appendix B. The support from satellite observations is shown in detail in the publication in Appendix D for the anvil-cloud amount feedback and in the publication in Appendix C for the diurnal cycle feedback.

5.1 HIGH-CLOUD ALTITUDE FEEDBACK

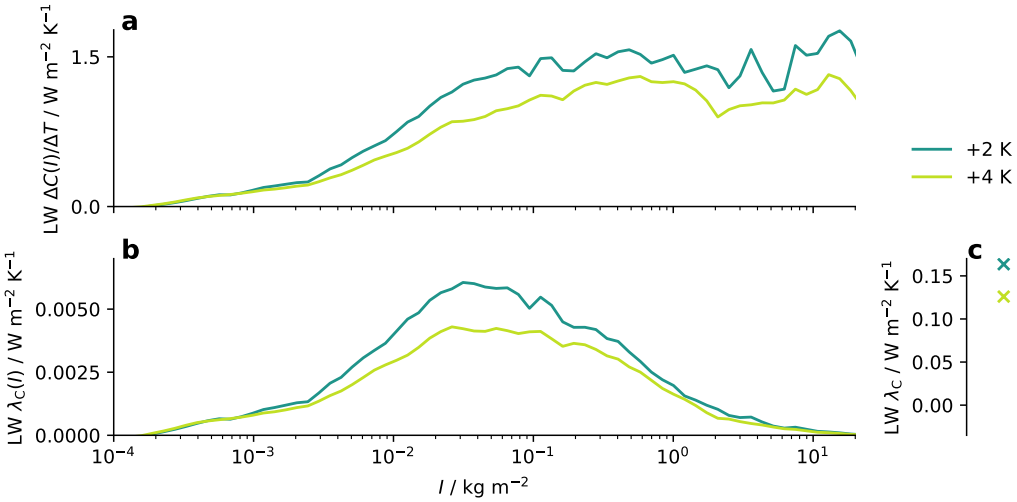


Figure 6: (**a**) Change in the LW high-cloud radiative effect (ΔC) per unit warming (ΔT) as a function of ice water path (I). (**b**) LW feedback from changes in C (λ_C) as a function of I. (**c**) Total LW λ_C plotted on the same scale as Figure 8d and Figure 9c. All feedback values are global mean values.

High clouds remain at approximately fixed temperatures despite surface warming in agreement with the FAT theory, producing a positive LW feedback. This isothermal rise of high clouds in ICON disagrees with most GCMs that predict a slight warming of high clouds, explained by the PHAT theory. I show that this high-cloud

warming is partly explained by an unrealistic treatment of ozone, casting doubt on the PHAT theory.

The LW $C(I)$ becomes more positive at all I in response to surface warming (Figure 6a). I multiply the change in $C(I)$ with $P(I)$ from the control simulation to derive the LW $\lambda_C(I)$ (Eq. 8, Figure 6b). The LW $\lambda_C(I)$ is strongest at intermediate I, where the LW $\Delta C(I)$ reaches its plateau and high clouds are still frequent.

The positive LW λ_C is explained by high clouds remaining at approximately fixed temperatures in agreement with the FAT theory (Hartmann and Larson, 2002). The high-cloud top temperature (T_{hc}) varies strongly with I. Deep convective clouds are coldest, anvils are warmest and thin cirrus are almost as cold as deep convective clouds (Figure 7a). Given the wide range of $T_{hc}(I)$, its change in response to surface warming is remarkably small (Figure 7b). Averaged over all I, the change in T_{hc} per degree of surface warming is -0.17 K K^{-1} (+2 K) and -0.06 K K^{-1} (+4 K).

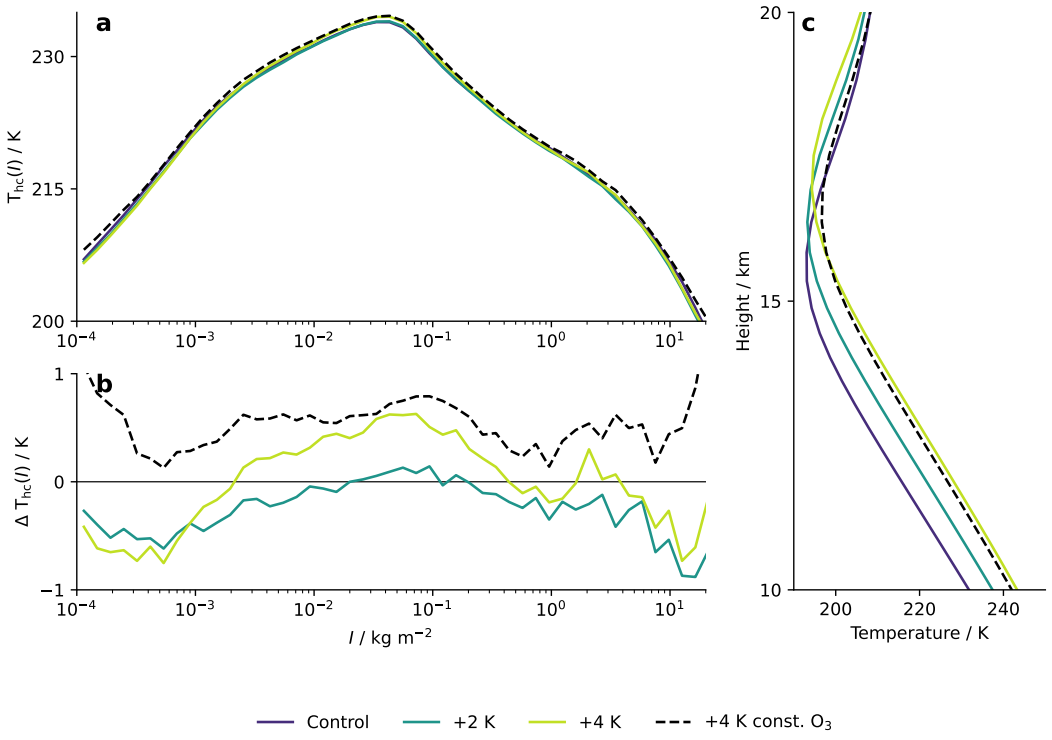


Figure 7: (**a**) High-cloud temperature (T_{hc}) as a function of ice water path (I), (**b**) change of T_{hc} with respect to the control simulation (ΔT_{hc}) and (**c**) mean clear-sky temperature profiles.

An interactive ozone scheme is necessary to capture the isothermal rise of high clouds. Simulations with GCMs used to calculate cloud feedbacks do not use an interactive ozone scheme but prescribe ozone to be constant on pressure levels (Taylor et al., 2012; Eyring et al., 2016). Therefore, ozone can not follow the isotherms to higher altitude as the surface warms, which has been claimed to cause an unrealistic warming of high clouds (Seidel and Yang, 2022). Indeed, high clouds are warming at 0.33 K K^{-1} in GCMs (Ceppi et al., 2017). I test whether this warming in GCMs results from unrealistic treatment of ozone with an additional +4 K warming simulation for which I prescribe the ozone profile from the control simulation to remain constant

on pressure levels. I find that high clouds warm at all I if ozone is prescribed (Figure 7b). The reason for this artificial warming of high clouds is that prescribed ozone leads to an unrealistic tropopause warming (Figure 7c). The tropopause migrates upward as the surface warms, but ozone concentrations stay fixed, causing higher ozone concentrations and hence higher temperatures in the tropopause, where the highest clouds reside. However, this only explains part of the high-cloud warming seen in GCMs. If ozone is prescribed, high clouds in ICON warm at 0.09 K K^{-1}.

5.2 ANVIL-CLOUD AMOUNT FEEDBACK

The amount of anvil clouds decreases in response to surface warming, in agreement with the stability iris theory, but the resulting feedback is near-neutral, and not negative as previously assumed (Sherwood et al., 2020; Forster et al., 2021). Satellite observations and the ICON simulations agree that the feedback is small since the positive feedback from a reduction of thick, cooling clouds is balanced by the negative feedback from a reduction of thin, warming clouds.

I use all four retrievals of I to test whether the response $P(I)$ to surface warming from the ICON simulations is realistic. I also include the ensemble mean of the cloud-resolving RCEMIP simulations (Wing et al., 2018) for comparison, since this was the first set of simulations that was analysed with the ice water path framework to show that the anvil-cloud amount feedback is small (Sokol et al., 2024),

Anvil clouds decrease in response to surface warming (Figure 8a) in agreement with the stability iris theory (Bony et al., 2016). This decrease in $P(I)$ is statistically significant at a 95% confidence level between $I = 4$ kg m^{-2} and $I \approx 3 \cdot 10^{-2}$ kg m^{-2} for the satellite observations (Figure 8b). The decrease of anvil clouds is more than twice as strong in the observations compared to the simulations. Two of the most profound differences between simulations and observations that might explain this discrepancy are that the simulations do not include land and that the warming is spatially uniform, whereas the observed warming from internal variability has a pattern.

The feedback from the observed and simulated reduction of anvil clouds is small since the positive feedback from a reduction of thick, cooling clouds is cancelled by the negative feedback from a reduction of thin, warming clouds (Figure 8c). To calculate λ_P, I multiply changes in $P(I)$ with $C(I)$ (Eq. 8). In the ICON simulations, thin clouds with a positive $C(I)$ reduce most relative to thick clouds with a negative $C(I)$, giving rise to a neutral to weakly negative λ_P (Figure 8d). In the RCEMIP simulations and all satellite observations, the positive feedback from a reduction of thick clouds with a negative $C(I)$ dominates, which results in a weakly positive λ_P.

My result of a small anvil-cloud amount feedback is confirmed by other recent studies, which makes the negative feedback from the WCRP assessment seem highly unlikely. Satellite observations (Raghuraman et al., 2024), theory (McKim et al., 2024) and models (Sokol et al., 2024; Wilson Kemsley et al., 2025) agree that λ_P is small. The ice water path framework facilitates the understanding of why λ_P is small by showing the cancellation of the positive feedback from a reduction of thick, cooling clouds and the negative feedback from a reduction of thin, warming clouds.

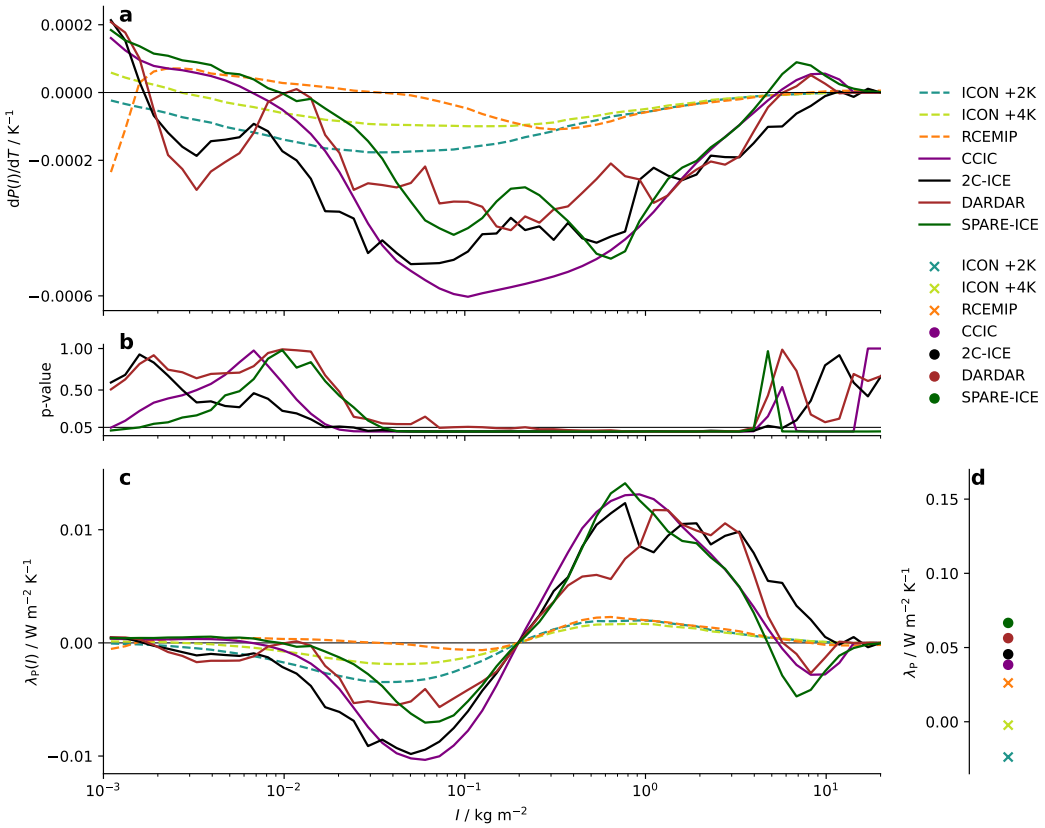


Figure 8: (**a**) Change of ice water path (I) frequency (P) per unit mean surface temperature (T) increase. Calculated via linear regressions of $P(I)$ on two-meter temperature T for the satellite observations, as the ensemble mean change in $P(I)$ from the RCEMIP simulations (Sokol et al., 2024) and as the change in $P(I)$ relative to the control simulation in ICON simulations. (**b**) P-value of the linear regression used to derive $\mathrm{d}P(I)/\mathrm{d}T$ from observations. (**c**) Feedback (λ_p) from changes in $P(I)$ as a function of I. (**d**) The total λ_P plotted on the same scale as Figure 6c and Figure 9c. All feedback values are global mean values.

5.3 DIURNAL CYCLE FEEDBACK

I find a previously unrecognised change in the diurnal cycle of deep convection that causes a positive SW feedback. This result from the ICON simulations is confirmed by internal variability within satellite observations.

The SW $C(I)$ becomes less negative at $I > 0.1$ kg m^{-2} in response to surface warming (Figure 9a), which results in a positive SW feedback (Figure 9b, c). The change in the SW $C(I)$ is much stronger than the change in the LW $C(I)$. However, the resulting SW λ_C is still of similar magnitude LW counterpart. The reason for this is that the change in the SW $C(I)$ grows large only for high I, which are less frequent, whereas the change in the LW $\Delta C(I)$ affects most I (Compare Figure 6 and Figure 9). Changes in the SW $C(I)$ at $I \leq 0.1$ kg m^{-2} depend on my definition for the separation of frozen and liquid clouds and are hence excluded from the diurnal cycle feedback.

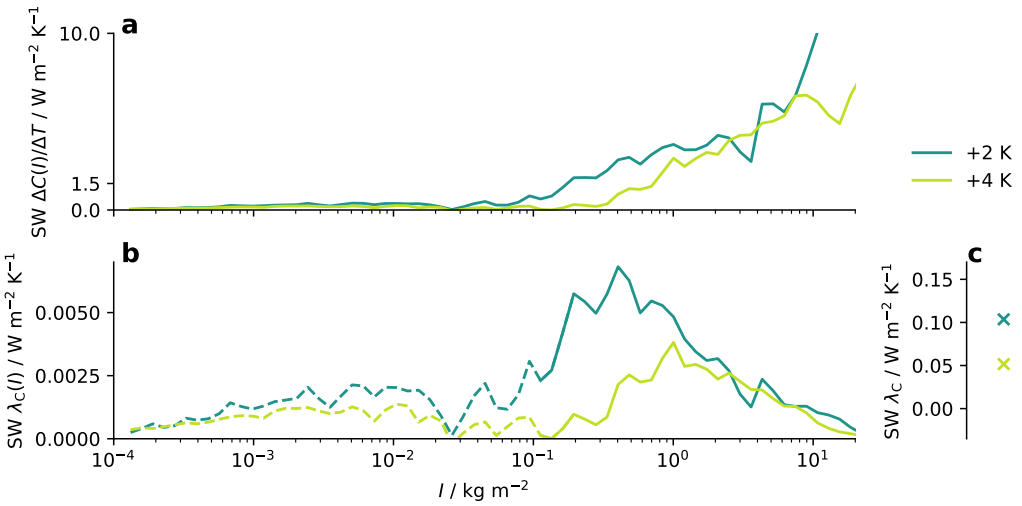


Figure 9: (**a**) Change in the SW high-cloud radiative effect (ΔC) per unit warming (ΔT) as a function of ice water path (I). (**b**) SW feedback from changes in C (λ_C) as a function of I. Dotted values of the SW $\lambda_C(I)$ are not included for the total SW λ_C. (**c**) Total SW λ_C plotted on the same scale as Figure 6c and Figure 8d. All feedback values are global mean values.

That the SW $C(I)$ becomes less negative in response to surface warming is caused by a change in the diurnal cycle of deep convection. Deep convection occurs less frequently during the day and more frequently during the night as the surface warms. Therefore, thick high clouds receive less SW radiation and hence reflect less, which reduces the magnitude of their SW $C(I)$.

I use CCIC to test whether the diurnal cycle of deep convection and its response to warming in ICON is realistic. I limit the set of satellite observations to CCIC since it is the only I retrieval that samples the diurnal cycle. I analyse the diurnal cycle of deep convection and its response to warming by calculating the fraction of deep convective clouds (f_d) with $I > 1$ kg m^{-2} as a function of local time.

The diurnal cycle of deep convection in the ICON aquaplanet simulations closely resembles the observed diurnal cycle over ocean (Figure 10a). The diurnal cycle of deep convection is much more muted over ocean than over land, which is in line with the scientific consensus (Hendon and Woodberry, 1993).

The partial shift of deep convection from daytime to nighttime in response to surface warming found in the ICON simulations is confirmed by internal variability within satellite observations (Figure 10b). The change in the diurnal cycle of deep convection is similar over land and ocean, which is surprising given the large differences in the mean diurnal cycle. The change in the diurnal cycle of deep convection is two to three times stronger in the observations compared to ICON. I perform a sanity check of the observed diurnal cycle change by calculating f_d directly from the brightness temperature observations on which CCIC is based. This test confirms the result from CCIC. My estimate of the SW λ_C from the observations is 0.12 ± 0.02 W m^{-2} K^{-1}, which is higher than both estimates from the ICON simulations (Figure 9c).

I speculate that intensified radiative heating might drive changes in the diurnal cycle of deep convection. Radiative heating is thought to control the diurnal cycle

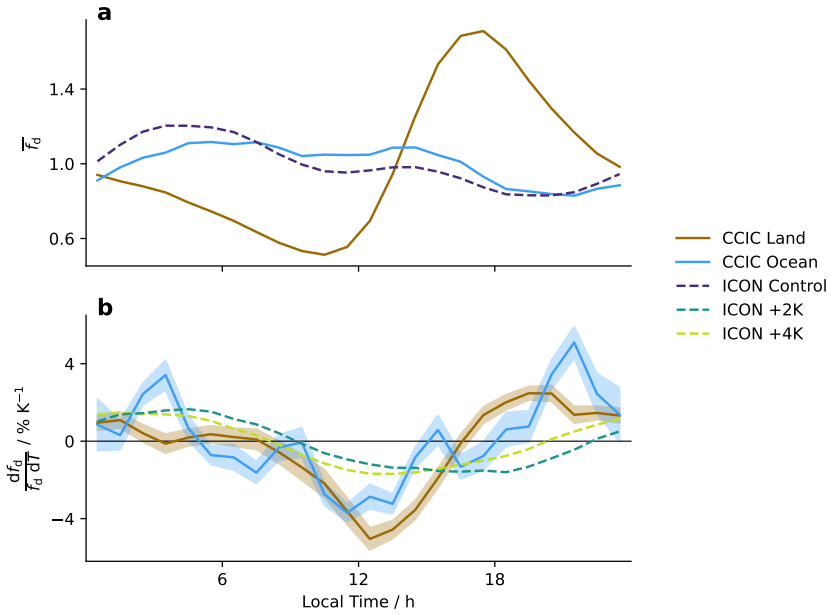


Figure 10: (**a**) Normalised deep convective cloud fraction ($\overline{f_d}$) as a function of local time from CCIC over land and ocean and from the ICON control simulation. (**b**) Change in the diurnal cycle of f_d per unit mean surface temperature (T) increase. Shading marks the standard error of the regression.

of deep convection in two ways: first by acting directly on the clouds in the form of cloud radiative heating (Kraus, 1963; Xu and Randall, 1995), and second by causing subsidence in clear-sky regions via radiative cooling, which needs to be balanced by updrafts in convective regions (Ruprecht and Gray, 1976; Gray and Jacobson, 1977). During the night, radiative heating favours deep convection. Radiative cooling of the cloud tops throughout the night decreases atmospheric stability, and clear-sky radiative cooling causes subsidence that must be balanced by convection (Ruppert and Hohenegger, 2018). During the day, radiative heating suppresses deep convection. Solar radiation reduces the clear-sky cooling and heats the cloud tops, inhibiting deep convection in the afternoon (Ruppert and Hohenegger, 2018). Radiative heating rates (Q) are calculated as

$$Q = \frac{1}{\rho c_p} \frac{\partial F}{\partial z}, \tag{9}$$

where ρ is air density, c_p is specific heat capacity of air, F is the radiative flux and z is height. The vertical divergence of the radiative flux is invariant to surface temperature on isotherms, since it is tied to water vapour concentration, which is, to first order, a function of the local air temperature (Jeevanjee and Romps, 2018). However, the density decreases as the surface warms, since isotherms shift to lower pressure, which causes an increase in the magnitude of heating rates. This affects radiative heating in the clear-sky atmosphere (Jeevanjee and Fueglistaler, 2020; Hartmann et al., 2022), but similar physics explain an increase in radiative heating of high clouds (Gasparini et al., 2024). Given that radiative heating suppresses convection during the day and favours convection during the night, I hypothesise that the in-

creased magnitude of radiative heating drives the partial shift of deep convection from daytime to nighttime in response to surface warming.

Feedbacks from changes in the diurnal cycle of clouds have received limited attention. One reason might be that suitable models for studying them became available only recently. The widely used GCMs are not ready for this task, since they rely on parameterisations of convection, which produce an unrealistic diurnal cycle (Covey et al., 2016; Christopoulos and Schneider, 2021). This limitation was overcome recently with the development of GSRMs, which have a good representation of the diurnal cycle of convection (Stevens et al., 2020; Song et al., 2024). Another possible reason for the lack of studies on the feedback from changes in the diurnal cycle of clouds is that cloud radiative kernels, the common framework for analysing cloud feedbacks, do not account for the diurnal cycle. Cloud radiative kernels only resolve the seasonal cycle at a monthly timestep, but not the diurnal cycle (Zelinka et al., 2012a). This makes them easy to use since monthly means are sufficient as input, but it means that feedbacks from changes in the diurnal cycle of clouds are neglected.

6 HIGHER CLIMATE SENSITIVITY

The total tropical high-cloud feedback that I derive from ICON aquaplanet simulations and satellite observations is more positive than previous estimates, implying a higher climate sensitivity. In this chapter, I summarise my feedback estimates from simulations and satellite observations and derive the combined best estimate. I compare my estimates to the WCRP assessment and update their equilibrium climate sensitivity to reflect my best estimate of the tropical high-cloud feedback.

I assign equal weight to all lines of evidence (ICON, RCEMIP and satellites) for my best estimates of the different components of the tropical high-cloud feedback and adopt a conservative approach to calculate uncertainty. I average the feedback within every line of evidence and then take the mean across all lines of evidence as the best estimate. Uncertainty (ϵ) is defined as half the range of the feedback estimates:

$$\epsilon = \frac{\max(\lambda_x) - \min(\lambda_x)}{2}, \tag{10}$$

where x can be any feedback component. This simple but conservative metric allows me to combine the four different kinds of uncertainty that my results quantify: state dependence, quantified by difference between the feedback estimates from the ICON +2 K and the ICON +4 K simulations; measurement uncertainty, quantified by the spread between estimates of the anvil-cloud amount feedback derived from satellites; sampling uncertainty within the linear regression used to derive the diurnal cycle feedback from CCIC; and the spread between different lines of evidence. For the diurnal cycle feedback, the uncertainty range includes the CCIC sampling uncertainty, which is added to the mean CCIC estimate to determine the maximum value used in Eq. 10. The uncertainty of the total feedback is calculated as the root-sum-square of the individual components, assuming independence. Individual feedback estimates and the combined best estimates are summarised in Table 1 and Figure 11.

The high-cloud altitude feedback in the ICON aquaplanet simulations is at the upper end of the uncertainty range of the WCRP assessment (Figure 11). This discrepancy is explained by high-cloud temperatures remaining approximately fixed in ICON, while high clouds are slightly warming in the GCM simulations used for the WCRP estimate (Zelinka et al., 2016; Ceppi et al., 2017). A more positive high-cloud altitude feedback seems more realistic, since part of the high-cloud warming in GCMs is explained by their unrealistic treatment of ozone (Chapter 5.1).

Satellite observations, RCEMIP simulations and ICON aquaplanet simulations agree that the anvil-cloud amount feedback is small rather than negative (Figure 11). I find that the anvil-cloud amount reduces in response to surface warming, but the resulting feedback is small since the positive feedback from a reduction of thick, cooling clouds is cancelled by the negative feedback from a reduction of thin, warming clouds (Chapter 5.2). A small anvil-cloud amount feedback is confirmed

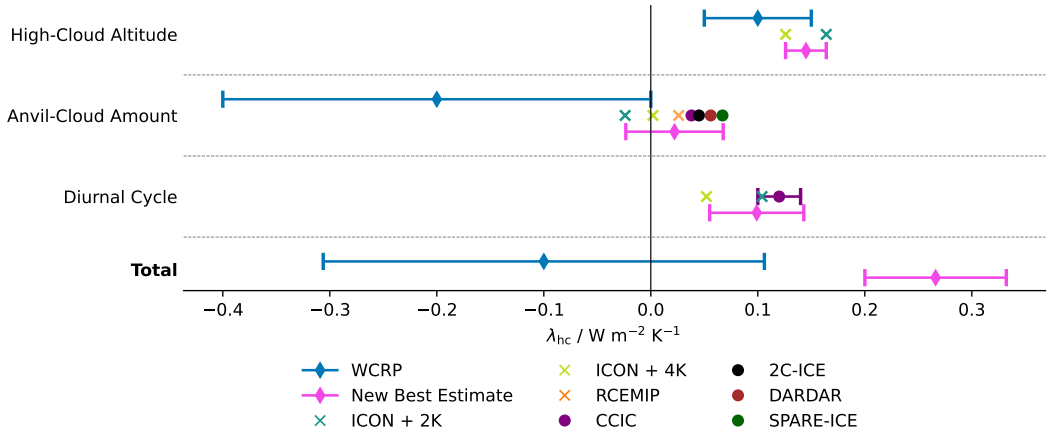


Figure 11: Tropical high-cloud feedback (λ_{hc}) from the WCRP assessment (Sherwood et al., 2020) and estimates derived in this thesis. I derive the tropical high-cloud altitude feedback from the WCRP value that includes all latitudes and calculate the uncertainty of the total feedback from the WCRP assessment as the root-sum-square of the individual uncertainties. I show all individual feedback estimates derived in this thesis and the combined best estimate. The individual estimates are single values, except for the CCIC estimate of the diurnal cycle feedback, which includes an uncertainty range. All feedback values are global mean values.

by other recent studies, making the WCRP estimate seem highly unlikely (McKim et al., 2024; Sokol et al., 2024; Raghuraman et al., 2024; Wilson Kemsley et al., 2025). The cumulating evidence for a small anvil-cloud amount feedback may help to settle more than two decades of discussion on whether this feedback is strongly negative, ignited by Lindzen et al. (2001).

The positive diurnal cycle feedback that I find in the ICON simulations and satellite observations is a new component of the tropical high-cloud feedback that was unknown at the time of the WCRP assessment. Deep convection in the tropics becomes less frequent during the day and more frequent during the night in response to surface warming, causing a decrease in albedo and hence a positive feedback (Chapter 5.3). This feedback is of similar magnitude as the high-cloud altitude feedback, and hence significantly contributes to the total tropical high-cloud feedback (Figure 11).

Overall, my results suggest that the tropical high-cloud feedback is strongly positive rather than weakly negative as previously assumed, implying a higher climate sensitivity. My best estimate of the tropical high-cloud feedback is 0.27 W m^{-2} K^{-1}, while the central estimate from the WCRP assessment is -0.1 W m^{-2} K^{-1}. The total climate feedback parameter from the WCRP assessment is -1.3 W m^{-2} K^{-1}. Together with their estimate of the radiative forcing from a doubling of CO_2 of 4 W m^{-2}, this gives an equilibrium climate sensitivity of 3.1 K (Eq. 1). The updated climate feedback parameter that accounts for my estimate of the tropical high-cloud feedback is -0.93 W m^{-2} K^{-1}, which yields an equilibrium climate sensitivity of 4.3 K. This is a significant increase, but still within the range of previous estimates. My updated estimate of the equilibrium climate sensitivity is at the upper end of

the 90% probability ranges from the WCRP assessment ($2.3 - 4.7$ K) and the latest IPCC report ($2 - 5$ K) (Forster et al., 2021).

Feedback	Source	Value / W m^{-2} K^{-1}
High-Cloud Altitude	ICON +2 K	0.16
	ICON +4 K	0.13
	Combined	0.15 ± 0.02
Anvil-Cloud Amount	ICON +2 K	-0.02
	ICON +4 K	0.00
	RCEMIP	0.03
	CCIC	0.04
	2C-ICE	0.05
	DARDAR	0.06
	SPARE-ICE	0.07
	Combined	0.02 ± 0.05
Diurnal Cycle	ICON +2 K	0.10
	ICON +4 K	0.05
	CCIC	0.12 ± 0.2
	Combined	0.10 ± 0.04
Total	Combined	0.27 ± 0.07

Table 1: Tropical high-cloud feedback estimates derived in this thesis, along with the combined best estimate. All feedback values are global mean values.

The close agreement from different lines of evidence on a positive tropical high-cloud feedback suggests a reduced uncertainty. Despite my conservative estimate of uncertainty, the uncertainty of the tropical high-cloud feedback is much reduced compared to the WCRP assessment (Figure 11). However, this comparison should be interpreted with caution, as my estimate is based solely on the results presented here, whereas the WCRP range is based on an expert assessment of the full body of evidence available at the time. A new expert assessment would be necessary to decide whether my results, together with other recent studies cited above, allow for a more constrained estimate of the tropical high-cloud feedback. The close agreement of satellite observations and simulations that I find makes this seem plausible.

7

CLOSING THOUGHTS

7.1 SUMMARY

I resolve the spectrum of tropical high clouds, ranging from thick deep convective clouds to thin cirrus, to analyse the tropical high-cloud feedback. Sorting tropical high clouds by ice water path as a measure of cloud thickness allows me to distinguish cloud types governed by different physics and to resolve how cloud thickness determines the high-cloud radiative effect. The high-cloud radiative effect is positive for thin clouds and negative for thick clouds. Resolving this dependence of the high-cloud radiative effect on cloud thickness is crucial for understanding the feedback from changes in cloud amount. Applying the ice water path perspective to global storm-resolving ICON aquaplanet simulations and satellite observations reveals that the high-cloud feedback is positive, rather than negative as estimated by the WCRP, implying a higher climate sensitivity. I find three components of the tropical high-cloud feedback, ranging from previously known to newly identified: a positive feedback from the isothermal rise of high clouds to higher altitude, a small feedback from the reduction of anvil clouds and a positive feedback from changes in the diurnal cycle of deep convection.

High clouds of any thickness rise to higher altitudes to remain at fixed temperatures in response to surface warming in the ICON simulations, producing a positive feedback by masking the Planck feedback. Such an isothermal rise of high clouds is in agreement with the FAT theory (Hartmann and Larson, 2002), but disagrees with results from GCMs, which predict a warming of high clouds of 0.33 K per K surface warming (Zelinka et al., 2016; Ceppi et al., 2017). I show that part of the high-cloud warming found in GCMs is explained by their unrealistic treatment of ozone. Ozone is prescribed to remain constant on pressure levels in these GCMs (Taylor et al., 2012; Eyring et al., 2016), while my ICON simulations use an interactive ozone scheme. If I instead prescribe ozone like in the GCMs, the high-cloud temperature change shifts from -0.06 K K^{-1} (interactive ozone) to 0.09 K K^{-1} (prescribed ozone). The high-cloud altitude feedback diagnosed from the ICON simulations with interactive ozone is at the upper end of the uncertainty range from the WCRP assessment, which is based on GCM simulations. This is a direct consequence of fixed high-cloud temperatures in ICON, rather than the slight warming predicted by GCMs.

Anvil clouds reduce in response to surface warming as expected from the stability iris theory (Bony et al., 2016), but the resulting feedback is near-neutral, and not negative as previously assumed (Sherwood et al., 2020; Forster et al., 2021). The reduction of anvil clouds in response to warming is captured by ICON aquaplanet and RCEMIP simulations, and confirmed by internal variability within satellite observations of ice water path. The magnitude of this reduction is two to three times larger in the observations compared to the simulations. Nevertheless, the resulting feedback is small in both observations and simulations, since the reduction of thick,

cooling clouds is cancelled by the reduction of thin, warming clouds in all datasets. The satellites and RCEMIP simulations yield a weakly positive feedback because the reduction of thick, cooling clouds predominates, while the ICON simulations have a neutral to weakly negative feedback since thin, warming clouds reduce more. A small anvil-cloud amount feedback is confirmed by other recent studies (Sokol et al., 2024; McKim et al., 2024; Raghuraman et al., 2024; Wilson Kemsley et al., 2025), making the negative feedback value from the WCRP assessment seem highly unlikely.

Deep convection partly shifts from daytime to nighttime in response to surface warming, causing a decrease in albedo and hence a positive feedback. This change in the diurnal cycle of deep convection that I first found in the ICON simulations is confirmed by internal variability in satellite observations of ice water path. While the observed diurnal cycle of deep convection is much more pronounced over land than over ocean, its change in response to surface warming is similar over land and ocean. I speculate that this partial shift of deep convection from daytime to nighttime might be caused by an increase in the magnitude of radiative heating. As the surface warms, the radiative heating at a given isotherm increases since the isotherm shifts to lower pressure and hence lower density. While the flux divergence stays constant at a given isotherm (Jeevanjee and Romps, 2018), density decreases, which results in an increased magnitude of radiative heating in clear-sky (Hartmann et al., 2022) and cloudy regions (Gasparini et al., 2024). Radiative heating favours deep convection during the night, but suppresses it during the day (Ruppert and Hohenegger, 2018). Therefore, it seems reasonable that an increased magnitude of radiative heating in response to surface warming causes a reduction of deep convection during the day, and an increase during the night. Such feedbacks from changes in the diurnal cycle of clouds have received limited attention. One reason for this is that cloud radiative kernels, as the main framework for diagnosing cloud feedbacks, do not resolve the diurnal cycle (Zelinka et al., 2012a). Another reason is that GCMs do not have a realistic representation of the diurnal cycle of convection (Covey et al., 2016; Christopoulos and Schneider, 2021). Therefore, the analysis of the diurnal cycle of clouds has only been enabled recently by the development of GSRMs, which have a realistic representation of the diurnal cycle (Stevens et al., 2020; Song et al., 2024).

Overall, satellite observations of ice water path and the ICON aquaplanet simulations yield a positive tropical high-cloud feedback of 0.27 ± 0.07 W m^{-2} K^{-1} rather than the negative feedback of -0.1 ± 0.21 W m^{-2} K^{-1} estimated by the WCRP, implying a higher climate sensitivity. When updated for my estimate of the tropical high-cloud feedback, the equilibrium climate sensitivity increases from 3.1 K to 4.3 K.

7.2 LOOKING FORWARD

I think science is rarely complete, and this thesis is no exception. Some of my hypotheses remain untested; the comparability of the high-cloud response diagnosed from different kinds of surface warming requires some thought; and my results should be tested with more realistic simulations.

My proposed heating-rate mechanism for the change in the diurnal cycle of deep convection should be tested. Idealised simulations might be the right tool for this. Simulations of RCE reduce the complexity of atmospheric convection to a minimum

but still capture the balance between convective heating and radiative cooling of the atmosphere, which is necessary to test the heating rate mechanism. Therefore, RCE simulations with a diurnal cycle of insolation might be the simplest simulations suitable for testing the heating-rate mechanism. The heating-rate mechanism could be tested by increasing the magnitude of heating rates without changing the surface temperature. One way this could be achieved is by scaling the radiative heating rates.

It is unclear how well the response of high clouds to long-term warming can be compared to their response to warming from internal variability. I assume that the high-cloud response is similar for any kind of surface warming by comparing ICON simulations with a spatially uniform surface warming to internal variability within satellite observations. While this comparison generally yields good qualitative agreement between models and simulations, the magnitude of the high-cloud response to warming is stronger when diagnosed from internal variability within the satellite observations. A stronger response of high clouds to warming from internal variability than to the long-term warming is found in GCMs. McKim et al. (2024) use the results from Saint-Lu et al. (2022) to argue that the reduction of tropical anvil clouds in response to the long-term warming is about half as strong as the reduction in response to warming from internal variability. A similar ratio was found for the high-cloud altitude feedback diagnosed from the long-term warming compared to the feedback diagnosed from internal variability (Vaillant de Guélis et al., 2018). It remains unclear whether this scaling is similar for the change in the ice water path frequency and the change in the diurnal cycle of deep convection. Answering this would require more realistic GSRM simulations spanning at least one full ENSO cycle and including a transient warming trend.

More realistic GSRM simulations are also necessary to test how my results are affected by the added complexity from land, varying SSTs and the seasonal cycle. The third phase of the DYnamics of the Atmospheric general circulation Modeled On Non-hydrostatic Domains (DYAMOND) project (Takasuka et al., 2024) will include such simulations. Year-long simulations in the current climate with observed SSTs as boundary conditions, and for a +4 K uniform SST increase, are planned to be carried out with a range of different GSRMs. However, instantaneous model output of ice water path is not planned to be included, which would be necessary for my analysis.

The ice water path framework that I use to diagnose the tropical high-cloud feedback allows for new insights, but the traditional method of cloud radiative kernels has the advantage that it cleanly separates clear-sky effects from the cloud feedback. I use the change in the cloud radiative effect as a measure of the high-cloud altitude feedback and the diurnal cycle feedback. This approach results in small but non-negligible biases compared to the true cloud feedback, defined as the radiative change caused by cloud properties in isolation (Soden et al., 2004). The bias is strongest for the LW cloud feedback, which is underestimated when diagnosed as the change in the cloud radiative effect. This bias is caused by the increase in atmospheric water vapour in response to warming, decreasing the clear-sky outgoing LW radiation, and hence the LW cloud radiative effect. Therefore, I underestimate the high-cloud altitude feedback. This does not affect my conclusions, since my estimate of the high-cloud altitude feedback is still higher than the WCRP estimate. I

explain this difference by high-cloud cloud temperatures staying approximately fixed in ICON, while they increase in GCMs. Cloud radiative kernels cleanly separate the cloud feedback from changes in the clear-sky atmosphere (Zelinka et al., 2012a) and will hence remain a valuable tool for diagnosing cloud feedbacks. I have two suggestions for how cloud radiative kernels could be improved for diagnosing the high-cloud feedback: by using temperature as the vertical coordinate rather than pressure, and by resolving the diurnal cycle. The first would make the altitude feedback simpler to understand since the change in high-cloud temperature determines its magnitude, not pressure. The latter would allow for capturing the diurnal cycle feedback.

A new synthesis of the research on climate sensitivity in the style of an IPCC report or the WCRP assessment is necessary to put my results into context. My results alone suggest a significant increase in equilibrium climate sensitivity from a positive tropical high-cloud feedback. However, other constraints on climate sensitivity, e.g. from paleoclimate records or observed trends, must be taken into account to derive a new estimate of climate sensitivity. Such a synthesis is also necessary to decide whether my results contribute to a reduction of uncertainty in climate sensitivity. The good agreement between satellite observations and the ICON aquaplanet simulations on a positive tropical high-cloud feedback makes this seem likely.

7.3 CONCLUSION

I resolve the spectrum of tropical high clouds, reaching from thick deep convective clouds to thin cirrus, which proves necessary to understand why the tropical high-cloud feedback is positive. I find a positive feedback from the isothermal rise of all high clouds to higher altitude, a small feedback from the reduction of anvil clouds and a positive feedback from a change in the diurnal cycle of deep convection.

Among all three components of the tropical high-cloud feedback, only the high-cloud altitude feedback was well understood before this thesis. Resolving the spectrum of high clouds is not necessary to capture the positive high-cloud altitude feedback, since all high clouds rise to higher altitude near-isothermally. Therefore, it appears as a robust feature in GCMs (e.g. Zelinka et al., 2016; Ceppi et al., 2017) confirmed by satellite observations (Zelinka and Hartmann, 2011; Vaillant de Guélis et al., 2018). Only the exact magnitude of the high-cloud altitude feedback remains disputed. I show that it might be more positive than the estimate from GCMs, since their treatment of ozone is unrealistic.

The anvil-cloud amount feedback was long misinterpreted to be negative (Lindzen et al., 2001; Sherwood et al., 2020; Forster et al., 2021). By resolving the spectrum of high clouds, I show that the anvil-cloud amount feedback is small, because the positive feedback from a reduction of thick, cooling clouds is cancelled by the negative feedback from a reduction of thin, warming clouds. I find this to be true in ICON aquaplanet simulations and satellite observations. A small anvil-cloud amount feedback is confirmed by other recent studies (McKim et al., 2024; Sokol et al., 2024; Raghuraman et al., 2024; Wilson Kemsley et al., 2025).

I find a positive diurnal cycle feedback as a new component of the tropical high-cloud feedback. This feedback results from a partial shift of deep convection from daytime to nighttime in response to surface warming, which I find in ICON aqua-

planet simulations and satellite observations. Capturing the change in the diurnal cycle of deep convection requires resolving both the spatial scale of deep convection and the temporal scale of the diurnal cycle, which is not the case in previous studies (e.g. Ceppi et al., 2017; Zelinka et al., 2022; Raghuraman et al., 2024).

The mechanisms governing the response of tropical high clouds to surface warming are all linked to the thermal expansion of the warming troposphere and the resulting change in radiative heating (and cooling). Hartmann and Larson (2002) first established the link between radiative cooling in clear-sky regions and high clouds. They show that radiative cooling is, to first order, a function of temperature since it depends on the amount of water vapour. Therefore, radiative cooling will follow the thermal expansion of the troposphere, requiring convective heating and hence high clouds to follow. The stability iris theory (Bony et al., 2016) links the decrease in detrained anvil clouds to the expansion of the troposphere by explaining it with the decrease in clear-sky subsidence from radiative cooling. As the troposphere warms and expands, the clear-sky radiative cooling profile isothermally shifts to higher altitude, where the same radiative cooling is balanced by less subsidence since the atmospheric stability is increased. The heating-rate mechanism that I propose as an explanation for the change in the diurnal cycle of deep convection is based on the same physics. The expansion of the troposphere causes an increase in the magnitude of radiative heating, both in clear-sky and cloudy regions, since the density at a given temperature decreases (Hartmann et al., 2022; Gasparini et al., 2024). Radiative heating favours convection during the night and inhibits convection during the day (Ruppert and Hohenegger, 2018). Therefore, I speculate that the increase in the magnitude of heating rates might explain the partial shift of deep convection from daytime to nighttime.

My analysis of the tropical high-cloud feedback shows that some things fall into place if the relevant scales are resolved. It is simple to understand that the anvil-cloud amount feedback is small due to the cancellation of the positive feedback from a reduction of thick, cooling clouds, and the negative feedback from a reduction of thin, warming clouds, but this insight requires cloud thickness to be resolved. It is also straightforward to see that a reduction in daytime clouds lowers the albedo and causes a positive feedback, but it requires convection and its diurnal cycle to be resolved. Therefore, this thesis underlines that predictive skill and conceptual understanding can be increased by abandoning the scale separation of GCMs to resolve the atmosphere at a horizontal grid spacing of $\mathcal{O}(1\ \mathrm{km})$ (Shaw and Stevens, 2025). This transition is fuelled by the increase in computational resources, enabling new tools like the ones used in my thesis: GSRMs and satellite retrievals based on machine learning algorithms.

Limited knowledge about the cloud response to surface warming remains the main cause for uncertainty in climate sensitivity (Sherwood et al., 2020; Forster et al., 2021), but my results suggest that this might be overcome by harnessing the synergy of GSRMs and satellite observations. Both GSRMs and satellite observations resolve clouds with a horizontal grid spacing of $\mathcal{O}(1\ \mathrm{km})$, allowing for a direct comparison. Internal variability within satellite observations confirms my findings from GSRM simulations, increasing confidence in my result of a positive tropical high-cloud feedback. Previous assessments of the tropical high-cloud feedback found it to be nega-

tive, but highly uncertain (Sherwood et al., 2020; Forster et al., 2021). Therefore, my result of a positive tropical high-cloud feedback implies a higher climate sensitivity.

Part II

APPENDIX

A

INSIGHTS ON TROPICAL HIGH-CLOUD RADIATIVE EFFECT FROM A NEW CONCEPTUAL MODEL

This paper was published as:
J. Deutloff, S. A. Buehler, M. Brath, and A. K. Naumann (2025a). "Insights on Tropical High-Cloud Radiative Effect From a New Conceptual Model." In: *Journal of Advances in Modeling Earth Systems* 17.2, e2024MS004615. DOI: 10.1029/2024MS004615

Author Contributions: Together with all co-authors, I conceptualised the study. S. A. Buehler and A. K. Naumann supervised the study. M. Brath ran the radiative transfer simulations. I conducted the analysis and wrote the manuscript with input from all co-authors.

Insights on Tropical High-Cloud Radiative Effect from a New Conceptual Model

Jakob Deutloff[1,2], Stefan A. Buehler[1], Manfred Brath[1], Ann Kristin Naumann[1,3]

[1]Center for Earth System Research and Sustainability (CEN), Meteorological Institute, Universität Hamburg, Hamburg, Germany
[2]International Max Planck Research School on Earth System Modelling (IMPRS-ESM), Hamburg, Germany
[3]Max Planck Institute for Meteorology, Hamburg, Germany

KEY POINTS

- The complexity of tropical high-cloud radiative effect is reduced by conceptualising it as a function of the ice water path.
- High clouds within our model simulation are characterised by a weakly positive high-cloud radiative effect.
- Low clouds render the high-cloud radiative effect positive.

ABSTRACT

The new capabilities of global storm-resolving models to resolve individual clouds allow for a more physical perspective on the tropical high-cloud radiative effect and how it might change with warming. In this study, we develop a conceptual model of the high-cloud radiative effect as a function of cloud thickness measured by ice water path. We use atmospheric profiles from a global ICON simulation with 5 km horizontal grid spacing to calculate the radiation offline with the ARTS line-by-line radiative transfer model. The conceptual model of the high-cloud radiative effect reveals that it is sufficient to approximate high clouds as a single layer characterised by an albedo, emissivity and temperature, which vary with ice water path. The increase of the short-wave high-cloud radiative effect with ice water path is solely explained by the high-cloud albedo. The increase of the long-wave high-cloud radiative effect with ice water path is governed by an increase of emissivity for ice water path below 10^{-1} kg m^{-2}, and by a decrease of high-cloud temperature with increasing ice water path above this threshold. The mean high-cloud radiative effect from the ARTS simulations for the chosen day of this ICON model run is 1.25 W m^{-2}, which is closely matched by our conceptual model with 1.26 W m^{-}2. Because the high-cloud radiative effect depends on the assumed radiative alternative, assumptions on low clouds make a substantial difference. The conceptual model predicts that doubling the fraction of low clouds roughly doubles the positive high-cloud radiative effect.

PLAIN LANGUAGE SUMMARY

High clouds are widespread within the tropics and can either amplify or dampen global warming if they change in a way that affects their ability to reflect solar or absorb terrestrial thermal radiation. To better understand how high clouds within the tropics might influence global warming, we use high-resolution climate models that are able to resolve individual clouds. Those models allow us to interpret the effect of high clouds on solar and thermal radiation as a function of the cloud thickness. To better understand this dependence, we develop a conceptual model of high clouds that breaks the physical mechanisms down to their main parts. The conceptual model shows that high clouds can be well approximated as a single layer whose reflectivity, temperature and transparency to thermal radiation depend on the cloud thickness. We find that high clouds are slightly warming the Earth in the current climate, which is well reproduced by the conceptual model. The conceptual model reveals that if more low clouds exist below the high clouds, the warming effect of high clouds is increased.

A1 INTRODUCTION

Cloud feedbacks remain to contribute most to the uncertainty in climate sensitivity among all feedback processes (Arias et al., 2021). Splitting up the cloud feedback into its subcomponents reveals that the major part of the net uncertainty associated with it stems from tropical high clouds (Sherwood et al., 2020). They can produce a climate feedback if their radiative effect changes in response to surface warming. To reduce the uncertainty within the tropical high-cloud feedback, it is therefore necessary to understand what controls the tropical high-cloud radiative effect (C) and how it might change with warming, which is the aim of this study.

Most analysis of tropical high-cloud feedbacks is based on global circulation models (GCMs) with horizontal resolutions $\mathcal{O}(100\ \mathrm{km})$ (Bony et al., 2016; Mauritsen and Stevens, 2015). Since GCMs are not able to resolve individual clouds, they predict the fraction of a grid cell covered with clouds. This has led to the notion of approximating high clouds to be uniform with an average albedo, emissivity, altitude and extent (McKim et al., 2024). The common analysis of the high-cloud feedback is based on this approximation. Therefore, the high-cloud feedback is often decomposed into an altitude, amount and optical thickness contribution (Sherwood et al., 2020; McKim et al., 2024; Zelinka et al., 2022). The high-cloud altitude feedback is expected to be positive, since tropical high clouds will rise and warm less than the surface in case of global warming and thereby mask the Planck feedback. This hypothesis is referred to as the proportionally higher anvil temperature (PHAT) mechanism (Zelinka and Hartmann, 2010). Similar thermodynamic arguments suggest that the tropical high-cloud amount will decrease, resulting in a negative feedback, which is referred to as the stability iris (Bony et al., 2016). Changes in high-cloud optical thickness have the potential for a strong feedback, but remain unconstrained (McKim et al., 2024).

This decomposition of the high-cloud feedback rests on the assumption of an average C, which was found to be near-neutral (Hartmann, 2016) with single estimates ranging from to weakly negative to weakly positive ($-1.5\ \mathrm{W\ m^{-2}}$ found by McKim et al. (2024), $2\ \mathrm{W\ m^{-2}}$ found by L'Ecuyer et al. (2019)). However, satellite observations resolving the clouds at a much higher resolution than GCMs ($\mathcal{O}(5\ \mathrm{km})$) have shown that approximating high clouds to be uniform with an average C is highly inaccurate (Berry and Mace, 2014). The radiative properties of high clouds vary with the cloud thickness, which can be measured by the ice water path (I). Since I of high clouds spans several orders of magnitude, associated with very different C, neglecting this dependence risks missing important feedbacks that do not map onto the oversimplified coordinates of mean altitude, mean amount and mean optical thickness.

The development of global storm resolving models (GSRMs), with horizontal resolutions $\mathcal{O}(5\ \mathrm{km})$, makes it possible to resolve C as a function of I in global simulations. The usefulness of this perspective on model simulations has recently been shown by Sokol et al. (2024), who applied it to radiative-convective equilibrium simulations. With this study, we aim to harness the new capabilities of GSRMs to further develop the ice water path perspective on C. We show that this perspective is deeply rooted within the physics underlying C by constructing a conceptual model that explains the dependence of C on I. This conceptual model reduces the complexity of C signif-

icantly, and hence provides a framework to evaluate the high-cloud feedback within warming GSRM simulations, which can replace the overly simplistic decomposition that was made for GCMs. Resolving C as a function of I allows to understand how the contribution of high clouds with a specific I to the mean C is governed by their $C(I)$ as well as their frequency of occurrence. We believe that this ice water perspective on the high-cloud radiative effect can provide new insights about the high-cloud feedback beyond the established decomposition.

After presenting our model setup in section A2, we explain how C can be interpreted as a function of I in section A3. We use this perspective to construct the conceptual model of $C(I)$ (Sec. A4), which helps us to understand its key ingredients (Sec. A5). The role of low clouds for C is investigated in section A6. We give an outlook on how the conceptual model can be useful for analysing high-cloud feedbacks in section A7, before we conclude with section A8. We explain our methods in depth in section A9.

A2 MODEL SETUP

Our conceptual model rests upon the development of global storm-resolving models (GSRMs) which explicitly resolve deep convection in the tropics. In particular, we use instantaneous atmospheric profiles from global simulations with the ICOsahedral Nonhydrostatic weather and climate model (ICON) (Hohenegger et al., 2023) with 5 km horizontal grid spacing. Microphysical processes within ICON are parameterized with a one-moment scheme, which distinguishes five hydrometeors: cloud water, rain, cloud ice, snow, and graupel. (Baldauf et al., 2011). ICON is forced with pre-industrial sea surface temperature from CMIP6 models and run for 6 months (Kluft, 2023). Operating at such a fine horizontal resolution, ICON is able to resolve individual clouds (Fig. A12). However, ICON only calculates all-sky and clear-sky radiative fluxes. While this data can be used to calculate the total cloud radiative effect, it does not allow for making a distinction between overlapping clouds of different types. Therefore, we calculate the radiative fluxes offline with the line-by-line Atmospheric Radiative Transfer Simulator (ARTS) (Buehler et al., 2018) to isolate the radiative effect of high clouds. This setup allows us to switch the radiative effect of high clouds off in the radiative transfer calculations to better study the radiative effect of high clouds over low clouds.

Since the radiative transfer simulations with ARTS are computationally expensive, we subsample atmospheric profiles on a 1° by 1° grid from one timestep (01.08. 12:00 UTC) of ICON data at native resolution. This subset of 64,800 profiles is used to calculate radiative fluxes with ARTS for three different setups: ARTS-allsky including all clouds, ARTS-clearsky including no clouds, and ARTS-lowcld including only liquid hydrometeors. We use the ARTS configuration introduced by Brath et al. (2024), which describes the optical properties of frozen hydrometeors as follows: cloud ice is assumed as hexagonal columns and follows the size distribution specified by (Geer and Baordo, 2014), snow as 10-plate-aggregates with the size distribution from Field et al. (2007) and graupel as droxtals with the size distribution from (Doms et al., 2021). Since ARTS is a spectrally resolving radiative transfer model, we prescribe a frequency grid for its simulations. We use 10,000 frequencies which

are linearly spaced from 10 cm^{-1} to $5 \cdot 10^3$ cm^{-1} to calculate the radiative transfer in the long-wave regime and another 10,000 frequencies spaced logarithmically from 10^3 cm^{-1} to 10^5 cm^{-1} for the short-wave regime. The distribution of I is calculated from the same ICON timestep, but without subsampling. We limit our analysis to the tropics (30°S to 30°N), which are associated with deep convection whose detrained cloud condensate forms into high clouds.

A3 ICE WATER PATH FRAMEWORK

The basic idea of the ice water path framework is to treat the radiative properties of high clouds as a function of the cloud thickness, approximated by I, the vertical integral of the sum of all frozen hydrometeors (cloud ice, snow, and graupel). This perspective unravels how the net high-cloud radiative effect changes from positive to negative with increasing I (Fig. A13). For the radiative effect of all high clouds, not only $C(I)$ is important, but also the frequency of occurrence of I ($P(I)$). The product of $C(I)$ and $P(I)$ shows the relative importance of high clouds with a specific I for the mean high-cloud radiative effect $\overline{C}$, which is proportional to the area under the $C(I) \cdot P(I)$ curve.

We define high clouds as all clouds with cloud tops above 350 hPa. This includes frozen clouds as well as deep convective clouds which contain frozen and liquid hydrometeors. A similar definition is used by Haslehner et al. (2024), to avoid artificial separation of clouds which can occur if high clouds are defined as frozen clouds. To classify as part of a high cloud, we furthermore require the liquid cloud condensate to sufficiently overlap with the frozen cloud condensate in the vertical (Sec. A9.2). Any liquid clouds that are not part of a high cloud, we refer to as low clouds. According to this definition, we exclude frozen clouds with cloud tops below 350 hPa from our analysis, which make up for 14% of all frozen clouds.

Based on our definition of high clouds, we calculate C as the difference between the net radiative fluxes at TOA including the radiative effect of high clouds (F_{allsky}) and without the radiative effect of high clouds (F_{nohcld}):

$$C = F_{\mathrm{allsky}} - F_{\mathrm{nohcld}},$$

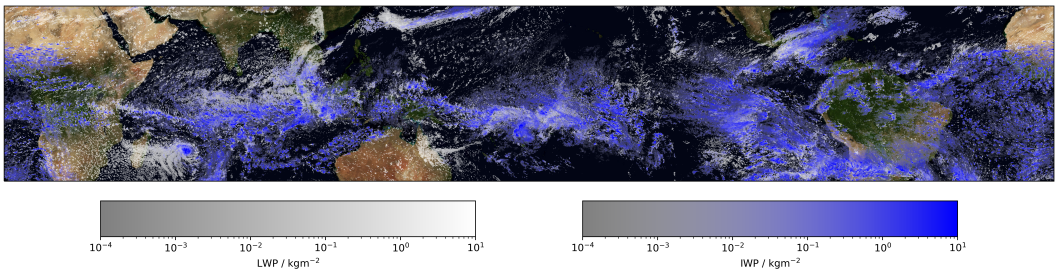


Figure A12: Clouds within ICON at the timestep used within this study. Liquid and frozen clouds are visualised by their liquid water path (LWP) and ice water path (IWP).

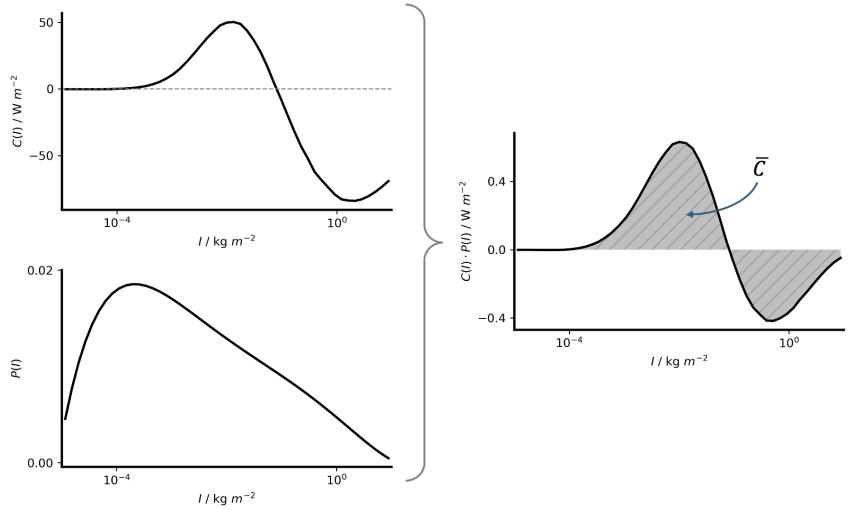


Figure A13: Schematic of how the mean high-cloud radiative effect ($\overline{C}$) is calculated from the net high-cloud radiative effect as a function of ice water path ($C(I)$) and the ice water path distribution ($P(I)$). $\overline{C}$ is proportional to the shaded area under the curve of $C(I) \cdot P(I)$.

where F_{nohcld} can originate from regions with low clouds or from clear-sky regions:

$$F_{\text{nohcld}} = \begin{cases} F_{\text{lowcld}}, & \text{if low cloud below,} \\ F_{\text{clearsky}}, & \text{if no cloud below.} \end{cases}$$

All radiative fluxes are co-located since they are calculated for the same grid points but with their respective ARTS setup. We split up the radiative spectrum into a LW and a SW contribution. The net value of C (C_{net}) is calculated as the sum of the SW (C_{SW}) and LW contributions (C_{LW}).

To simplify our analysis, we neglect the influence of the timing of convection on $C(I)$. It has been shown that the occurrence frequency of high clouds does vary over the day due to peaks of deep-convective activity in the morning (over ocean) and in the afternoon (over land) (Gasparini et al., 2022). This will affect $C(I)$, because if a certain I is more likely to occur during day than during night, the corresponding $C_{\text{net}}(I)$ will be more negative due to a stronger SW component. We neglect this dependence by assuming that every I is equally likely to occur at any time of the day. This simplification is necessary to keep the conceptual model of $C(I)$ sufficiently simple to allow for intuitive conclusions. To calculate $C(I)$ in agreement with this simplification, we bin C by I and longitude, interpolate this 2D field linearly and average over all longitudes to calculate $C(I)$. A similar simplification is made by Wall and Hartmann (2018), who show that the resulting bias in the mean $C_{\text{net}}(I)$ is negligible.

Sorting the atmospheric profiles by I allows us to link the thickness of high clouds to their radiative effect (Fig. A14). Since I spans several orders of magnitude, we interpret our results in $\log_{10}(I)$ space. This reveals that thick clouds characterised by high I which are typically part of deep convective towers exert a negative C_{net} since the negative SW dominates over the positive LW contribution. This balance shifts for anvil clouds of intermediate thickness at $I = 6 \cdot 10^{-2}$ kg m^{-2}, below which C_{net} is

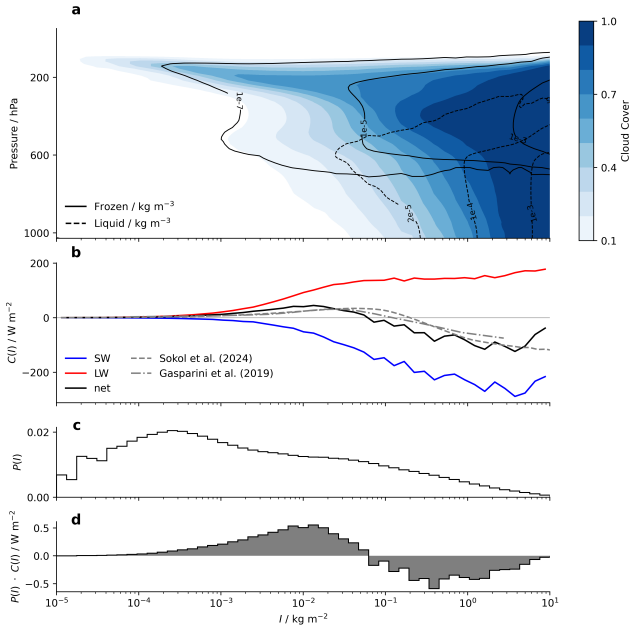


Figure A14: Filled contours of cloud cover and contour lines of frozen and liquid water content (a), Cloud radiative effect C from ARTS and the net C from Sokol et al. (2024) and Gasparini et al. (2019) (b), Ice water path distribution P from ICON (c) and the net C from ARTS weighted by P (d). All quantities are plotted against the ice water path I.

positive. The maximum C_{net} of 45 W m^{-2} occurs at $I = 1.3 \cdot 10^{-2}$ kg m^{-2}. Moving from this I towards lower values associated with thin cirrus clouds, C_{net} converges to zero.

The shape of $C_{\text{net}}(I)$ diagnosed by us is similar to estimates from radiative convective equilibrium (RCE) simulations and satellite observations, however the curves are shifted to higher I with the transition from positive to negative values occurring at: $I = 2 \cdot 10^{-1}$ kg m^{-2} for RCE (Sokol et al., 2024), and $I = 1.2 \cdot 10^{-1}$ kg m^{-2} for satellite observations (Gasparini et al., 2019). We assume that the lower sensitivity of C_{net} to I found by Gasparini et al. (2019) compared to ARTS is due to differences in horizontal resolution. The observed radiative fluxes used by Gasparini et al. (2019) to derive C have a horizontal resolution of 30 km, which is coarse compared to the 5 km of horizontal grid spacing used by us and can lead to the inclusion of clear-sky contributions in C_{net}, which would lower its sensitivity to I. The RCE models are run at 3 km horizontal grid spacing, hence we suspect that the differences in $C_{\text{net}}(I)$ compared to ARTS result from differences in how frozen hydrometeors are treated within the radiative transfer schemes. This disagreement gives rise to the question of how robust the mapping from frozen condensate mass to radiative fluxes is with respect to different assumptions about the optical properties of the hydrometeors. We are trying to answer that question within a different study by altering the optical properties of the hydrometeors assumed within ARTS (Sec. A2) to generate a model ensemble which allows us to quantify the resulting uncertainty in $C(I)$.

The distribution of I ($P(I)$), calculated as the fraction of profiles within the tropics covered by the respective I, reveals that thin high clouds with a weakly positive

C_{net} are more frequent than thick high clouds with a strongly negative C_{net}. At the maximum of P at $I = 3 \cdot 10^{-4}$ kg m^{-2}, we find $C_{\text{net}} = 4.2$ Wm^{-2}.

The mean high-cloud radiative effect ($\overline{C}$) is calculated as

$$\overline{C} = \sum_I C(I) \cdot P(I).$$

The usual weighting of gridcells with cos (latitude) is not necessary here since gridcells of ICON are to first order equal in area. Inspecting the product of $C(I)$ and $P(I)$ shows that both are equally important for $\overline{C}$. Thin clouds with a weakly positive $C_{\text{net}}(I)$ occur frequently enough to slightly overcompensate the contribution from less frequent thick high clouds with a strongly negative $C_{\text{net}}(I)$. Therefore, we find that high clouds in this ICON simulation are on average slightly warming the Earth with $\overline{C_{\text{net}}} = 1.25$ W m^{-2}. This is higher than the -1.5 Wm^{-2} estimated by McKim et al. (2024), but reasonably close to the 2 Wm^{-2} from L'Ecuyer et al. (2019), with both estimates relying on satellite observations. We hypothesize that the disagreement between our estimate and the one from McKim et al. (2024) is due to the fact that they do not properly account for the effect of overlapping low clouds in their study (Sec. A6).

A4 CONCEPTUAL MODEL OF THE HIGH-CLOUD RADIATIVE EFFECT

To understand what sets C and how it might change with warming, we develop a conceptual model that predicts C as a function of I to reduce the complexity of C to a minimum (Fig. A15). We approximate high clouds as a single layer characterised by cloud top temperature (T_{hc}), long wave emissivity (ε_{hc}) and short wave albedo (α_{hc}), which are functions of I. Anything below the high clouds is referred to as the lower troposphere (subscript t), which is characterised by an upward LW flux (R_{t}) and a short wave albedo (α_{t}). Both R_{t} and α_{t} are composed by a contribution from clear-sky regions and low clouds based on the low cloud fraction (f_{lc}). For $R_{\text{t}}(I)$, we furthermore introduce a correction term $C_{\text{H}_2\text{O}}(I)$ that accounts for the reduction of R_{t} with increasing I due to the moistening of the atmosphere that outweighs the increase in surface temperature.

For the LW radiation, we assume that R_{t} penetrates the high cloud depending on ϵ_{hc} and that the high cloud emits LW radiation to space with the same emissivity according to the Stefan-Boltzmann law. The all-sky LW flux at TOA ($F_{\text{LW,allsky}}$) is therefore given as

$$F_{\text{LW,allsky}}(I) = -(1 - \varepsilon_{\text{hc}}(I))R_{\text{t}}(I) - \varepsilon_{\text{hc}}(I)\sigma T_{\text{hc}}(I)^4,$$

with upward fluxes being defined as negative. To calculate $C_{\text{LW}}(I)$, we subtract the LW flux at TOA without high clouds ($\varepsilon_{\text{hc}} = 0$) from $F_{\text{LW,allsky}}$:

$$\begin{aligned} C_{\text{LW}}(I) &= \left[-(1 - \varepsilon_{\text{hc}}(I))R_{\text{t}}(I) - \varepsilon_{\text{hc}}(I)\sigma T_{\text{hc}}(I)^4\right] - \left[-R_{\text{t}}(I)\right] \\ &= \varepsilon_{\text{hc}}(I)\left(R_{\text{t}}(I) - \sigma T_{\text{hc}}(I)^4\right). \end{aligned} \tag{11}$$

For the SW radiation, we assume that the incoming solar radiation (S) penetrates the high cloud based on α_{hc}. The remaining SW radiation will experience multiple

reflections between the high cloud and the lower troposphere, which are described by a harmonic series that converges (Sec. A9.3). The all-sky SW flux at TOA ($F_{\mathrm{SW,allsky}}$) is therefore given as

$$F_{\mathrm{SW,allsky}} = S - S\left(\alpha_{\mathrm{hc}}(I) + \frac{\alpha_{\mathrm{t}}(1-\alpha_{\mathrm{hc}}(I))^2}{1-\alpha_{\mathrm{hc}}(I)\alpha_{\mathrm{t}}}\right)$$

To calculate C_{SW}, we subtract the SW flux at TOA without high clouds ($\alpha_{\mathrm{hc}} = 0$) from $F_{\mathrm{SW,allsky}}$:

$$\begin{aligned} C_{\mathrm{SW}}(I) &= \left[S - S\left(\alpha_{\mathrm{hc}}(I) + \frac{\alpha_{\mathrm{t}}(1-\alpha_{\mathrm{hc}}(I))^2}{1-\alpha_{\mathrm{hc}}(I)\alpha_{\mathrm{t}}}\right)\right] - [S - \alpha_{\mathrm{t}}S] \\ &= S\left(\alpha_{\mathrm{t}} - \alpha_{\mathrm{hc}}(I) - \frac{\alpha_{\mathrm{t}}(1-\alpha_{\mathrm{hc}}(I))^2}{1-\alpha_{\mathrm{hc}}(I)\alpha_{\mathrm{t}}}\right). \end{aligned} \tag{12}$$

For both SW and LW radiation we do not explicitly include emission and extinction from the atmosphere above high clouds.

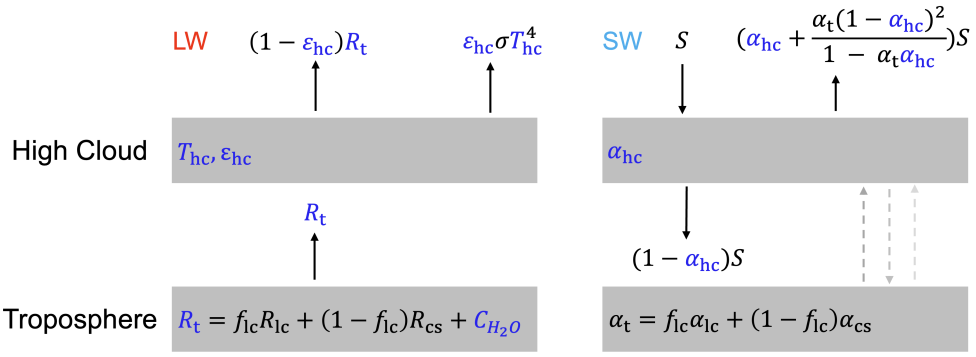


Figure A15: Schematic of the conceptual model, distinguishing between the short wave (SW) and long wave (LW) component of the high-cloud radiative effect. Variables that depend on I are marked in blue. See Table A3 for variable descriptions.

A5 KEY INGREDIENTS OF THE HIGH-CLOUD RADIATIVE EFFECT

We use the ARTS simulations to determine the free parameters of the conceptual model (Sec. A9.4). The shape of the mean of T_{hc} binned by I is closely linked to the cloud top height (compare Fig. A14a and Fig. A16a). The thickest clouds penetrate into the tropopause, resulting in cold cloud top temperatures. Clouds of intermediate thickness are generally lower and warmer, while the thinnest clouds are again found at higher, colder levels. We define $T_{\mathrm{hc}}(I)$ as the mean T_{hc} binned by I, since this relationship does not follow a clear functional form, which would allow for further simplification.

The mean values of $\varepsilon_{\mathrm{hc}}$ and α_{hc} binned by I follow an S-shape in the $\log_{10}(I)$ space, i.e., they approach zero for small I and a constant for large I with a transition for intermediate values (Fig. A16b and d). Therefore, we approximate $\varepsilon_{\mathrm{hc}}(I)$ and $\alpha_{\mathrm{hc}}(I)$ with logistic functions. Values of $\varepsilon_{\mathrm{hc}}$ higher than one can result from a bias of T_{hc}, or the approximation that LW radiation emitted by the high clouds escapes to space

without further atmospheric absorption (Fig. A15). Since the mean of ε_{hc} binned by I does not overshoot values of one significantly, we regard those simplifications to be acceptable (Fig. A16b). Besides of I, α_{hc} also depends on the incoming solar radiation (Fig. A16d). If the sun is closer to the horizon, the path of the SW radiation through the cloud and hence α_{hc} increase. We eliminate this dependency by calculating the daily mean α_{hc} (Sec. A9.4.3).

The radiative properties of the lower troposphere are governed by clear-sky regions and low clouds. The mean fraction of low clouds binned by I stays roughly constant for all I (Fig. A16c). Therefore, we approximate f_{lc} to be constant at the mean value of f_{lc} averaged over all I with $f_{lc} = 0.16$. Interestingly, the binned mean f_{lc} stays roughly constant even though the fraction of gridcells with LWP $> 10^{-4}$ kg m^{-2} increases strongly with I beyond $I > 10^{-1}$ kg m^{-2}. This means that high clouds contain increasingly more liquid condensate at high I, causing the fraction of low clouds to remain roughly constant.

Source	SW / Wm^{-2}	LW / Wm^{-2}	net / Wm^{-2}
ARTS	-28.64	29.89	1.25
Conceptual Model	-28.51	29.77	1.26

Table A2: $\overline{C}$ from the ARTS simulation and the conceptual model.

Based on f_{lc}, we calculate α_t as a composition of a clear-sky and a low-cloud contribution (Fig. A15). The rationale behind this approach is that we can distinguish between the high albedo of low clouds and the lower albedo of clear-sky regions (Fig. A16f). We use the same approach to describe how R_t is composed by a strong flux from clear-sky and a weaker flux from low cloud regions (Fig. A16e). However, the magnitude of R_t also depends on I. R_t decreases with I due to a moistening of the atmosphere that outweighs an increase in surface temperature. This decrease of R_t with I is approximated by the correction term C_{H_2O} that scales linearly with $\log_{10}(I)$ (Sec. A9.4.4).

Feeding those radiative properties of high-clouds and the lower troposphere into the conceptual model allows us to predict the high-cloud radiative effect (Eq. 11 and Eq. 12). The conceptual model seems to capture the main physics underlying $C(I)$, since it is able to reproduce the shape of $C(I)$ from the ARTS simulations (Fig. A16g). The agreement between $C(I)$ from ARTS and the conceptual model also shows in $\overline{C}$. The error of the conceptual model compared to ARTS is 0.45% for $\overline{C_{SW}}$, 0.4% for $\overline{C_{LW}}$, and 0.8% for $\overline{C_{net}}$ (Tab. A2). Since $\overline{C_{net}}$ is the small residual of two larger numbers, this low relative error in $\overline{C_{net}}$, which is the result of partial cancellation of errors in $\overline{C_{SW}}$ and $\overline{C_{LW}}$, is encouraging.

The conceptual model reduces the complexity of $C(I)$ significantly, and therefore allows to understand what governs the relationship between C and I. The increasingly negative C_{SW} towards high I is solely a result of the increase of α_{hc} with I. On the other hand, C_{LW} is governed by T_{hc} and ε_{hc}. The initial increase of C_{LW} up to $I = 10^{-1}$ kg m^{-2} can be linked to the increase of ε_{hc}. Beyond this I, high clouds are opaque to LW radiation with $\varepsilon_{hc} \approx 1$ and the continued increase of C_{LW} is caused by the decrease of T_{hc}.

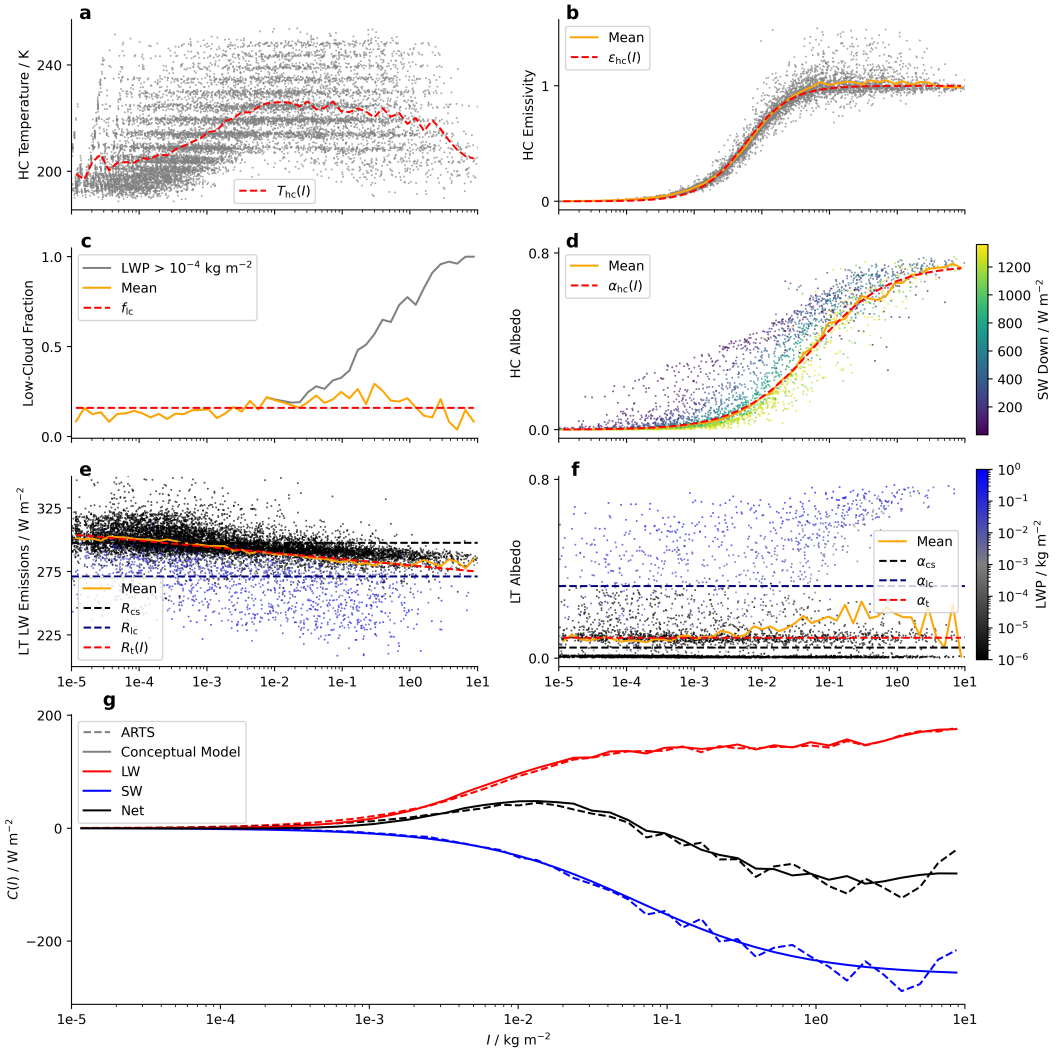


Figure A16: All input variables of the conceptual model (a-f) and the resulting high-cloud radiative effect C as a function of the ice water path I (g). Dots in a-f show individual atmospheric profiles, solid orange lines the mean binned by I and red dashed lines denote model inputs of high cloud (HC) and lower troposphere (LT) variables.

The reduction of complexity involved in $C(I)$ we achieve by using I as the predictor of C comes at the cost of neglecting other factors that influence C. A major simplification we make is to not consider the effect of ice particle properties, such as their effective radii and number concentration, which might affect $C(I)$ if they change, e.g. due to aerosols (Beer et al., 2024). Furthermore, we do not take into account that the effect of ice condensate on radiation per ice water content may be different for different hydrometeors, with larger particles having a weaker extinction per ice water content (e.g. Feng et al., 2025). This is confirmed by our ARTS simulation, for which cloud ice causes around 88% of C, even though it only makes up for 10% of the total atmospheric ice mass within the tropics. Therefore, it can be a good alternative to our approach of using the vertical integral of the sum of all ice hydrometeors (cloud ice, snow, and graupel) as a predictor of C to only rely on cloud

ice. However, using the vertical integral of cloud ice as a predictor for C would mean to miss the approximately 12% of C caused by snow and graupel and prevent the comparison of models to satellite observations, which typically provide I and hence include all ice species (discussed in more detail in Sec. A9.1).

A6 LOW CLOUDS RENDER THE HIGH-CLOUD RADIATIVE EFFECT POSITIVE

The high-cloud radiative effect depends not only on the radiative properties of high clouds, but also on the assumption of what would be there instead of the clouds, if they were missing. Therefore, low clouds have the potential to alter C. The impact of low clouds on C becomes visible by comparing $C(I)$ from ARTS for cases with low clouds (LWP $> 10^{-4}$ kg m^{-2}) and without low clouds (LWP $< 10^{-4}$ kg m^{-2}) (Fig. A17). Low clouds reduce the magnitude of the SW part of $C(I)$ more strongly than the LW part, which results in C becoming more positive for all I. This is a result of how low clouds change the boundary conditions of C. They are much brighter but only slightly colder than the clear-sky surface, and therefore decrease the contrast between high clouds and the lower troposphere more strongly in the SW than in the LW spectrum.

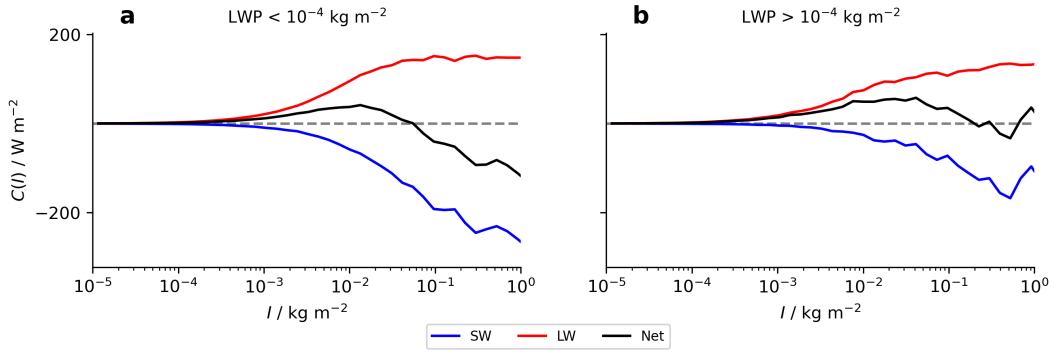


Figure A17: High-cloud radiative effect (C) from ARTS as a function of ice water path (I) without low clouds being present below the high clouds (a) and with low clouds (b).

Via this mechanism, the amount of low clouds can change the mean high-cloud radiative effect. We show this by calculating $\overline{C}$ with our conceptual model for various values of f_{lc}. Increasing amounts of low clouds render $\overline{C_{\mathrm{net}}}$ more positive (Fig. A18). A doubling of $f_{\mathrm{lc}} = 0.16$ diagnosed from this ICON simulation leads to an increase of $\overline{C_{\mathrm{net}}}$ by 102%. The linear relationship between f_{lc} and C is a result of f_{lc} altering the lower tropospheric radiative properties linearly within the conceptual model (Fig. A15).

This effect of cloud overlap is difficult to analyse with conventional satellite and model products, which only provide clear-sky and all-sky fluxes. The cloud radiative effect (CRE) calculated from these fluxes includes high and low clouds and can hence not be interpreted as a measure of C. The negative radiative effect of warm and bright low clouds is included in the CRE and will offset the SW contribution from high clouds to more negative values. This becomes visible in the CRE calculated from

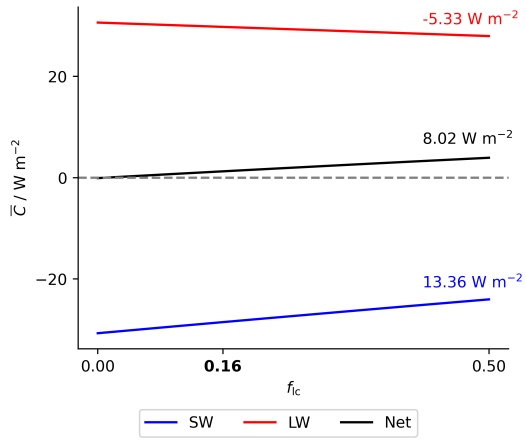


Figure A18: Mean high-cloud radiative effect $\overline{C}$ for different low cloud fractions f_{lc} from the conceptual model. The value of f_{lc} diagnosed from the ICON simulation is indicated in bold. The numbers next to the lines denote the slope of the curves.

satellite observations for the tropical west pacific by Gasparini et al. (2019), which remains negative even for the smallest I. Their result should hence not be interpreted, as the CRE of high clouds, but as the CRE of a region that contains a lot of high clouds, together with some low clouds. We hypothesize that the estimate of $\overline{C_{net}}$ from McKim et al. (2024) is 2.75 W m^{-2} more negative than our estimate because they do not properly account for the effect of overlapping low clouds. Since their detection of clouds relies on reflectivities observed from space, low clouds below optically thick high clouds will be obscured, which leads to an underestimation of the cloud overlap effect. Sokol et al. (2024) developed a different approach to calculate C from all-sky and clear-sky fluxes. They calculate an "ice-only" CRE which only includes profiles with frozen clouds, and an "all-sky" CRE which includes frozen and liquid clouds. For their estimate of C, they use the "ice-only" CRE at $I < 10^{-1}$ kg m^{-1} and the "all-sky" CRE at $I > 10^{0}$ kg m^{-1} with a linear transition in-between. While this approach yields a $C_{net}(I)$ with a shape similar to our estimate, it does not include the effect of overlapping low clouds on C, which increases $C_{net}(I)$ as we have shown above. We assume that this explains the difference between their estimate of the maximum $C_{net}(I)$ of 34 Wm^{-2} and our estimate of 45 Wm^{-2}.

A7 TOWARDS A BETTER UNDERSTANDING OF TROPICAL HIGH-CLOUD FEEDBACKS

The conceptual model can be used as a tool to diagnose $\overline{C}$ and the related feedback from GSRMs or other km-scale data sources. The main improvement compared to earlier approaches of diagnosing the tropical high-cloud feedback is that our conceptual model is able to predict the individual contributions of clouds over the whole I spectrum and how they contribute to the mean high-cloud radiative effect (Fig. A19). This enables us to show that $C(I)$ and $P(I)$ are equally important for $\overline{C}$ and how SW and LW contributions cancel out. The ability of the conceptual model to diagnose the contribution of thin high clouds with $\varepsilon_{hc} < 1$ to $\overline{C}$ improves on the com-

monly used radiative kernels, which are known to wrongly interpret such clouds as part of a deeper and optically thicker cloud, since their detection algorithm of cloud top height relies on brightness temperature (Zelinka et al., 2012b). The approach of Sokol et al. (2024) to diagnose $C(I)$ went into a similar direction as our conceptual model. However, we go one step further by explaining what shapes the relationship between C and I, which enables us to diagnose differences in $C(I)$ between models or climates.

By reducing the complexity of $C(I)$, the conceptual model simplifies diagnosing high-cloud feedbacks. If we assume that $\alpha_{\mathrm{hc}}(I)$ and $\varepsilon_{\mathrm{hc}}(I)$ are invariant to surface warming, since the physics of how radiation interacts with cloud condensate do not depend on the climate, the input data we need to diagnose $C(I)$ can be reduced to $T_{\mathrm{hc}}(I)$ and f_{lc}. This means that no additional radiative transfer simulations are necessary. To calculate $T_{\mathrm{hc}}(I)$ and f_{lc} in a way that is consistent with our conceptual model, instantaneous profiles of cloud hydrometeors are needed (Sec. A9.4).

Resolving C as a function of I allows us to investigate how proposed mechanisms of the tropical high-cloud feedback like PHAT (Zelinka and Hartmann, 2010) and the stability iris (Bony et al., 2016) play out across the ice water path spectrum. While PHAT is expected to change $C(I)$, the stability iris effect would affect $P(I)$. Both mechanisms may well apply differently to high clouds of different I, since the processes governing cloud formation and lifetime vary greatly with I, ranging from deep convective clouds to thin cirrus. E.g. results from RCE indicate that the stability iris might apply only to thick high clouds with negative $C_{\mathrm{net}}(I)$ (Sokol et al., 2024).

It is possible to apply our conceptual model to GCMs with horizontal grid spacings of $\mathcal{O}(100\ \mathrm{km})$, but we believe this is less promising than focusing on high-resolution GSRMs. The I that can be derived from GCMs often does not include precipitating hydrometeors and does not compare well with satellite observations (Eliasson et al., 2011). Furthermore, we expect high I associated with deep convection or thick anvils to be less well represented in GCMs compared to GSRMs due to the low horizontal resolution of GCMs. On the other hand, $P(I)$ from GSRMs compares well with satellite observations (Turbeville et al., 2022). As multi-year GSRM simulations become more common (Wieners et al., 2024), we believe that future research on tropical high-cloud feedbacks should focus on GSRM simulations and try to constrain them with satellite observations. Especially satellite products based on active radar and lidar measurements seem promising, as they are able to resolve cloud overlaps (e.g. Matus and L'Ecuyer, 2017).

A8 SUMMARY AND CONCLUSION

With this study, we seek to improve the understanding of the high-cloud radiative effect within the tropics by explaining its dependence on the ice water path. This perspective reveals that the radiative effect of a cloud with a specific ice water path and its frequency of occurrence are equally important for its contribution to the mean high-cloud radiative effect. By showing how radiative properties of high clouds depend on the ice water path, we provide a more physical framework for the analysis of high-cloud radiative effect compared to earlier studies assuming high clouds to be uniform (McKim et al., 2024).

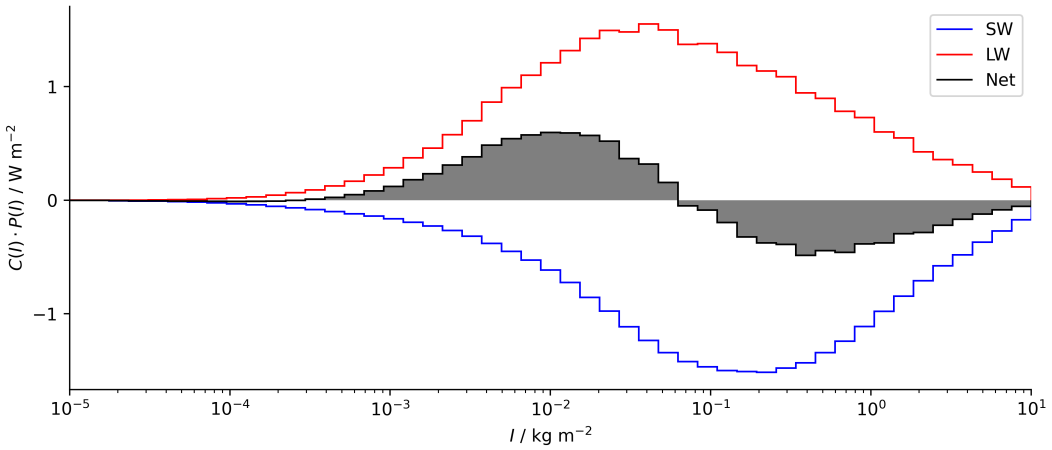


Figure A19: The high-cloud radiative effect ($C(I)$) from the conceptual model, weighted by the ice water path distribution ($P(I)$) from ICON. The area below the curves is proportional to the mean high-cloud radiative effect ($\overline{C}$).

For the development of the ice water path perspective on high clouds, we harness the capability of GSRMs to resolve individual clouds in global simulations. We use the atmospheric profiles from ICON with 5 km horizontal grid spacing and calculate radiative fluxes offline with ARTS, which allows us to switch the effect of high clouds off in the radiative transfer calculations. By developing a conceptual model, we demonstrate that the complexity of the high-cloud radiative effect can be reduced significantly if it is interpreted as a function of ice water path. To first order, the dependency of the high-cloud radiative effect on ice water path can be explained by abstracting high clouds as a single layer whose temperature, emissivity and albedo are varying with ice water path. Within this framework, the lower troposphere below high clouds is characterised by upwelling LW emissions and an albedo. We conceptualise these properties as functions of the low cloud fraction, which determines the contributions from clear-sky and low-cloud regions, with an additional correction term being introduced for the upwelling LW emissions.

The dependence of high-cloud albedo and emissivity on the logarithm of the ice water path is characterised by an S-shape that can be well approximated with logistic functions. While the dependence of the SW high-cloud radiative effect on ice water path is governed only by the high-cloud albedo, the interplay of high-cloud emissivity and temperature explains their LW radiative effect. Up to an ice water path of 10^{-1} kg m^{-2} the LW high-cloud radiative effect increases as a result of increasing high-cloud emissivity. The continued increase of the LW high-cloud radiative effect beyond this ice water path where the high-cloud emissivity reaches one is explained by the decrease of high-cloud temperature. The net high-cloud radiative effect results from a cancellation of SW and LW effects. For thin high clouds below an ice water path of $6 \cdot 10^{-2}$ kg m^{-2} the LW component dominates, hence the net high-cloud radiative effect is positive and converges towards zero for decreasing ice water path. Above an ice water path of $6 \cdot 10^{-2}$ kg m^{-2}, the SW component dominates and the net high-cloud radiative effect becomes negative.

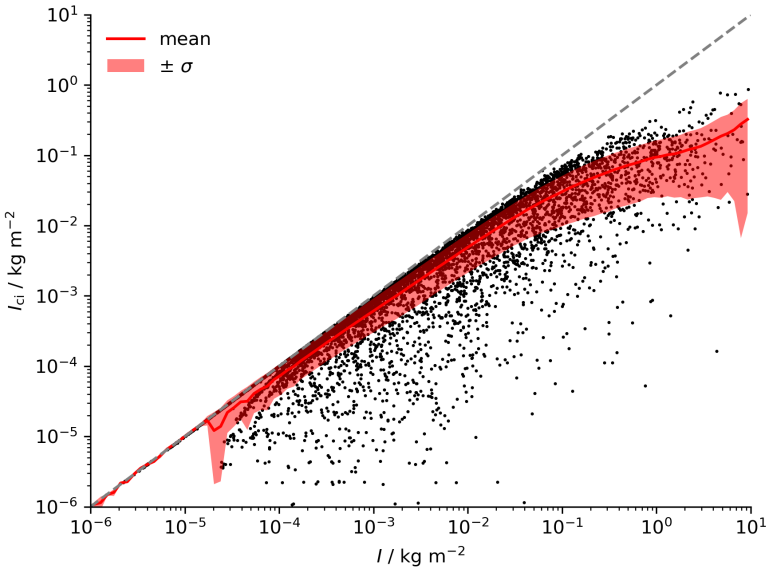


Figure A20: Cloud ice water path I_{ci} plotted against ice water path I for 10,000 randomly chosen profiles (black dots) and the mean I_{ci} binned by I together with ± one standard deviation (red line and red shading).

We show that the mean radiative effect of high clouds becomes more positive for increasing amounts of underlying low clouds. This can be understood as a result of low clouds being bright but relatively warm. Therefore, they decrease the contrast of high clouds and the lower troposphere more strongly in the SW than in the LW spectrum, resulting in a stronger decrease in magnitude of the negative SW high-cloud radiative effect compared to its positive LW counterpart. With this cloud overlap effect included, we derive a mean high-cloud radiative effect from the ARTS simulations of 1.25 W m^{-2}, which is closely matched by the conceptual model with 1.26 W m^{-2}. while our estimate of the mean high-cloud radiative effect is reasonably close to the 2 Wm^{-2} estimated by L'Ecuyer et al. (2019), it is significantly higher than the -1.5 Wm^{-2} from McKim et al. (2024). We assume that this discrepancy is a result of underestimation of the cloud overlap effect by McKim et al. (2024), since low clouds are obscured by thick high clouds in satellite observations.

Great hopes have been put in the abilities of GSRMs in helping to reduce the uncertainty of cloud feedbacks. The conceptual model based on the ice water path perspective introduced in this study provides a framework for analysing the tropical high-cloud feedback produced by GSRMs, since it reduces the involved complexity significantly.

A9 METHODS

A9.1 *Choosing the Right Predictor for the High-Cloud Radiative Effect*

Ice in the atmosphere is typically divided into a number of hydrometeor species within models. The ICON simulation we use distinguishes cloud ice, snow and graupel

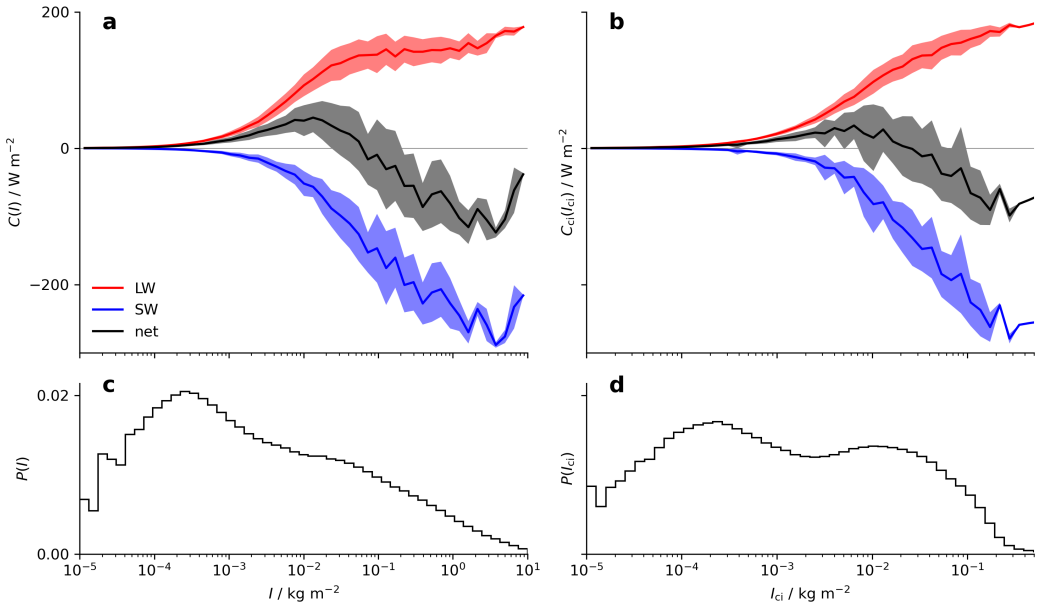


Figure A21: High cloud radiative effect $C \pm$ one standard deviation plotted against ice water path I (a) High cloud radiative effect only including cloud ice C_{ci} plotted against cloud ice water path I_{ci} (b). Probability distribution P of ice water path and cloud ice water path (c and d).

(Baldauf et al., 2011). Even though cloud ice only makes up for 10% of the total atmospheric ice mass in the tropics, it is the most important hydrometeor for C. If we deactivate snow and graupel in ARTS, C is reduced by only 13% in the SW and 12% in the LW regime. Since the SW and the LW contribution cancel out and the reduction in the SW dominates, C_{net} is increased by 15%.

That cloud ice has a much stronger effect on radiation per unit mass compared to snow and graupel means that I, the vertical integral of all three hydrometeors, might not be a reliable predictor for C. This discrepancy arises because C depends not only on the total amount of ice present in the atmosphere, as measured by I, but also on whether this ice predominantly comprises radiatively active cloud ice or the less radiatively active snow or graupel. However, this issue is mitigated if I serves as a good proxy for the vertical integral of cloud ice (I_{ci}), meaning that the fraction of cloud ice contained in I remains consistent for all I. For the ICON simulation we use, there is a such a clear relationship between I and I_{ci} (Fig. A20). The standard deviation of the mean I_{ci} binned by I is around 50% of the mean value for most I, and increases to 100% for high I. Any noise within the relation of I and I_{ci} will result in noise of $C(I)$, as it means the fraction of cloud ice contained in I might vary.

We test how big the increase in noise in $C(I)$ is due to the imperfect relation of I and I_{ci} by comparing the standard deviation of $C(I)$ to the one of the high cloud radiative effect caused by cloud ice (C_{ci}) as a function of I_{ci}. The standard deviation of $C_{\text{ci}}(I_{\text{ci}})$ is indeed generally smaller than that of $C(I)$, but not significantly (Fig. A21 a and b). The average standard deviation of $C_{\text{ci}}(I_{ci})$ in the LW is 6.4 W m^{-2} compared to 10.2 W m^{-2} for $C(I)$ and 12.7 W m^{-2} compared to 16.2 W m^{-2} respectively in the SW.

The general shape of $C_{ci}(I_{ci})$ is comparable to $C(I)$ (Fig. A21 a and b). However, the maximum of I_{ci} is about 1.5 orders of magnitude smaller than the maximum of I, resulting in a more compressed probability distribution (Fig A21 c and d). It is possible to use I_{ci} within our conceptual model to predict C_{ci}, and doing so does not change our results significantly (not shown). This means that both I and I_{ci} can be used to predict the high-cloud radiative effect.

Whether it is the better choice to include all ice species in the analysis of the high-cloud radiative effect, or not, depends on the question at hand. We believe that for a comparison of several GSRMs, it would be better to exclude less radiatively active ice species and investigate the different $C_{ci}(I_{ci})$, since the partitioning between the ice species may vary strongly between models. However, if a study relies on a single model, or includes satellite observations, we think it is better to use $C(I)$. In this case, we believe that the advantages of this approach of being able to include the radiative effect of all ice species in the high-cloud radiative effect and facilitating the comparison to satellite observations, which typically provide I, outweigh the disadvantage of increasing the noise in the $C(I)$ relationship. Since this study relies only on one model, and we plan to include satellite observations in future studies, we choose to include all ice species in our analysis.

A9.2 *Connectedness of Clouds*

Our definition of high clouds assumes that liquid cloud condensate (q_l) is part of the high cloud if it is connected in the vertical to the frozen condensate (q_f). We assess whether q_l and q_f within one atmospheric column are connected by inspecting the gap between the respective vertical maxima. To this end, we calculate the height at which the maximum concentration of liquid and frozen condensate occurs for every column:

$$z_l = z|_{q_l=\max(q_l)},$$
$$z_f = z|_{q_f=\max(q_f)},$$

where z is the vertical model coordinate. If we can find a grid cell between those levels where the liquid and the frozen condensate are both less than 10% of their respective maximum value within the column, the two phases are considered unconnected:

$$c = \begin{cases} 0, & \exists\ z \in [z_l, z_f] : (q_l < 0.1 \cdot \max(q_l)) \wedge (q_f < 0.1 \cdot \max(q_f)), \\ 1, & \text{Else}, \end{cases} \tag{13}$$

with c being connectedness. Liquid condensate that is not connected to the frozen condensate is interpreted as a low cloud, independent of the high cloud above. Liquid condensate becomes increasingly connected to high clouds for high I (Fig. A22). Changing the percentage of the maximum value required for connectedness affects C derived from ARTS. For a threshold of 5% we derive a C_{total} of 1.01 Wm^{-2} and 1.53 Wm^{-2} for 15%. However, this does not affect our qualitative finding that SW and LW contributions to C_{total} cancel out, resulting in a weakly positive net value.

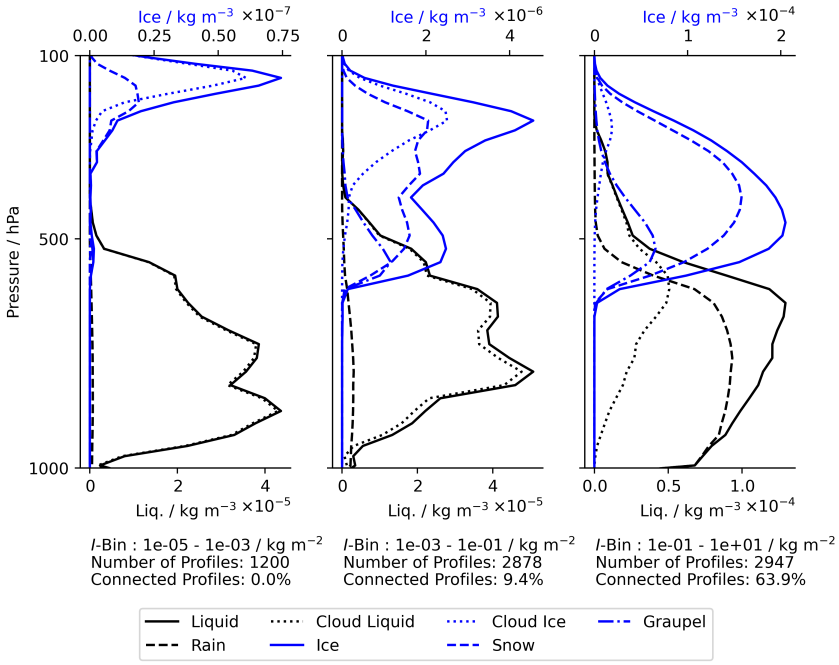


Figure A22: Mean hydrometeor profiles averaged over the respective ice water path I bin for profiles that contain frozen and liquid clouds. The I-bin, the number of profiles within it, and the percentage of those profiles that contain connected liquid and frozen clouds are indicated below each subplot.

A9.3 *Conceptualising Albedo*

The SW radiation $(1-\alpha_{hc})S$ that penetrates the high cloud is partly reflected by the lower troposphere with an albedo α_t, hence $\alpha_t(1-\alpha_{hc})S$ is reflected by the lower troposphere towards the high cloud. Depending on the high-cloud albedo α_{hc}, a fraction of this upward reflected radiation will penetrate the high cloud, while the rest is reflected back to the lower troposphere and is subject to the same sequence of reflections again. The amount of SW radiation that is reflected by high clouds and the lower troposphere to space (F_{up}) is described by the following series

$$F_{up} = \alpha_{hc}S + \alpha_t(1-\alpha_{hc})^2 S + \alpha_{hc}\alpha_t^2(1-\alpha_{hc})^2 S + \alpha_{hc}^2\alpha_t^3(1-\alpha_{hc})^2 S + \ldots$$

This can be rewritten as

$$F_{up} = S\left[\alpha_{hc} + \alpha_t(1-\alpha_{hc})^2\left(1 + \alpha_{hc}\alpha_t + \alpha_{hc}^2\alpha_t^2 + \ldots\right)\right]. \tag{14}$$

For $\alpha_{hc} < 1$ and $\alpha_t < 1$ the geometric series from this equation converges

$$\sum_{n=0}^{\infty}(\alpha_{hc}\alpha_t)^n = \frac{1}{1-\alpha_{hc}\alpha_t}.$$

Therefore, we can rewrite Eq. 14 as

$$F_{up} = S\left(\alpha_{hc} + \frac{\alpha_t(1-\alpha_{hc})^2}{1-\alpha_{hc}\alpha_t}\right).$$

A9.4 *Parameterizing the Conceptual Model*

The parameters of our conceptual model and their dependence on the IWP are inferred from the ARTS simulations. By default, we use all atmospheric profiles from ARTS within the tropics (30°S to 30°N) for the parameterization, except for the 14% of the sample that contain ice clouds with cloud tops below 350 hPa. Only for high-cloud albedo and emissivity, we restrict the parameterization to atmospheric profiles that do not contain low clouds, since this reduces the noise significantly.

A9.4.1 *Cloud Top Temperature*

To diagnose T_{hc} from the ARTS simulations, we identify the cloud top pressure (p_{top}). For thin clouds, we want T_{hc} to correspond to the level from which most LW are emerging. Hence, we calculate the cloud top pressure of thin clouds p_{thin} as the level with the maximum ice water content (IWC, sum of all frozen hydrometeors)

$$p_{\mathrm{thin}} = p|_{IWC=\max(IWC)}.$$

However, for thick clouds with $\varepsilon_{\mathrm{hc}} = 1$, the LW emissions might emerge from a higher level if enough IWC is located above p_{thin}. To find this emission level of thick clouds, we rely on the considerations of Jeevanjee (2023) and define the vertically integrated ice mass (I, integral downwards from the top) above the emission level as

$$I_{\mathrm{em}} = I|_{T_{\mathrm{a}}=T_{\mathrm{b}}},$$

where T_{b} is the brightness temperature calculated from the spectrally integrated outgoing LW flux at TOA and T_{a} is the atmospheric temperature. Averaged over all high clouds with IWP $> 10^{-1}$ kg m^{-2} for which we assume $\varepsilon_{\mathrm{hc}} = 1$, this yields $I_{\mathrm{em}} = 6.7 \cdot 10^{-3}$ kg m^2. We use this value to calculate the cloud top pressure of thick clouds (p_{thick}) as

$$p_{\mathrm{thick}} = p|_{I=I_{\mathrm{em}}}.$$

For a consistent definition of p_{top} over all IWP, we define it as

$$p_{\mathrm{top}} = \min(p_{\mathrm{thick}}, p_{\mathrm{thin}}).$$

T_{hc} is then defined as

$$T_{\mathrm{hc}} = T_{\mathrm{a}}|_{p=p_{\mathrm{top}}},$$

where T_{a} is the atmospheric temperature. For the conceptual model, we use the mean value of T_{hc} binned by I.

A9.4.2 *Emissivity*

To calculate $\varepsilon_{\mathrm{hc}}$, we require the LW flux at TOA from our conceptual model to match the one from ARTS

$$(1 - \varepsilon_{\mathrm{hc}})R_{\mathrm{t}} + \varepsilon_{\mathrm{hc}}\sigma T^4 = F_{\mathrm{LW,allsky}}.$$

Since we only include atmospheric profiles without low clouds in this parameterisation, R_t simplifies to the clear-sky flux at TOA ($F_{LW,clearsky}$). Substituting R_t with $F_{LW,clearsky}$ and rearranging for ε_{hc} yields

$$\varepsilon_{hc} = \frac{F_{LW,allsky} - F_{LW,clearsky}}{\sigma T^4 - F_{LW,clearsky}}$$

The mean ε_{hc} binned by I exhibits a logistic shape in the $\log_{10}(I)$ space (Fig. A16b). Since we expect this relationship to be invariant to surface warming, we decrease the complexity of the conceptual model by approximating $\varepsilon_{hc}(I)$ as a logistic function of $\log_{10}(I)$

$$\varepsilon_{hc}(I) = \frac{L''}{1 + \exp\left(-k''(\log_{10}(I) - x'')\right)}.$$

The parameters within this equation are inferred by fitting it to the binned mean ε_{hc} inferred from the ARTS simulations using non-linear least squares while requiring $L_\varepsilon = 1$, which limits ε_{hc} to a maximum value of 1.

A9.4.3 *Albedo*

To calculate α_{hc}, we require the SW flux at TOA from our conceptual model to match the one from ARTS

$$S - S\left(\alpha_{hc} + \frac{\alpha_t(1-\alpha_{hc})^2}{1-\alpha_{hc}\alpha_t}\right) = S - F_{SW,allsky}, \tag{15}$$

where $F_{SW,allsky}$ is the upward SW flux at TOA. Since we only include atmospheric profiles without low clouds, α_t simplifies to the clear-sky albedo (α_{cs}, compare Fig. A15). Dividing Eq.15 by S yields

$$\alpha_{hc} + \frac{\alpha_{cs}(1-\alpha_{hc})^2}{1-\alpha_{hc}\alpha_{cs}} = \frac{F_{SW,allsky}}{S}.$$

The right hand side term represents the all-sky albedo $\frac{F_{SW,allsky}}{S} = \alpha_{as}$. With this, we can rearrange for α_{hc}

$$\alpha_{hc} = \frac{\alpha_{as} - \alpha_{cs}}{1 + \alpha_{cs}(\alpha_{as} - 2)}.$$

To calculate the mean of α_{hc} binned by I we have to consider that α_{hc} depends on the amount of incoming SW radiation (Fig. A16d) and that α_{hc} at noon is more important for the daily mean than α_{hc} in the evening when incoming SW radiation is low. Therefore, we bin α_{hc} by I and longitude and interpolate this 2D field linearly to fill potential data gaps. Next, we calculate the mean over all longitudes for each I bin, weighted with the incoming SW radiation. Like ε_{hc}, the mean of α_{hc} binned by I exhibits a logistic shape (Fig. A16d). Since we assume that this relationship will also be invariant to surface warming, we decrease the complexity of the conceptual model by approximating $\alpha_{hc}(I)$ as a logistic function of $\log_{10}(I)$

$$\alpha_{hc}(I) = \frac{L_{ff}}{1 + \exp\left(-k_{ff}(\log_{10}(I) - x_{ff})\right)},$$

The parameters within this equation are determined by fitting it to the binned mean α_{hc} inferred from the ARTS simulations using non-linear least squares.

A9.4.4 *Lower Troposphere*

The radiative properties of the lower troposphere are parameterised based on the mean fraction of low clouds f_{lc}. To calculate f_{lc}, we compare the LWP to a threshold and require the low cloud not to be connected to a high cloud

$$f_{\mathrm{lc}} = \begin{cases} 1, \ \forall \ \mathrm{LWP} > 10^{-4} \ \mathrm{kg\ m^{-2}} \wedge c = 0, \\ 0, \ \text{otherwise.} \end{cases}$$

Here, c denotes connectedness as defined in Eq.13. Since the mean of f_{lc} binned by I does not vary significantly with I, we approximate f_{lc} to be constant for all I (Fig. A16c).

We calculate α_{cs} and α_{lc} by dividing the upward TOA fluxes $F_{\mathrm{SW,clearky}}$ and $F_{\mathrm{SW,lowcld}}$ by S respectively. For α_{t}, we select from α_{cs} and α_{lc} based on f_{lc}

$$\alpha_{\mathrm{t}} = \begin{cases} \alpha_{\mathrm{cs}}, \ \forall \ f_{\mathrm{lc}} = 0, \\ \alpha_{\mathrm{lc}}, \ \forall \ f_{\mathrm{lc}} = 1. \end{cases}$$

The mean value of α_{cs} is calculated by averaging α_{cs} over all atmospheric profiles with $f_{\mathrm{lc}} = 0$. To calculate the average of α_{lc}, we have to take into consideration that, like α_{hc}, it depends on the incoming SW radiation. To calculate the daily mean value of α_{lc}, we therefore apply the same technique as for α_{hc} and bin α_{lc} by LWP and longitude. We linearly interpolate this 2D field and average over all longitudes. From the resulting α_{lc} binned by LWP, we calculate the mean value as

$$\alpha_{\mathrm{lc}} = \frac{\sum_{\mathrm{LWP}} \alpha_{\mathrm{lc}}(\mathrm{LWP}) \cdot n(\mathrm{LWP})}{\sum_{\mathrm{LWP}} n(\mathrm{LWP})},$$

where $n(\mathrm{LWP})$ is the number of profiles with $f_{\mathrm{lc}} = 1$ per LWP bin.

To derive R_{t}, we use the TOA fluxes $F_{\mathrm{LW,clearsky}}$ and $F_{\mathrm{LW,lowcld}}$

$$R_{\mathrm{t}} = \begin{cases} F_{\mathrm{LW,clearsky}}, \ \forall \ f_{\mathrm{lc}} = 0, \\ F_{\mathrm{LW,lowcld}}, \ \forall \ f_{\mathrm{lc}} = 1. \end{cases}$$

For the mean value of R_{cs}, we average $F_{LW,clearsky}$ over all atmospheric profiles with $f_{\mathrm{lc}} = 0$. For the mean value of R_{lc}, we average $F_{LW,lowcld}$ over all atmospheric profiles with $f_{\mathrm{lc}} = 1$. The approximately linear decrease of the binned mean of R_{t} with $\log_{10}(I)$ (Fig. A16e) can be linked to an increase of integrated column water vapour with I (not shown). To correct for this, we introduce the correction term $C_{\mathrm{H_2O}}(I)$, which scales linearly with $\log_{10}(I)$

$$C_{\mathrm{H_2O}}(I) = a \cdot \log_{10}(I) + b.$$

The coefficients a and b are inferred from linearly regressing the anomaly of the binned mean of R_{t} with $\log_{10}(I)$.

Variable	Description	Constant Value
I	Ice water path	
T_{hc}	High-cloud temperature	
α_{hc}	High-cloud albedo	
ε_{hc}	High-cloud emissivity	
R_t	LW emissions from lower troposphere	
C_{H_2O}	Moisture correction term	
f_{lc}	Low-cloud fraction	0.16
α_t	Lower troposphere albedo	0.09
S	Incoming SW radiation	395 W m^{-2}
L_{ff}	Maximum high-cloud albedo	0.74
L''	Maximum high-cloud emissivity	1
k_{ff}	Steepness high-cloud albedo	1.8
k''	Steepness high-cloud emissivity	3
x_{ff}	Midpoint high-cloud albedo	-1.2
x''	Midpoint high-cloud emissivity	-2.2
R_{lc}	LW emissions from low clouds	271 W m^{-2}
R_{cs}	LW emissions from clear-sky	297 W m^{-2}
α_{lc}	Low-cloud albedo	0.32
α_{cs}	Clear-sky albedo	0.05
a	Slope of C_{H_2O}	4.9 W m^{-2}
b	Intercept of C_{H_2O}	13.5 W m^{-2}

Table A3: All variables used by the conceptual model with variable description and value if it is constant.

OPEN RESEARCH SECTION

The code to reproduce the results and figures presented in this study is available from `https://github.com/JakobDeutloff/cm_publication` and archived under `https://doi.org/10.5281/zenodo.14059493` (Deutloff, 2024). The model data and the parameter sets are archived under `https://doi.org/10.25592/uhhfdm.14753` (Deutloff and Brath, 2024). The full ICON simulation which provides the basis for our analysis is made available by Kluft (2023).

ACKNOWLEDGMENTS

This research was funded by the Deutsche Forschungsgemeinschaft (DFG, German Research Foundation) under Germany's Excellence Strategy EXC 2037 "CLICCS - Climate, Climatic Change, and Society" - Project Number: 390683824, contribution to the Center for Earth System Research and Sustainability (CEN) of Universität

Hamburg. We thank Brett McKim, Adam Sokol and Blaž Gasparini for inspiring discussions and Lukas Kluft for assisting with the model data. We also want to thank the three anonymous reviewers who helped to improve this manuscript.

B

FACETS OF THE TROPICAL HIGH-CLOUD FEEDBACK IN A GLOBAL STORM-RESOLVING MODEL

This paper is under review and available as a preprint:
J. Deutloff, S. A. Buehler, J. Windmiller, and A. K. Naumann (2026a). "Facets of the Tropical High-Cloud Feedback in a Global Storm-Resolving Model." Preprint, under revision at npj Climate and Atmospheric Science. DOI: 10.21203/rs.3.rs-9133974/v1

Author Contributions: I conceptualised the study. S. A. Buehler, J. Windmiller and A. K. Naumann supervised the study and supported the conceptualisation. I conducted the analysis and wrote the manuscript with input from all co-authors.

Facets of the Tropical High-Cloud Feedback in a Global Storm-Resolving Model

Jakob Deutloff[1,2,3], Stefan A. Buehler[1,2], Julia Windmiller[4,5], Ann Kristin Naumann[6]

[1]Earth System Sciences, Atmospheric Science, University of Hamburg, Hamburg, Germany
[2]Earth and Society Research Hub (ESRAH), Hamburg, Germany
[3]International Max Planck Research School on Earth System Modelling (IMPRS-ESM), Hamburg, Germany
[4]Max Planck Institute for Meteorology, Hamburg, Germany
[5]Monash University, Melbourne, Australia
[6]Ludwig-Maximilians-Universität in Munich, Munich, Germany

ABSTRACT

Tropical high clouds are the cloud type that contributes most to the uncertainty in climate sensitivity, as their feedback on global warming remains poorly constrained. One reason for this is that global circulation models (GCMs) do not resolve the full spectrum of high clouds, ranging from thin cirrus to thick deep convective clouds. We use a set of storm-resolving aquaplanet simulations that resolve this spectrum to investigate how high clouds with different thicknesses contribute to the total high-cloud feedback. We find that the total feedback is positive, arising from all high clouds remaining at fixed temperatures and from an intensification of the diurnal cycle of deep convection. Fixed high-cloud temperatures require an interactive representation of ozone. Prescribing ozone, as often done in GCMs, results in an unrealistic warming of high clouds and hence a less positive feedback. Thick clouds produced by deep convection partly shift from daytime to nighttime in response to surface warming. This reduces sunlight reflection and results in a previously unrecognised positive feedback. The reduction of high clouds in response to warming, assumed to produce a negative feedback, affects thin (warming) and thick (cooling) clouds equally in our simulations, resulting in a near-neutral feedback. By resolving cloud thickness, our storm-resolving simulations show that heterogeneous high-cloud responses to warming combine to yield a positive total feedback.

B1 INTRODUCTION

High clouds fed by deep convection occur throughout the tropics, but remain difficult to predict due to their multiscale nature, spanning from the microscale of individual droplets, through the mesoscale of convective systems, to the synoptic scale of the intertropical convergence zone (Gasparini et al., 2023). As a result, tropical high clouds are the cloud type contributing most to the uncertainty in climate sensitivity, with their feedback on global warming being poorly constrained (Sherwood et al., 2020).

Progress in reducing the uncertainty in the response of tropical high clouds to surface warming has been difficult, partly because global circulation models (GCMs) have limited ability to capture the details of tropical convection. With a typical horizontal grid-spacing of $\mathcal{O}(100\ \mathrm{km})$, those models do not resolve convection or individual clouds and hence rely on parameterisations for those processes, which cause vast inter-model differences in the cloud response to warming (Stevens and Bony, 2013; Sanderson et al., 2008).

There is hope that the shortcomings of GCMs for simulating clouds can be overcome by global storm-resolving models (GSRMs) with a horizontal grid-spacing of $\mathcal{O}(1\ \mathrm{km})$ (Schär et al., 2020). Those models do not depend on parameterisations of convection since it is simulated explicitly, and clouds are resolved in the sense that microphysical models directly respond to grid-scale forcing (Satoh et al., 2019). GSRMs indeed represent some aspects of the tropical climate more accurately than GCMs: the diurnal cycle and the spatial distribution of precipitation are better captured (Stevens et al., 2020), and the inter-model spread of relative humidity is reduced (Lang et al., 2021).

Another benefit from GSRMs is that their high resolution allows for better interpretability of the results. By resolving high clouds, GSRMs capture the continuum of high clouds that exists in the real world, ranging from thick deep convective towers to thin cirrus (Turbeville et al., 2022). Therefore, the total high-cloud radiative effect can be decomposed into the high-cloud radiative effect as a function of cloud thickness, measured by ice water path (I), and the frequency of each I (Deutloff et al., 2025a; Sokol et al., 2024). This perspective uncovers how clouds with different thicknesses, governed by different physics, contribute to the high-cloud feedback.

We use the I-perspective to investigate the tropical high-cloud feedback in a set of global storm-resolving aquaplanet simulations. We will show that the tropical high-cloud feedback consists of three parts: a positive longwave feedback from high clouds remaining at fixed temperature, a positive shortwave feedback from an intensification of the diurnal cycle of convection and a near-neutral feedback from changes in high-cloud frequency. The total tropical high-cloud feedback we derive is positive, in contrast to the near-neutral estimate reported by the World Climate Research Programme (WCRP) expert assessment (Sherwood et al., 2020). This difference arises because the newly identified positive feedback from an intensified diurnal cycle of convection adds to the well-documented (Hartmann and Larson, 2002; Zelinka and Hartmann, 2010; Ceppi et al., 2017) feedback associated with approximately fixed high-cloud temperatures. In addition, the negative feedback expected by the WCRP assessment from a reduction of tropical high clouds proves to be near-neutral, as both

thin (warming) and thick (cooling) clouds decrease with warming. This near-neutral high-cloud amount feedback is in line with recent radiative convective equilibrium (RCE) simulations (Sokol et al., 2024) and observational estimates (McKim et al., 2024; Raghuraman et al., 2024; Wilson Kemsley et al., 2025).

B2 RESOLVING HIGH CLOUDS AT KM-SCALE

We simulate convection explicitly at 5 km horizontal grid spacing with the Sapphire version of the ICOsahedral Nonhydrostatic (ICON) model (Hohenegger et al., 2023), with parameterised turbulence (Smagorinsky, 1963), cloud microphysics (Baldauf et al., 2011) and interactive ozone (Cariolle and Teyssèdre, 2007). To allow for short simulation periods while including the main characteristics of tropical convection, we use an aquaplanet setup (Peinado Bravo et al., 2026; Blackburn et al., 2013) with a prescribed zonally symmetric sea surface temperature (SST) pattern (Neale and Hoskins, 2000) and no seasonal cycle. We conduct a three-month-long control and two warming simulations with the same simulation period and uniform SST increases of 2 K and 4 K (see Methods for details). Our analysis is constrained to the tropics (20°S to 20°N). By moving to the global scale, including rotation and the diurnal cycle of convection, we go beyond previous, more idealised cloud-resolving model studies (Sokol et al., 2024; Stauffer and Wing, 2023). Despite their reduced complexity, aquaplanet simulations reproduce key features of the Earth's atmosphere, and have proven useful for studying cloud feedbacks (Medeiros et al., 2015).

We define high clouds as all clouds that contain frozen condensate. To avoid artificial separation between the frozen and the liquid phase of clouds, we consider liquid condensate to be part of the high cloud if liquid and frozen condensate sufficiently overlap (Deutloff et al., 2025a) (Sec. B8).

The I frequency distribution, $P(I)$, within the tropics from ICON broadly agrees with satellite retrievals. The ICON simulations agree with both 2C-ICE R05 (Deng et al., 2010) and DARDAR v2.1.1 (Delanoë and Hogan, 2010) that high clouds become more frequent the thinner they are (Fig. B23b). However, deep convective clouds with $I > 1\ \mathrm{kg\ m^{-2}}$ are underrepresented in ICON, which is consistent with earlier studies (Turbeville et al., 2022). Differences between ICON and the satellite retrievals for $I < 10^{-1}\ \mathrm{kg\ m^{-2}}$ are significant, but should not be overinterpreted as the two retrievals also do not agree in this domain.

The high-cloud radiative effect, $C(I)$, calculated from the ICON simulations exhibits the characteristic shape (Sokol et al., 2024; Gasparini et al., 2022) of a positive net $C(I)$ for small I and a negative net $C(I)$ for high I with the sign change occurring at $I \approx 2 \cdot 10^{-1}\ \mathrm{kg\ m^{-2}}$ (Fig. B23a). The shape of the net $C(I)$ is a result of the cancellation of the positive longwave (LW) and negative shortwave (SW) contributions. With increasing I, the opacity of high clouds for LW radiation increases faster than their albedo, giving rise to the positive net $C(I)$, which switches to negative as the albedo keeps increasing with I (Deutloff et al., 2025a). The surprising increase of the SW $C(I)$ beyond $I > 7\ \mathrm{kg\ m^{-2}}$ does not result from the high-cloud albedo, but from the diurnal cycle of convection. Such deep convective clouds predominantly occur in the early morning, which decreases their SW $C(I)$ since the incoming SW radiation is less than for thinner clouds, which occur closer to noon (Fig. B.S1).

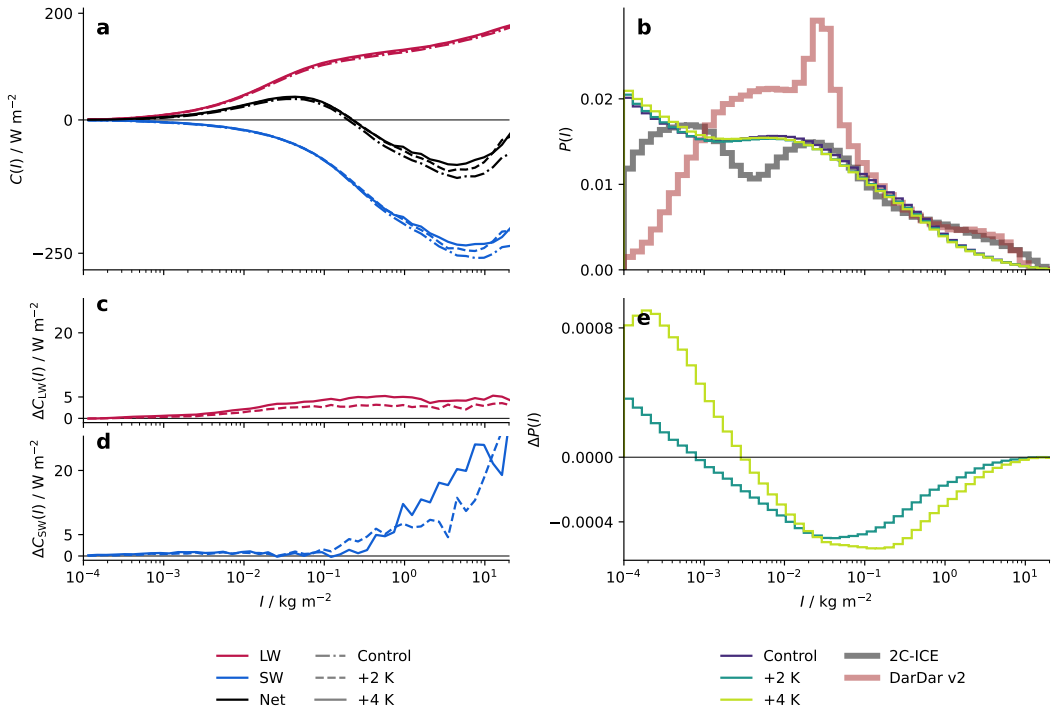


Figure B23: (**a**) High-cloud radiative effect (C) as a function of ice water path (I), (**b**) ice water path frequency distribution (P),(**c**) change of the LW C with respect to the control simulation (ΔC_{LW}),(**d**) change of the SW C with respect to the control simulation (ΔC_{SW}), (**e**) change in P with respect to the control simulation (ΔP).

As expected, the total high-cloud radiative effect ($\overline{C}$) is near-neutral. We calculate $\overline{C}$ as

$$\overline{C} = \sum_I C(I) \cdot P(I). \tag{16}$$

For the control simulation, we get $\overline{C} = 3.7$ W m^{-2}, which is slightly more positive than earlier estimates (McKim et al., 2024; L'Ecuyer et al., 2019), due to realistic treatment of overlapping low clouds (Deutloff et al., 2025a) (see Methods). The unrealistically low amount of deep convective clouds in ICON is another cause for a more positive $\overline{C}$. Nevertheless, the magnitude of $\overline{C}$ is still much lower than most $C(I)$, confirming the near-neutrality of $\overline{C}$ from a cancellation of cooling and warming high clouds.

B3 POSITIVE HIGH-CLOUD FEEDBACK

One advantage of our I-framework is that we can analyse whether the feedback is due to changes in $C(I)$ or $P(I)$. The total tropical high-cloud feedback (F) is calculated as the change in $\overline{C}$ per unit warming:

$$F = \frac{\Delta \overline{C}}{\Delta T_{\mathrm{s}}} \approx \sum_I \underbrace{P(I)\frac{\Delta C(I)}{\Delta T_{\mathrm{s}}}}_{F_{\mathrm{C}}(I)} + \sum_I \underbrace{\frac{\Delta P(I)}{\Delta T_{\mathrm{s}}} C(I)}_{F_{\mathrm{P}}(I)}, \tag{17}$$

with T_s being the mean surface temperature, and Δ the difference with respect to the control simulation (see Methods). This linearised chain rule separates the feedback contributions from changes in $P(I)$ (F_P) and changes in $C(I)$ (F_C).

Our framework differs from other studies that use radiative kernels to isolate cloud feedbacks (Zelinka et al., 2016; Raghuraman et al., 2024). Using changes in C per unit warming as a measure of cloud feedbacks has been shown to underestimate their magnitude relative to the true cloud feedback, defined as the radiative change caused by cloud properties in isolation (Soden et al., 2004). The reason behind this is that changes in C include clear sky effects such as the change in water vapour. However, this does not impact our conclusions, since the magnitude of our feedback values is generally higher than previous estimates, and this discrepancy is explained by the high-cloud response to surface warming (Sec. B4 and B6).

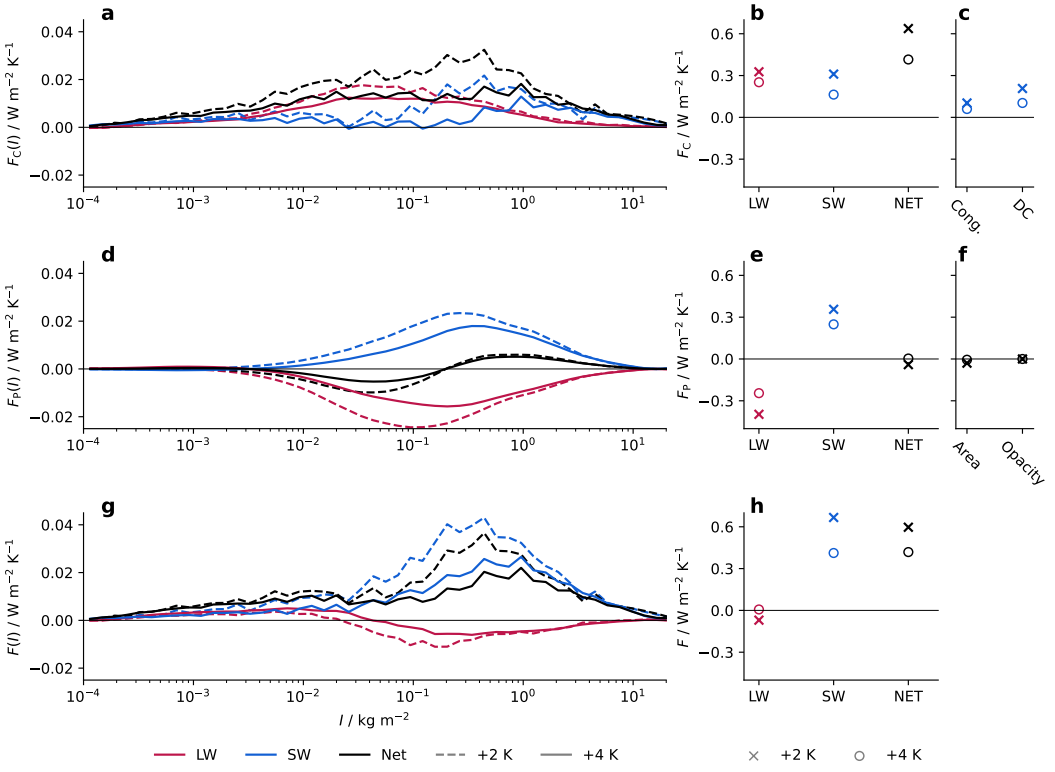


Figure B24: (**a**) Feedback from changes in the high-cloud radiative effect (F_C) as a function of ice water path (I) and (**b**) its sum. (**c**) The SW F_C partitioned into the feedback from changes in the amount of congestus clouds and changes in the diurnal cycle (DC) of deep convective clouds. (**d**) Feedback from changes in ice water path frequency (F_P) as a function of I, (**e**) its sum and (**f**) the net F_P partitioned into the feedback from changes in high-cloud area and opacity. (**g**) Total high-cloud feedback (F) as a function of I and (**h**) its sum. All feedback values are tropical means.

The LW $C(I)$ becomes more positive and the SW $C(I)$ becomes less negative with surface warming (Fig. B23c, d), producing positive feedbacks of similar magnitude (Fig. B24a, b). While the LW $\Delta C(I)$ is positive at all I, the SW $\Delta C(I)$ is significantly larger than 0 primarily at $I > 1$ kg m^{-2}, where it reaches about five times the magnitude of its LW counterpart. That the LW and SW contributions to F_C are still

of similar magnitude is a result of high values of the SW $\Delta C(I)$ occurring only at less frequent high I, whereas the LW $\Delta C(I)$ is also significantly positive at more frequent low I. We find that the LW $\Delta C(I)$ results from high-cloud temperatures remaining approximately fixed with surface warming (Sec. B4). The SW $\Delta C(I)$ results from a decrease of congestus clouds with surface warming at $I \leq 10^{-1}$ kg m^{-2} (Fig. B.S2) and from changes in the diurnal cycle of deep convective clouds at $I > 10^{-1}$ kg m^{-2} (Sec. B6).

We partition the SW F_C into contributions from the congestus feedback and the diurnal cycle feedback by summing up $F_C(I)$ over the respective I ranges. This reveals that the diurnal cycle feedback is more than twice as strong as the congestus feedback (Fig. B24c). The positive congestus feedback arises from high clouds in a warmer world being less likely to contain high amounts of liquid condensate at $I \leq 10^{-1}$ kg m^{-2}, which decreases their average albedo. This feedback is a result of our method for defining high clouds, which includes liquid condensate as part of the high cloud if frozen and liquid condensate sufficiently overlaps (see Methods). If liquid clouds are ignored, the congestus feedback vanishes (Fig. B.S3). Therefore, we regard the congestus feedback as an artefact of our method for defining high clouds and focus on the diurnal cycle feedback in the following (Sec. B6).

The frequency of high clouds changes with surface warming (Fig. B23e), but the resulting F_P is near-neutral (Fig. B24c, d). The reason for the near-neutral feedback is that the reduction of cooling clouds is cancelled by the reduction of warming clouds, while the increase of the lowest I is not radiatively relevant. Possible explanations for the change in high-cloud frequency are changes in atmospheric stability or cloud radiative heating (Sec. B5).

For comparison with previous literature (Raghuraman et al., 2024; McKim et al., 2024; Wilson Kemsley et al., 2025; Sherwood et al., 2020), we partition the net F_P into the more commonly discussed area and the opacity feedbacks (Sokol et al., 2024). The area feedback is calculated as the overall change in high-cloud fraction times $\overline{C}$. Since $\overline{C}$ is near-neutral, large changes in high-cloud fraction would be required to produce a significant area feedback (McKim et al., 2024). However, the overall change in high-cloud fraction remains below 1 % K^{-1} for both warming simulations; hence, the area feedback is near zero. The opacity feedback arises since the change in high-cloud fraction is non-uniform across I, i.e. it describes the feedback from a shift in the balance between cooling and warming high clouds. The opacity feedback is near neutral for the same reason as the net F_P: the reduction of cooling clouds is cancelled by the reduction of warming clouds. Changes in the microphysics of high clouds in response to surface warming can add to the opacity feedback if they affect the opacity of high clouds. This is not the case in our simulations (Fig. B.S4).

The total tropical high-cloud feedback we derive is positive with 0.6 W m^{-2} K^{-1} (+2 K) and 0.42 W m^{-2} K^{-1} (+4 K). This is a result of both LW $C(I)$ and SW $C(I)$ becoming more positive with surface warming. Within the next sections, we explain and discuss the different feedback components.

B4 FIXED HIGH-CLOUD TEMPERATURES

The positive LW F_C results from tropical high-cloud temperatures (T_{hc}) remaining approximately fixed despite surface warming. The binned $T_{hc}(I)$ reveals that deep convective clouds ($I > 1$ kg m^{-2}) are cold, anvils (1 kg m^{-2} $\geq I >$ 10^{-2} kg m^{-2}) are about 30 K warmer and thin cirrus ($I \leq 10^{-2}$ kg m^{-2}) are almost as cold as the deep convective clouds (Fig. B25a). This shape of $T_{hc}(I)$ remains remarkably fixed despite surface warming. The change in $T_{hc}(I)$ with respect to the control simulation is below 1 K for all I (Fig B25b). Averaged over all I, the change in T_{hc} per degree of surface warming is -0.17 K K^{-1} (+2 K) and -0.06 K K^{-1} (+4 K).

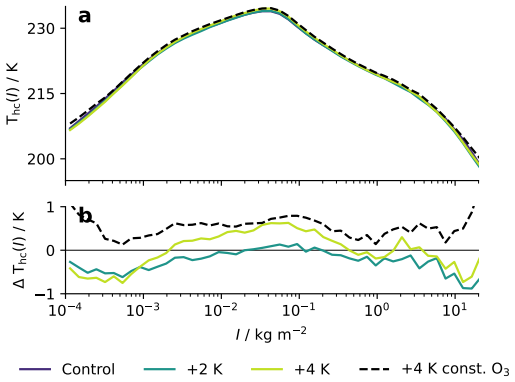


Figure B25: (**a**) High-cloud temperature (T_{hc}) as a function of ice water path (I) and (**b**) change in high-cloud temperature with respect to the control simulation (ΔT_{hc}).

Our finding of approximately fixed high-cloud temperatures agrees well with the fixed anvil temperature (FAT) theory (Hartmann and Larson, 2002), but disagrees with most GCMs, which predict high clouds to warm at about 0.33 K K^{-1} as surface temperatures increase, which gave rise to the proportionately higher anvil temperature (PHAT) theory (Zelinka and Hartmann, 2010; Ceppi et al., 2017). Within those GCM simulations, ozone is usually prescribed to remain constant on pressure levels despite surface warming (Taylor et al., 2012; Eyring et al., 2016). It has been argued that such treatment of ozone might cause an unrealistic warming of tropical high clouds (Seidel and Yang, 2022). We test this hypothesis with an additional +4 K warming simulation for which we prescribe the ozone profile from the control simulation to remain constant on pressure levels (see Methods). We find that in this case, high-cloud temperatures do indeed slightly increase with surface warming at 0.09 K K^{-1} (Fig. B25). If ozone is prescribed, the ozone profile cannot rise to higher altitudes together with the temperature profile as the surface warms, resulting in higher ozone concentrations in the upper troposphere and tropopause region and hence higher temperatures (Fig. B.S5). This finding emphasises the importance of interactive ozone schemes and casts doubt on the PHAT theory.

Our estimates of the LW F_C of 0.33 W m^{-2} K^{-1} (+2 K) and 0.25 W m^{-2} K^{-1} (+4 K) lie at the upper bound of previous estimates of the high-cloud altitude feedback. The global mean feedback value from the WCRP assessment can be directly compared to our tropical mean values, since GCMs suggest that the high-cloud altitude feedback is of similar magnitude in the tropics and the rest of the

world (Ceppi et al., 2017; Sherwood et al., 2020). The WCRP feedback estimate of 0.2 ± 0.1 W m^{-2} K^{-1} is based on their ensemble of GCM simulations, but they also derive a feedback estimate of 0.35 ± 0.2 W m^{-2} K^{-1} from an observational study (Vaillant de Guélis et al., 2018). Our results are closer to that observational estimate than to the one from GCMs. This is a consequence of fixed high-cloud temperatures in our simulations, rather than the slight warming simulated by most GCMs, which may be due to unrealistic ozone treatment.

B5 STABILITY IRIS AND RADIATIVE HEATING

While we do find the expected (Bony et al., 2016; Jeevanjee, 2022; Saint-Lu et al., 2020) decrease of anvil clouds (1 kg m$^{-2} \geq I > 10^{-2}$ kg m^{-2}) in response to surface warming, the feedback resulting from changes in high-cloud frequency is near-neutral. The area feedback is near-neutral, since the total area change and the mean high-cloud radiative effect are small, which agrees with observational estimates (McKim et al., 2024; Raghuraman et al., 2024; Wilson Kemsley et al., 2025), but contradicts the negative WCRP feedback estimate. The opacity feedback, not discussed by the WCRP, is also near-neutral in our simulations, since clouds with negative and positive $C(I)$ reduce equally in frequency (Fig. B24c).

Doubts about a negative feedback from a reduction of anvil clouds are supported by recent cloud-resolving RCE simulations, which also yield a near-neutral area feedback, but a positive opacity feedback of 0.07 W m^{-2} K^{-1} (Sokol et al., 2024). The shape of $\Delta P(I)$ from the RCE simulations resembles our result, but the decrease in frequency mostly affects thicker clouds with a negative $C(I)$ in the RCE simulations, which explains their positive opacity feedback.

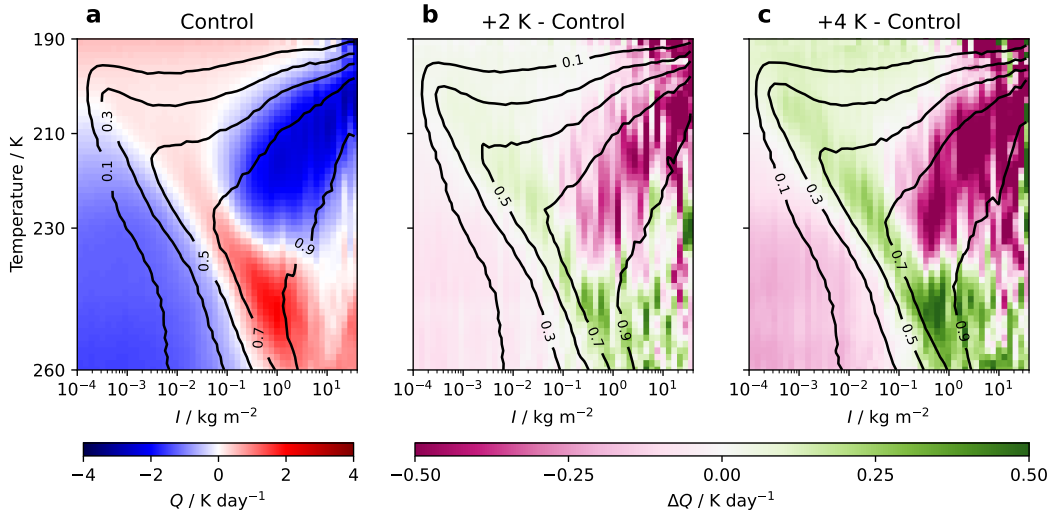


Figure B26: (**a**) Radiative heating rate (Q) binned by temperature and ice water path (I) for the control run, (**b, c**) change in radiative heating rate (ΔQ) with respect to the control simulation. The contour lines depict cloud fraction.

Judging from the shape of $\Delta P(I)$ (Fig. B23e), there seem to be two counteracting mechanisms at work in our simulations that drive the change of high-cloud frequency

in response to surface warming: one that increases thin cirrus and one that decreases anvil clouds.

The stability iris (Bony et al., 2016; Jeevanjee, 2022; Saint-Lu et al., 2022; Saint-Lu et al., 2020) is a mechanism associated with a reduction of anvil clouds in response to warming. The physical thinking behind the stability iris is that the horizontal divergence detraining anvil clouds from deep convection is constrained by radiatively driven convergence in clear-sky regions via mass balance. As atmospheric stability increases, clear-sky convergence and hence anvil clouds are expected to decrease. We find that a stability iris exists in our simulations as clear-sky convergence decreases with surface warming at $0.006\ \mathrm{day}^{-1}\mathrm{K}^{-1}$ (Fig. B.S7). However, this decrease is smaller than the $0.013\ \mathrm{day}^{-1}\mathrm{K}^{-1}$ found in cloud-resolving RCE simulations (Jeevanjee, 2022) or the $0.016\ \mathrm{day}^{-1}\mathrm{K}^{-1}$ from GCM RCE simulations (Bony et al., 2016). A possible reason for this disagreement is that we are using all-sky radiative fluxes in cloud-free regions to calculate radiative subsidence (see Methods), while the above-mentioned studies use clear-sky radiative fluxes over the entire domain, which we did not save.

We hypothesise that an increase in cloud radiative heating (Fig. B26) might prolong cirrus lifetimes, which would explain their increased frequency at higher surface temperatures. Our simulations confirm basic physical considerations (Gasparini et al., 2024) that the magnitude of cloud radiative heating increases with surface warming (Fig. B26). As the surface warms, clouds rise isothermally to lower pressure and hence lower density, which increases the magnitude of heating rates (Fig. B.S8). Cirrus lifetimes are prolonged by radiative heating that causes the cloud to rise and hence keeps it in a supersaturated environment (Hartmann et al., 2018). As cloud radiative heating increases with surface warming, cirrus are lifted to colder temperatures (Fig. B25b), which should increase their lifetime.

B6 INTENSIFICATION OF THE DIURNAL CYCLE OF DEEP CONVECTION

A major advancement of GSRMs is that they can simulate a realistic diurnal cycle of deep convection, something GCMs struggle with (Song et al., 2024; Stevens et al., 2020). We use the Chalmers Cloud Ice Climatology (CCIC) (Amell et al., 2024; Pfreundschuh et al., 2025) to compare the diurnal cycle of deep convection from our aquaplanet simulations to the diurnal cycle over oceans. We define deep convective clouds as grid cells with $I > 1\ \mathrm{kg\ m}^{-2}$ in agreement with earlier studies (Bolot et al., 2023). The aquaplanet simulations reproduce the two peaks of deep convective clouds, but the early morning peak is more pronounced than the afternoon peak compared to CCIC (Fig. B27). The afternoon peak is assumed to be intensified by diurnal SST variations (Ruppert and Johnson, 2016; Bellenger et al., 2010), which would explain why it is less pronounced in our aquaplanet simulations with fixed SST.

We find that the positive SW F_{C} at $I > 0.1\ \mathrm{kg\ m}^{-2}$ is due to a more pronounced diurnal cycle of deep convection. Deep convection during daytime reduces in response to surface warming, and so do the clouds produced by deep convection. This is most pronounced for deep convective clouds (Fig. B27), but also affects thick anvil clouds with $0.1\ \mathrm{kg\ m}^{-2} < I < 1\ \mathrm{kg\ m}^{-2}$ (Fig. B.S1). As clouds produced by deep convection

become less frequent during the day, they receive less solar radiation and hence reflect less, which explains their weaker SW $C(I)$.

The feedback associated with changes in the diurnal cycle of tropical deep convection has received limited attention, even though our results suggest that it substantially contributes to the positive tropical high-cloud feedback. The SW F_C resulting from changes in the diurnal cycle of deep convection is 0.2 W m^{-2} K^{-1} (+2 K) and 0.1 W m^{-2} K^{-1} (+4 K). Further studies are necessary to test whether the diurnal cycle feedback also exists over land. If it holds only over tropical oceans, which our simulations are representative of, the feedback must be scaled by the ocean fraction in the tropics (0.74), which yields 0.15 W m^{-2} K^{-1} (+2 K) and 0.074 W m^{-2} K^{-1} (+4 K) for the tropical feedback. The non-linearity of the diurnal cycle feedback is caused by thick anvils with 0.1 kg m^{-2} $< I <$ 1 kg m^{-2} (Fig. B24a). Those clouds reduce substantially during the day in the +2 K simulation, while their response is more muted in +4 K simulation (Fig. B.S1).

Our analysis suggests that the amplification of the diurnal cycle of deep convection results from intensified cloud radiative heating in response to surface warming. Cloud radiative heating has been shown to drive the diurnal cycle of deep convection over the ocean (Ruppert and Hohenegger, 2018; Mapes and Houze, 1993; Gray and Jacobson, 1977). The peak of deep convection in the early morning hours is caused by LW cooling of high clouds communicated to the surroundings via gravity waves, which leads to a destabilisation of the atmosphere, favouring deep convection. During the day, SW heating of high clouds stabilises the atmosphere and leads to a suppression of deep convection. With cloud radiative heating being a key driver of the diurnal cycle of deep convection, it seems reasonable to assume that the intensified cloud radiative heating (Fig. B26) causes the intensified diurnal cycle of deep convection.

It remains an open question how the presence of land might influence changes in the diurnal cycle of deep convection. Convection over land may respond differently to surface warming, since its diurnal cycle is strongly controlled by SW surface heating (Yang and Slingo, 2001). In addition, land–sea contrasts that drive local circulations may further modulate changes in the diurnal cycle of deep convection. Nevertheless, the increasing magnitude of cloud radiative heating is independent of the surface type (Gasparini et al., 2024), suggesting that the mechanism outlined above may be universal.

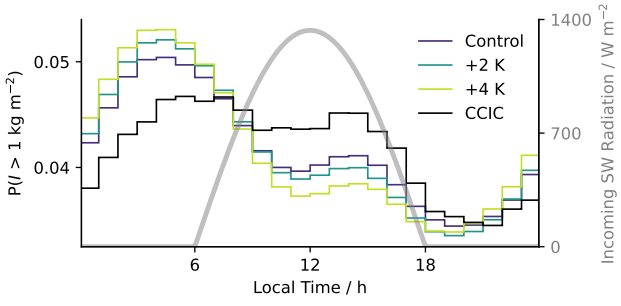


Figure B27: Frequency of occurrence (P) of deep convective clouds with ice water path (I) higher than 1 kg m^{-2} for every hour and incoming SW radiation.

B7 CONCLUSION

Resolving the spectrum of high clouds, ranging from thin cirrus to thick deep convective clouds, allows us to reassess the tropical high-cloud feedback. Our GSRM simulations reveal that the tropical high-cloud feedback consists of three parts, ranging from previously known to newly identified: A positive longwave feedback from fixed high-cloud temperatures, a near-neutral feedback from changes in high-cloud frequency, and a positive shortwave feedback from an intensified diurnal cycle of deep convection.

That high-cloud temperatures remain fixed despite surface warming agrees with theory (Hartmann and Larson, 2002), but disagrees with most GCMs, which predict a slight warming of high clouds (Zelinka and Hartmann, 2010; Ceppi et al., 2017). Therefore, the resulting feedback is more positive in our simulations than in GCMs. We find that this discrepancy is partly due to the unrealistic treatment of ozone within GCMs.

The anticipated reduction of tropical high clouds with surface warming, thought to be driven by an increase in atmospheric stability (Bony et al., 2016), affects thin (warming) and thick (cooling) clouds equally in our simulation. Therefore, we find the feedback from changes in high-cloud frequency to be near neutral, rather than negative, as suggested by the WCRP assessment. Such doubts about the WCRP estimate are supported by recent RCE simulations (Sokol et al., 2024) and observational estimates (McKim et al., 2024; Raghuraman et al., 2024; Wilson Kemsley et al., 2025).

The feedback from changes in the diurnal cycle of clouds has received limited attention, but our results suggest that it can be substantial. As the surface warms, thick and reflective clouds produced by deep convection occur less frequently during the day and more frequently during the night, and hence reflect less sunlight. We hypothesise that this change in the diurnal cycle of deep convection is driven by the increase in cloud radiative heating with surface warming, consistent with the strong coupling between cloud radiative heating and deep convection (Ruppert and Hohenegger, 2018). The broad agreement between the diurnal cycle of deep convection from our aquaplanet simulations and the observed diurnal cycle over oceans lends credibility to the plausibility of such a feedback. Nevertheless, targeted modelling studies are required to investigate the mechanism causing a reduction of daytime deep convection, and observational analyses will be essential to assess whether this feedback operates in the real climate system.

Overall, our results suggest that a positive tropical high-cloud feedback seems more plausible than the near-neutral feedback suggested by the WCRP assessment, which implies a higher climate sensitivity.

B8 METHODS

B8.1 *Aquaplanet Simulations*

We use version 2024.10 of ICON, which is open source and available from GitLab. We use a vertical grid with 90 levels, which are increasingly fine-spaced towards the

surface. The SST is prescribed to follow the zonally symmetric Qobs distribution (Neale and Hoskins, 2000), with maximum temperatures at the equator and minimum temperatures at the poles.

For the control simulation, we run six months of spin-up, which is sufficient for the model to reach a stationary state (not shown). To save computing time, we initialise the spin-up simulations of the +2 K, the +4 K and the +4 K with constant ozone simulations from the control spin-up. This allows us to shorten their spin-up simulations to three months.

We use three months of simulation of the control, the +2 K, the +4 K runs for our analysis. This is sufficiently long to reach a statistically stable state for $\Delta P(I)$, which we found to be the most fragile quantity in our analysis (Fig. B.S9). We only use one month of simulation for the +4 K run with constant ozone. Changes in high cloud temperature are more robust, and hence one month is sufficient to reach a statistically stable state.

All the data that we use is instantaneous. Full 3D atmospheric profiles are saved at 0 UTC every day, and 2D variables are saved hourly. Saving 3D profiles once a day is sufficient since the aquaplanet is uniform along latitudes.

B8.2 *Handling Big Data*

To reduce the amount of data required for our analysis, we draw random samples from the model output. We randomly sample 10^7 atmospheric profiles from within the tropics (20°S to 20°N) for every simulation, which proves sufficient to capture the statistics of the data (not shown). Those samples are used for calculating C and T_{hc}, which require 3D profiles. For the analysis of the stability iris and the heating rates, we interpolate a subsample of 10^6 3D profiles on temperature levels.

For the histograms within our analysis (Fig. B23b, e and Fig. B27), we use the entire 2D data to achieve maximum accuracy.

B8.3 *High-Cloud Radiative Effect*

For the calculation of C, we define high clouds as any cloud that contains frozen condensate. We consider liquid condensate to be part of the high cloud if frozen and liquid condensate sufficiently overlap within the column (Deutloff et al., 2025a; Haslehner et al., 2024). This avoids artificial separation of liquid and frozen clouds, which is most obvious for deep convection, where liquid and frozen condensate are always part of the same cloud and cannot exist without the other phase.

We calculate three radiative fluxes: The all-sky flux (F_{allsky}), which includes all condensate, the wet-sky flux (F_{wetsky}), which only sees liquid condensate, and the clear-sky flux (F_{clearsky}), which does not see any condensate.

We calculate C as the difference in the net radiative flux with and without the high cloud at the top of the atmosphere :

$$C = F_{\mathrm{allsky}} - F_{\mathrm{nohcld}},$$

where the flux without the high cloud (F_{nohcld}) either includes liquid condensate or not, depending on whether the liquid phase is part of the high cloud:

$$F_{\text{nohcld}} = \begin{cases} F_{\text{clearsky}}, & \text{if } c = 1, \\ F_{\text{wetsky}}, & \text{if } c = 0. \end{cases}$$

Here, c represents the connectedness of the liquid and frozen cloud condensate within the column, with a value of 1 indicating that the two are connected and 0 otherwise.

We determine whether liquid condensate (q_{l}) and frozen condensate (q_{f}) are connected, based on the gap between their respective maxima. To this end, we calculate the height (z) of the maximum frozen and liquid condensate for every column:

$$z_{\text{l}} = z|_{\max(q_{\text{l}})},$$
$$z_{\text{f}} = z|_{\max(q_{\text{f}})}.$$

If we can find a grid cell between z_{f} and z_{l} where both liquid and frozen condensate are less than 5% times a tuning factor of their maximum, we consider both phases to be unconnected:

$$c = \begin{cases} 0, & \exists\, z \in [z_{\text{l}}, z_{\text{f}}] : (q_{\text{l}} < 0.05 \cdot \left(\frac{z_{\text{k}}}{z_{\text{m}}}\right)^7 \cdot \max(q_{\text{l}})) \wedge (q_{\text{f}} < 0.05 \cdot \left(\frac{z_{\text{k}}}{z_{\text{m}}}\right)^7 \cdot \max(q_{\text{f}})), \\ 1, & \text{Else}, \end{cases}$$

where z_{k} is the average difference between z_{l} and z_{f} of the respective simulation and z_{m} is the average of z_{k} over all three simulations. The SW F_{C} is the only feedback component that is sensitive to the threshold chosen to decide whether frozen and liquid clouds are connected (Fig. B.S10). Since the sign of the SW F_{C} is robust, this does not affect our conclusions.

The tuning factor $\left(\frac{z_{\text{k}}}{z_{\text{m}}}\right)^7$ is necessary because clouds extend further up with warming. This means there will be a higher chance of finding a grid box with less than the fraction of condensate required for $c = 1$, which increases the fraction of unconnected liquid clouds with warming (Fig. B.S11). More liquid cloud below the high clouds would decrease the SW $C(I)$ and hence create a SW feedback (Deutloff et al., 2025a). We consider such a feedback to be artificial, since the mean liquid cloud fraction does not increase with warming (Fig. B.S11). To avoid such an artificial feedback, we keep the liquid cloud fraction constant at each I by using the tuning factor.

Introducing the F_{wetsky} as an additional diagnostic variable in ICON is necessary to properly distinguish high, frozen clouds from low, liquid clouds. This mainly becomes important for anvil and cirrus clouds, which are independent of the lower liquid clouds. If F_{wetsky} is not available, an alternative approach can be to disregarding gridcells with overlapping high and low clouds for low I (Sokol et al., 2024). However, this leads to an underestimation of $C(I)$ for those clouds (Deutloff et al., 2025a).

The I frequency distribution $P(I)$ used to calculate the total high-cloud radiative effect $\overline{C}$ (Eq. 16) should be interpreted as the I-resolved high-cloud fraction. That means $\overline{C}$ is the average high-cloud radiative effect across the tropics, including areas without high clouds.

B8.4 *Feedback Partitioning*

The complete equation for the partitioning of the total high-cloud feedback, F, also includes a non-linear term:

$$F = \frac{\Delta\overline{C}}{\Delta T_\mathrm{s}} = \sum_I \underbrace{\frac{\Delta P(I)}{\Delta T_\mathrm{s}} C(I)}_{F_\mathrm{P}(I)} + \sum_I \underbrace{P(I)\frac{\Delta C(I)}{\Delta T_\mathrm{s}}}_{F_\mathrm{C}(I)} + \sum_I \underbrace{\frac{\Delta P(I)}{\Delta T_\mathrm{s}}\frac{\Delta C(I)}{\Delta T_\mathrm{s}}}_{\mathrm{non-linear}}.$$

We neglect this non-linear term, since it is one order of magnitude smaller than both linear terms. Both $C(I)$ and $P(I)$ are taken from the control simulation.

B8.5 *High-Cloud Temperature*

We calculate T_hc as

$$T_\mathrm{hc} = \min\left(T|_{\max q_\mathrm{i}}, T_\mathrm{b}\right),$$

with $T|_{\max q_\mathrm{i}}$ being the temperature at maximum cloud ice (q_i) concentration, and T_b being brightness temperature. This formulation of T_hc has the advantage that it captures thin high-clouds which are semi-transparent to LW radiation and can hence be applied to clouds with any I (Deutloff et al., 2025a).

B8.6 *Stability Iris Analysis*

The physical thinking behind the stability iris is that the horizontal divergence ($\nabla_\mathrm{h}\mathbf{v}_\mathrm{cld}$), which detrains anvil clouds from deep convection, is constrained by horizontal convergence in clear-sky regions ($-\nabla_\mathrm{h}\mathbf{v}_\mathrm{clear}$) via mass balance (Bony et al., 2016). This convergence is a result of the clear-sky subsidence profile (ω_clear), which balances the radiative cooling (Q):

$$\nabla_\mathrm{h}\mathbf{v}_\mathrm{cld} = -\nabla_\mathrm{h}\mathbf{v}_\mathrm{clear} = \frac{\partial\omega_\mathrm{clear}}{\partial_z} \approx -\frac{\partial}{\partial_z}\frac{Q}{S}, \tag{18}$$

where S is static stability and z is height. We neglect latent heating in line with earlier studies (Bony et al., 2016; Saint-Lu et al., 2022).

We calculate Q as:

$$Q = \frac{1}{\rho c_\mathrm{p}}\frac{\mathrm{d}F}{\mathrm{d}z},$$

where ρ is air density, c_p specific heat capacity of air and F the radiative flux.

The static stability (S) is calculated as the difference between the dry lapse rate and the lapse rate:

$$S = \Gamma_\mathrm{d} - \Gamma = \frac{g}{c_\mathrm{p}} - \frac{\mathrm{d}T}{\mathrm{d}z},$$

where g is the gravitational constant.

Most previous studies analysing the stability iris use 3D clear-sky radiative fluxes (Bony et al., 2016; Jeevanjee, 2022), whereas we only store 3D all-sky radiative fluxes

due to disk storage constraints. Therefore, we define clear-sky profiles as profiles with $I < 10^{-2}$ kg m^{-2}, where $C(I)$ becomes sufficiently small (Fig. B23a). Our key findings do not rely on this threshold.

From the mean clear-sky profiles of Q and S, we calculate ω_{clear}:

$$\omega_{\text{clear}} = -\frac{Q}{S}.$$

The clear-sky convergence is then calculated as the vertical derivative of ω (Eq. 18). To reduce the noise in the clear-sky convergence profile, we use a third-order Savitzky-Golay filter to smooth ω before calculating the derivative.

ACKNOWLEDGEMENTS

The authors thank Blaž Gasparini, Seth Seidel, Sandrine Bony, Mark Zelinka, Martin Singh and James Ruppert for inspiring discussions and Lukas Kluft and Sebastian Rast for assisting with the ICON simulations.

FUNDING

This research was funded by the Deutsche Forschungsgemeinschaft (DFG, German Research Foundation) under Germany's Excellence Strategy—EXC 2037 "CLICCS-Climate, Climatic Change, and Society"—Project Number: 390683824, contribution to the Earth and Society Research Hub (ESRAH) of the University of Hamburg. This work used resources of the Deutsches Klimarechenzentrum (DKRZ) granted by its Scientific Steering Committee (WLA) under project ID bm1183.

CODE AVAILABILITY

The code to reproduce the figures and numbers from this paper is available from `https://doi.org/10.5281/zenodo.17472875` (Deutloff, 2026a).

DATA AVAILABILITY

The DARDAR data is available from `https://www.icare.univ-lille.fr/dardar/data-access/` and 2C-ICE data from http://cloudsat.cira.colostate.edu/data-products/2c-ice. The data to reproduce the figures and numbers from this paper is available from `https://doi.org/10.5281/zenodo.17472875` (Deutloff, 2026b).

AUTHOR CONTRIBUTION

All authors contributed to designing the research. J.D. carried out the research and wrote the paper with input from all co-authors.

COMPETING INTERESTS

All authors declare no financial or non-financial competing interests.

B.S1 SUPPLEMENT

B.S1.1 *Influence of Time of Occurrence on High-Cloud Radiative Effect*

The SW $C(I)$ becomes stronger for more incoming solar radiation, which can be modulated by the local time at which the respective cloud occurs, and its distance to the equator. To first order, the incoming SW radiation is governed by the timing of the clouds. This becomes evident by the solar radiation closely following the time difference to noon (Fig. B.S1).

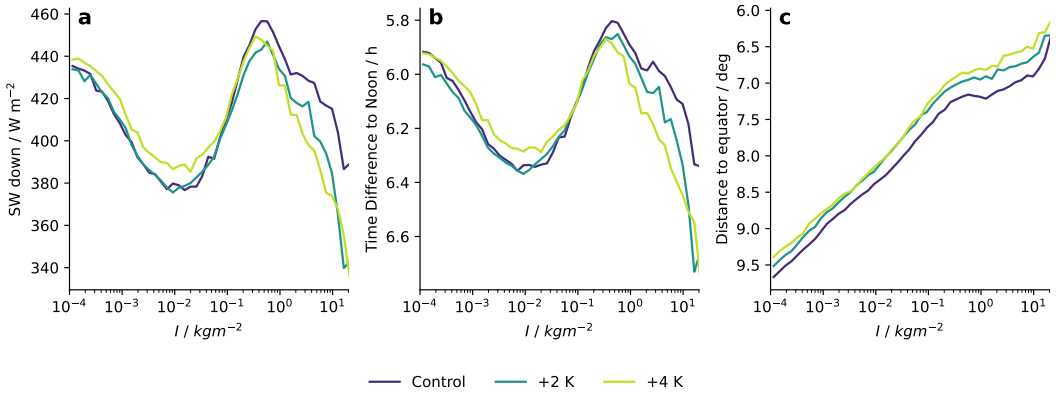


Figure B.S1: (**a**) Incoming SW radiation, (**b**) time difference to noon and (**c**) distance to the equator binned by ice water path (I).

B.S1.2 *Congestus Feedback*

Liquid clouds can either be part of a high cloud if the frozen and liquid condensate sufficiently overlap, or not (Eq. 3). At low I, overlap between frozen and liquid clouds is rare, but it exists. We refer to such overlapping clouds as congestus clouds, since they typically contain more liquid than frozen condensate. The rest of the liquid clouds are referred to as low clouds.

Liquid clouds reduce as surface temperature increases (Fig. B.S2a), which causes a reduction in both low clouds (Fig. B.S2b) and congestus clouds (Fig. B.S2c). Congestus clouds also carry less liquid as surface temperatures increase. The median liquid water path of congestus clouds at $I < 10^{-1}$ kg m^{-2} is 0.169 kg m^{-2} (control), 0.152 kg m^{-2} (+2 K) and 0.145 kg m^{-2} (+4 K).

The reduction of congestus clouds together with their reduced amount of liquid condensate causes the SW $C(I)$ to become less negative at $I < 10^{-1}$ kg m^{-2} in response to surface warming (Fig. 1d). This becomes apparent when we calculate $\Delta C_{\mathrm{SW}}(I)$ only for frozen clouds, i.e. liquid condensate is not included as part of the high clouds. In this case, the positive $\Delta C_{\mathrm{SW}}(I)$ at $I < 10^{-1}$ kg m^{-2} does not exist (Fig. B.S3).

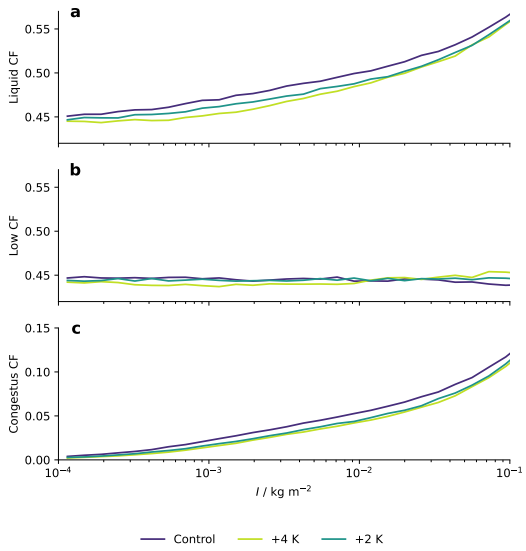


Figure B.S2: (**a**) Fraction of all liquid clouds, (**b**) fraction of low clouds (liquid clouds that are not part of the high clouds) and (**c**) fraction of congestus clouds (liquid clouds that are part of the high clouds).

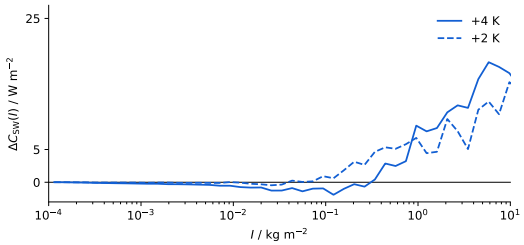


Figure B.S3: Change in the SW $C(I)$ for frozen clouds only.

B.S1.3 *Albedo and Emissivity of High Clouds*

We test whether changes in the microphysics of high clouds in response to surface warming alter the high-cloud opacity by calculating the high-cloud albedo and emissivity (Deutloff et al., 2025a). Both the albedo and the emissivity of high clouds remain remarkably constant despite surface warming (Fig. B.S4). We conclude from this that potential changes in the microphysics of high clouds in response to surface warming do not alter their opacity in our simulations.

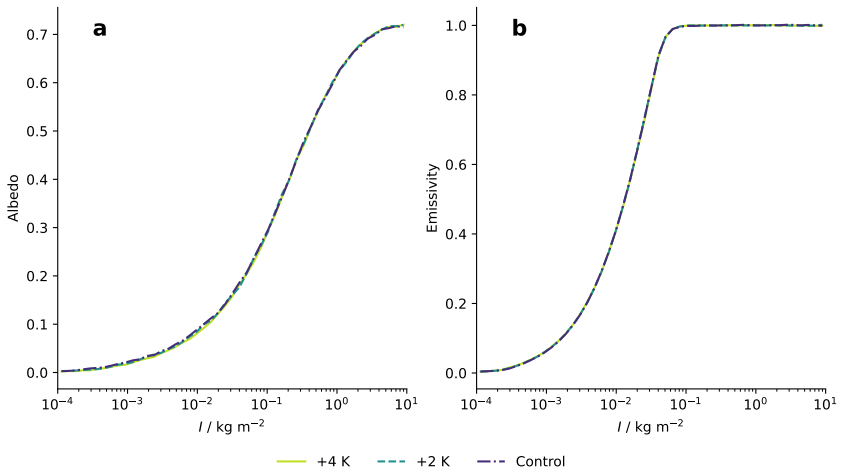


Figure B.S4: (**a**) Albedo of high clouds and (**b**) emissivity of high clouds.

B.S1.4 *Constant Ozone Simulation*

The temperature profile of the +4 K warming simulation with prescribed constant ozone simulation shows clear tropopause warming. This is not the case for warming simulations with interactive ozone, for which the temperature profile shifts upward.

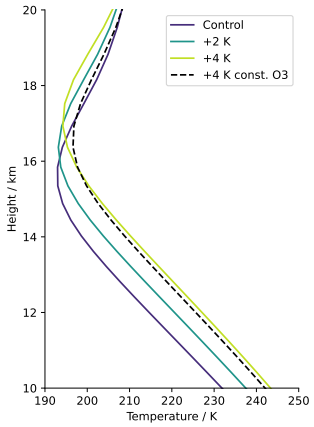


Figure B.S5: Mean clear-sky temperature profiles.

B.S1.5 *Stability Iris*

The static stability is increasing with surface warming as expected (Fig. B.S6b); however, this is partly cancelled by an increase in clear-sky radiative cooling (Fig. B.S6a). Therefore, changes in the subsidence profiles and the convergence are small (Fig. B.S6c, d). This cancellation was also found by previous studies, but seems more pronounced in our simulations (Bony et al., 2016).

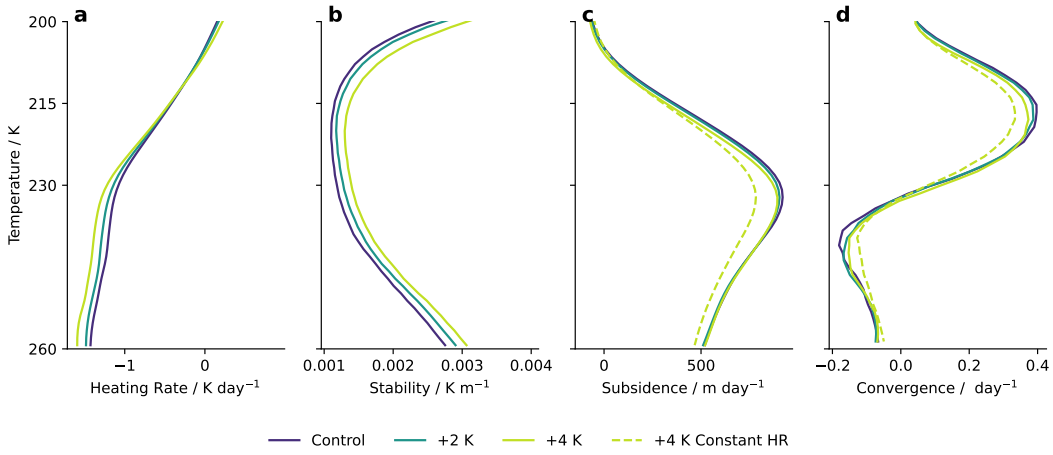


Figure B.S6: (**a**) Mean profiles within the clear-sky atmosphere of heating rate, (**b**) static stability, (**c**) radiatively driven subsidence and (**d**) horizontal convergence of radiatively driven subsidence. The dotted line in **c** and **d** shows results for the +4 K simulation with the heating rate fixed at the control profile.

Regressing the maximum clear-sky convergence ($D_{\max}$) against the surface temperature anomaly yields the decrease of $D_{\max}$ in response to increasing surface temperatures, which is central to the stability iris theory (Fig. B.S7).

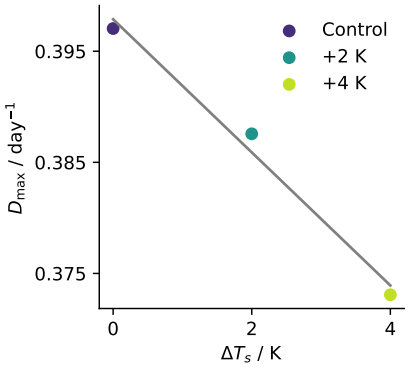


Figure B.S7: Maximum clear-sky convergence ($D_{\max}$) plotted against the surface temperature anomaly (ΔT_s) and linear regression of the data (grey line).

B.S1.6 *Heating Rates*

Radiative heating rates (Q) are calculated as

$$Q = \frac{1}{\rho c_\mathrm{p}} \frac{\mathrm{d}F}{\mathrm{d}z},$$

where ρ is air density, c_p specific heat capacity of air and F the radiative flux. As the surface warms, the atmosphere expands, and isotherms move to lower pressure and hence lower density. The high clouds follow the isotherms (Hartmann and Larson, 2002), and hence also move to lower density. The flux divergence $\frac{\mathrm{d}F}{\mathrm{d}z}$ is expected to stay constant at a given isotherm, despite the isothermal expansion of the atmosphere (Jeevanjee and Romps, 2018). The decrease in density at cloud height should therefore imply a higher magnitude of cloud radiative heating (Gasparini et al., 2024). However, changes in the diurnal cycle of clouds will affect the SW $\frac{\mathrm{d}F}{\mathrm{d}z}$. We test the relative importance of the density effect and the change in flux divergence for the overall change in heating rates by decomposing the change in heating rates:

$$\Delta Q = \underbrace{\Delta \frac{1}{\rho c_\mathrm{p}} \frac{\mathrm{d}F}{\mathrm{d}z}}_{\text{Density}} + \underbrace{\frac{1}{\rho c_\mathrm{p}} \Delta \frac{\mathrm{d}F}{\mathrm{d}z}}_{\text{Flux Divergence}} + \underbrace{\Delta \frac{1}{\rho c_\mathrm{p}} \Delta \frac{\mathrm{d}F}{\mathrm{d}z}}_{\text{non-linear}}.$$

This decomposition reveals that the decrease in density is the main driver for changes in heating rates (Fig. B.S8). Changes in the flux divergence exist and cause changes in radiative heating, but they are noisier and contribute less to the overall change in radiative heating.

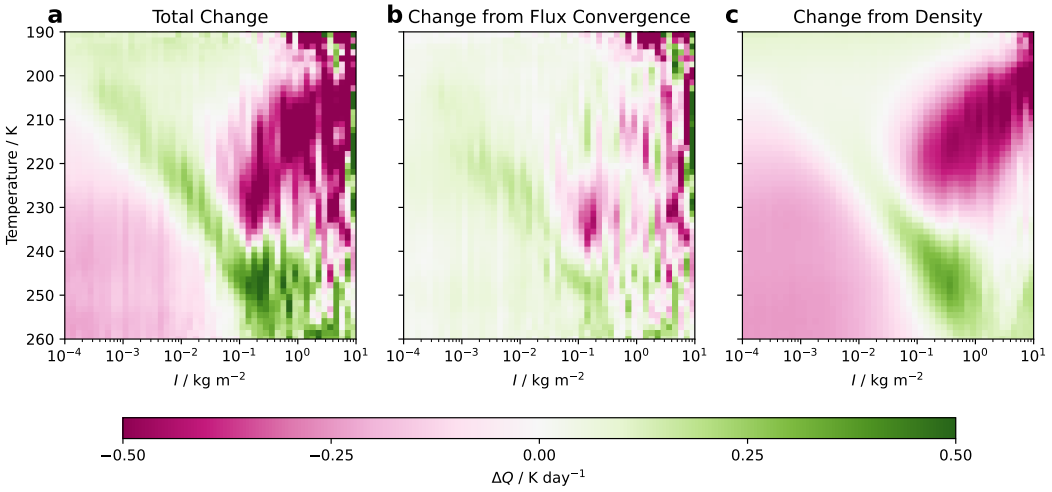


Figure B.S8: (**a**) Change in cloud radiative heating for the +4 K simulation and the decomposition of the change in heating rate into contributions from (**b**) the change in flux convergence and (**c**) the change in density.

B.S1.7 *Testing Convergence of Statistics*

To test whether three months of simulation are long enough to reach a statistically stable state, we investigate the most fragile quantity of our analysis, ΔP. When plotted with data from the first month, the first two months and all three months of simulation, ΔP shows convergence (Fig. B.S9). This proves that three months of simulation are sufficient to reach a statistically stable state.

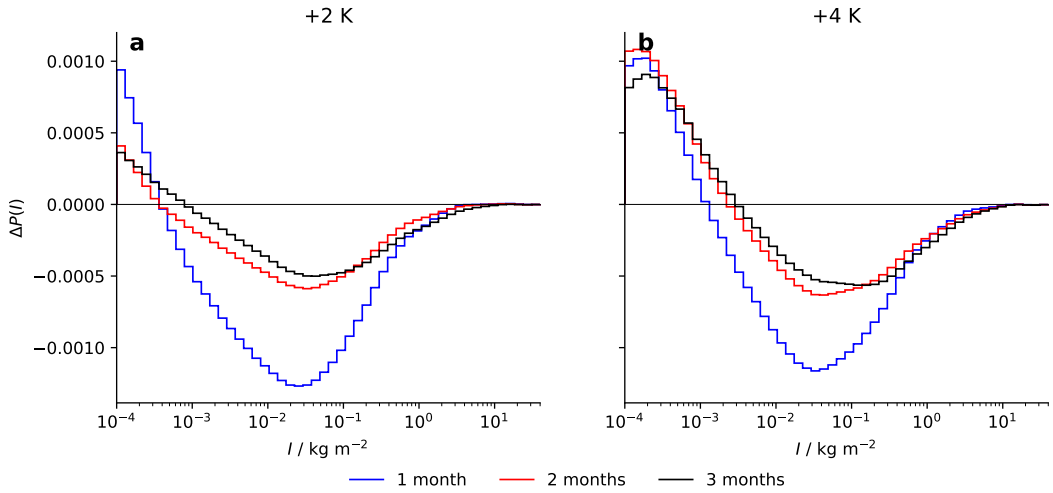


Figure B.S9: The difference between the ice water path frequency with respect to the control simulation ($\Delta P(I)$) based on data from the first month, the first two months and all three months of the simulations for (**a**) the +2 K and (**b**) the +4 K simulation.

B.S1.8 *Sensitivity to Connectedness of Liquid and Frozen Clouds*

Varying the threshold used to decide whether liquid clouds are part of the high, frozen cloud above mostly affects our estimate of the SW F_C (Fig. B.S10). This is explained by the SW C of liquid clouds being much stronger than their LW C (Deutloff et al., 2025a). In the paper, we use 5% as the threshold for connectedness.

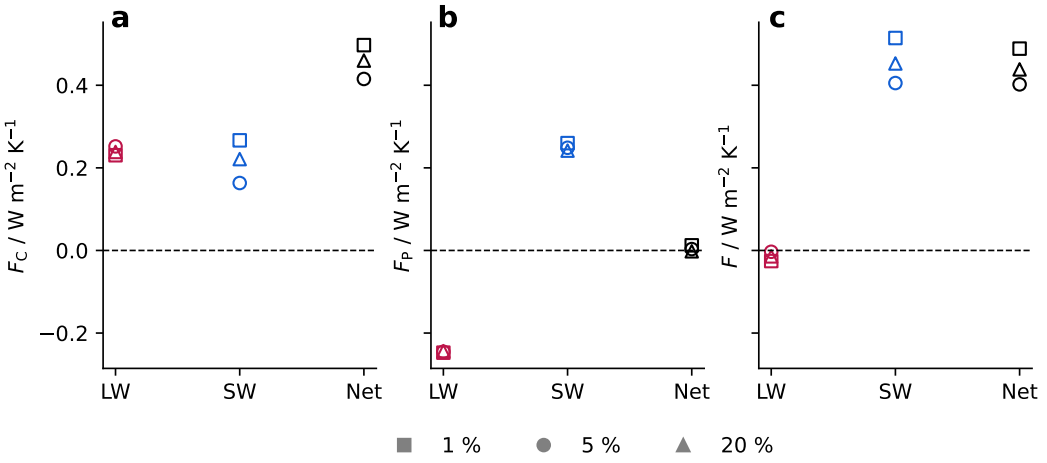


Figure B.S10: High-cloud feedback from the +4 K simulations for different thresholds in the calculation of connectedness. (**a**) Feedback from changes in $C(I)$, (**b**) feedback from changes in $P(I)$ and (**c**) total feedback.

B.S1.9 *Liquid Clouds at the Transition to Deep Convection*

Liquid clouds are typically not connected to the frozen clouds at low I, but become increasingly connected towards high I. According to our definition of high clouds, liquid clouds are part of the high clouds if the liquid and frozen condensate within a column sufficiently overlap (Eq. 3). The transition from liquid clouds being unconnected with the frozen clouds to liquid clouds being part of the high cloud occurs at $1\ \mathrm{kg\ m^{-2}} < I < 10\ \mathrm{kg\ m^{-2}}$ (Fig. B.S11).

Without the tuning factor in Eq. 3, this transition would shift towards higher I with warming, which would make the SW $C(I)$ become less negative. This is a consequence of liquid clouds being more reflective than the ocean surface. We regard this change in the SW $C(I)$ and the associated feedback to be artificial since it depends on subtle details of our definition of high clouds. Therefore, we introduce the tuning factor to keep the liquid cloud fraction constant with warming.

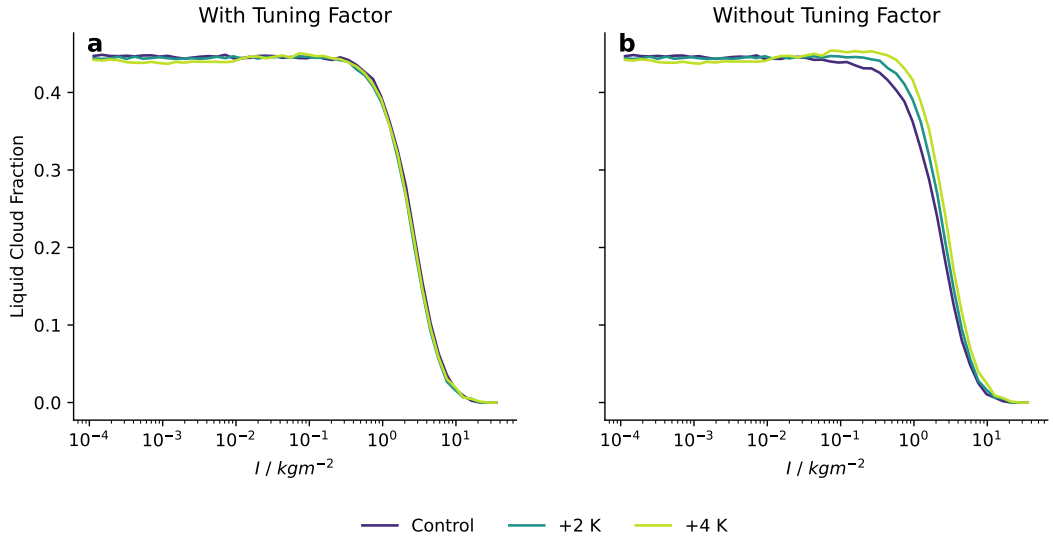


Figure B.S11: Fraction of liquid clouds with a liquid water path of more than $10^{-4}\ \mathrm{kg\ m^{-2}}$ that are not part of high clouds (**a**) with and (**b**) without including the tuning factor designed to keep the liquid cloud fraction constant with warming.

C

OBSERVED DIURNAL CYCLE CHANGE OF TROPICAL DEEP CONVECTION AMPLIFIES SURFACE WARMING

This paper is under review and available as a preprint:
J. Deutloff, S. A. Buehler, J. Windmiller, and A. K. Naumann (2026b). "Observed Diurnal Cycle Change of Tropical Deep Convection Amplifies Surface Warming." Preprint, under revision at Nature Geoscience. DOI: 10.21203/rs.3.rs-9293749/v1

Author Contributions: I conceptualised the study. S. A. Buehler, J. Windmiller and A. K. Naumann supervised the study and supported the conceptualisation. I conducted the analysis and wrote the manuscript with input from all co-authors. J. Windmiller produced Figure C4.

Observed Diurnal Cycle Change of Tropical Deep Convection Amplifies Surface Warming

Jakob Deutloff[1,2,3], Stefan A. Buehler[1,2], Julia Windmiller[4]
Ann Kristin Naumann[5]

[1]Earth System Sciences, Atmospheric Science, University of Hamburg, Hamburg, Germany.
[2]Earth and Society Research Hub (ESRAH), Hamburg, Germany.
[3]International Max Planck Research School on Earth System Modelling (IMPRS-ESM), Hamburg, Germany
[4]Monash University, Melbourne, Australia.
[5]Ludwig-Maximilians-Universität in Munich, Munich, Germany.

ABSTRACT

Climate feedbacks from changes in the diurnal cycle of clouds have received limited attention. However, recent storm-resolving aquaplanet simulations predict a partial shift of tropical deep convection from daytime to nighttime in response to surface warming, producing a positive feedback of similar magnitude as other cloud feedbacks. Here, we use satellite observations of ice water path to test whether such a feedback exists. We use the internal variability within 24 years of observations to regress the diurnal cycle of cloud fraction against surface temperature. We find that clouds produced by deep convection partly shift from daytime to nighttime with increasing surface temperature, over both land and ocean. This increases the amount of solar radiation absorbed by the surface and hence constitutes a positive climate feedback. We derive a global feedback value of 0.12 ± 0.02 W m^{-2} K^{-1} for this diurnal-cycle feedback, which adds to previous estimates of the cloud feedback, implying a higher climate sensitivity.

C1 INTRODUCTION

Understanding how clouds will amplify or dampen global warming remains a key challenge for narrowing down uncertainty in climate sensitivity. Among all climate feedbacks, the cloud feedback is most uncertain (Arias et al., 2021), which has motivated numerous studies on this aspect of climate change (Sherwood et al., 2020; Ceppi et al., 2017; Raghuraman et al., 2024; Zelinka et al., 2016; Zelinka et al., 2022). However, those studies do not include changes in the diurnal cycle of clouds, despite their potential to create a substantial feedback (Chen et al., 2025; Luo et al., 2024). If clouds shift from daytime to nighttime (or vice versa), this will decrease (increase) the amount of reflected solar radiation and hence amplify (dampen) surface warming.

One reason for the lack of studies targeting the feedback from changes in the diurnal cycle of clouds might be that the conventional framework for analysing the cloud feedback does not account for it. The typical decomposition of the cloud feedback only takes changes in mean cloud quantities into account, like altitude, optical depth

or cloud amount (Sherwood et al., 2020; Arias et al., 2021). This decomposition is usually done with cloud radiative kernels, which allow for separating changes in cloud properties from changes in the clear-sky atmosphere (Zelinka et al., 2012a; Zelinka et al., 2012b). However, cloud radiative kernels assume that clouds do not have a diurnal cycle. This makes it impossible to use them for detecting a feedback from changes in the diurnal cycle of clouds.

Another reason why changes in the diurnal cycle of clouds have received limited attention may be that suitable models for studying them only became available recently. The widely used Global Circulation Models (GCMs) are not ready for this task, since they rely on parameterisations of convection, which produce an unrealistic diurnal cycle (Christopoulos and Schneider, 2021; Covey et al., 2016). This limitation was overcome recently by the development of Global Storm-Resolving Models (GSRMs) that resolve convection explicitly, which leads to a correct representation of the diurnal cycle of convection (Stevens et al., 2020; Song et al., 2024; Eriksson et al., 2026).

Recent aquaplanet simulations with a GSRM predict that some of the tropical clouds produced by deep convection shift from daytime to nighttime in response to surface warming, which produces a positive feedback in these simulations (Deutloff et al., 2026a). The shift from daytime to nighttime is greatest for the thickest clouds with an ice water path (I) of $I \geq 1\ \mathrm{kgm^{-2}}$, referred to as deep convective clouds, but also affects thick anvil clouds with $1\ \mathrm{kgm^{-2}} > I \geq 0.1\ \mathrm{kgm^{-2}}$. The resulting feedback diagnosed from the GSRM simulations scaled to a global value is $0.1\ \mathrm{W\ m^{-2}\ K^{-1}}$ for a uniform surface warming of $2\ \mathrm{K}$ and $0.05\ \mathrm{W\ m^{-2}\ K^{-1}}$ for a $4\ \mathrm{K}$ warming. This would enhance the total cloud feedback of $0.45 \pm 0.33\ \mathrm{W\ m^{-2}\ K^{-1}}$ (Sherwood et al., 2020) by ten to twenty percent.

The change in the diurnal cycle of deep convection found in the aquaplanet simulations needs to be tested with observations to assess its realism and whether it also applies over land. The diurnal cycle of deep convection is more pronounced over land, where surface heating produces a strong afternoon peak of deep convection, whereas deep convection over the ocean peaks in the early morning hours due to enhanced radiative cooling of the atmosphere at nighttime (Ruppert and Hohenegger, 2018; Gray and Jacobson, 1977; Yang and Smith, 2006).

In this study, we use internal variability within satellite observations of I and two-meter temperature to test whether the positive feedback from changes in the diurnal cycle of tropical deep convection exists in the real world. We find that this is the case, with a partial shift of the deep convection from daytime to nighttime in response to surface warming. This is true over land and ocean, despite large land-ocean differences in the mean diurnal cycle. The change in the diurnal cycle of tropical deep convection and the resulting feedback is stronger in the observations than in the aquaplanet simulations.

C2 IDENTIFYING CLOUDS PRODUCED BY DEEP CONVECTION

We use I as a measure for cloud thickness to distinguish different types of tropical high clouds. This I-perspective has proven to be a valuable framework for analysing the high-cloud feedback (Sokol et al., 2024; Gasparini et al., 2019; Deutloff et al.,

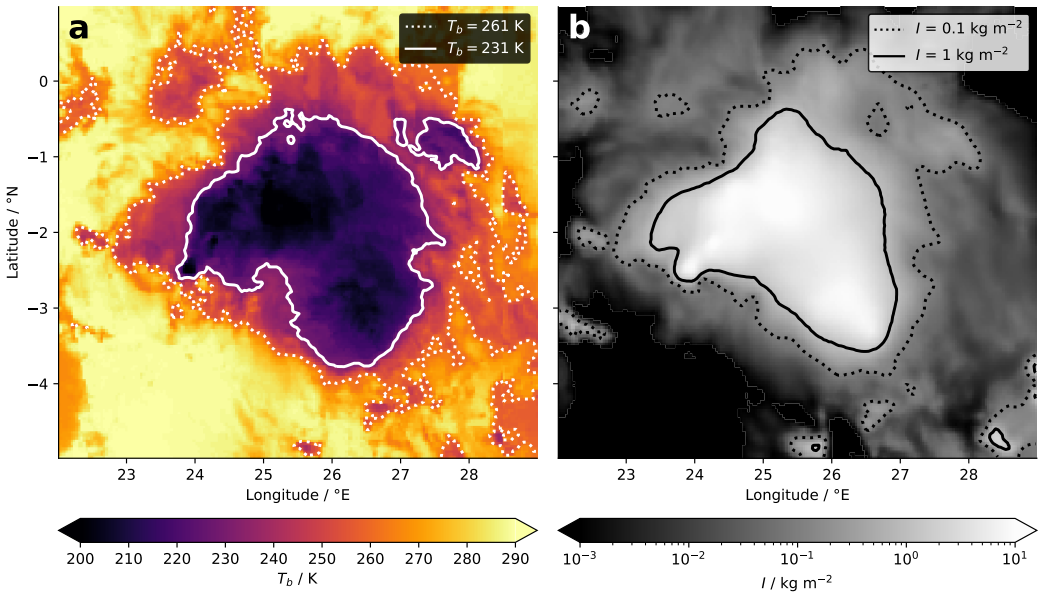


Figure C1: Brightness temperature T_b and corresponding ice water path I of a mesoscale convective system. Contour lines mark the threshold for deep convective clouds (solid) and thick anvils (dashed).

2026a; Deutloff et al., 2025a). We define deep convective clouds as $I > 1$ kg m^{-2} in agreement with earlier studies (Bolot et al., 2023; Deutloff et al., 2026a). While deep convective clouds have the closest link to deep convection, thick anvil clouds detrained from them might also feel changes in the diurnal cycle of deep convection and contribute to the total feedback. Therefore, we include all clouds with $I >$ 0.1 kg m^{-2} in our feedback estimate (Sec. C5).

Our analysis is based on the Chalmers Cloud Ice Climatology (CCIC) (Amell et al., 2024; Pfreundschuh et al., 2025), which uses machine learning to retrieve I from brightness temperature (T_b) measurements. The CCIC dataset has a horizontal grid spacing of 0.036°, a 30 minute timestep and is available for the 2000 to 2024 period. We cannot use direct satellite observations of I, since they are only available from sun-synchronous satellites (Deng et al., 2010; Delanoë and Hogan, 2010), and hence do not capture the diurnal cycle. To test the robustness of our results, we also use the T_b measurements (Janowiak et al., 2001; Janowiak et al., 2017) CCIC is based on to assess changes in the diurnal cycle of deep convective clouds. We constrain our analysis to the tropics (30°S to 30°N).

We establish comparability between measurements of I and T_b by making use of the fact that clouds with the highest I usually also have the coldest T_b. To derive thresholds in T_b that correspond to the I thresholds, we require the area (A) covered by clouds thicker than a given I_0 to match the area covered by clouds colder than the corresponding $T_{\mathrm{b},0}$:

$$A(I > I_0) = A(T_\mathrm{b} < T_{\mathrm{b},0}). \tag{1}$$

This yields a near-linear relationship of T_b and $\log_{10} I$ (Fig. C.S1) and suggests $T_b < 231$ K for deep convective clouds and $T_b < 261$ K for all clouds contributing to the feedback.

For an example mesoscale convective system, similar clouds are identified as deep convective clouds regardless of whether T_b or I are used (Fig. C1). The cloud area identified via T_b is slightly larger than the cloud area from I. This is possible because the area constraint in Eq. 1 used to derive the relationship of T_b and I is required to hold on average over the whole observation period, and will not hold for every individual scene. The cloud field appears smoother in I than in T_b. This is a consequence of the machine learning algorithm using the spatial structure of T_b to infer I, which causes the effective resolution of I to be lower than the resolution of T_b (Amell et al., 2024).

C3 DIURNAL CYCLE OF DEEP CONVECTION

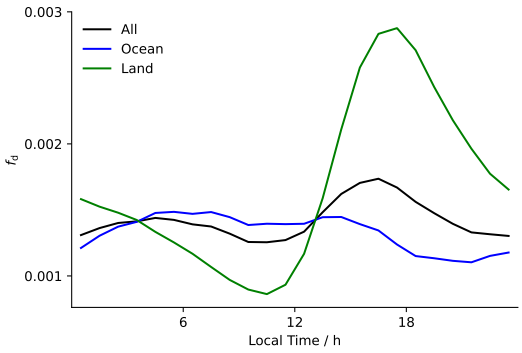


Figure C2: Mean deep convective cloud fraction (f_d) plotted against local time for the entire tropics (All) and for deep convective clouds over land and ocean.

We use the cloud fraction of deep convective clouds (f_d) to analyse the diurnal cycle of deep convection. To this end, we calculate f_d as a function of local time for areas over land, ocean, and the whole tropics by applying the I threshold defined for deep convective clouds (See Methods). The total area fraction covered by deep convective clouds can be derived by summing up f_d over local time, which yields 0.040 over land and 0.032 over ocean.

As expected (Hendon and Woodberry, 1993), the diurnal cycle of deep convection is much stronger over land than over ocean (Fig. C2). While deep convection over land has a pronounced peak at 17:30 local time, deep convection over ocean peaks at 5:30 and 14:30. The strong afternoon peak of convection over land is known to be driven by solar surface heating. (Yang and Slingo, 2001; Duvel, 1989). Absorbed solar radiation is causing surface temperatures to increase throughout the day, building up atmospheric instability that is consumed by convection in the late afternoon. Since the variability of surface temperature is smaller over ocean than over land, the diurnal cycle is less pronounced and mostly driven by radiative fluxes (Ruppert and Hohenegger, 2018; Yang and Smith, 2006).

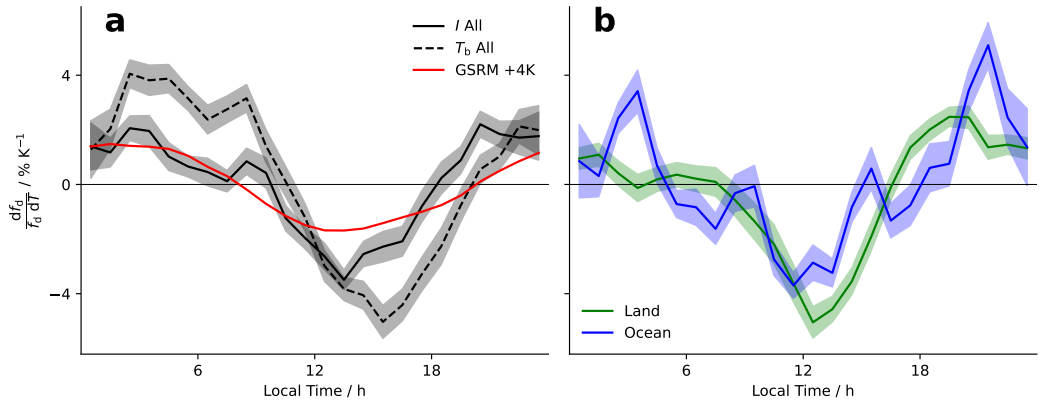


Figure C3: (**a**) Change of the diurnal cycle of deep convective cloud fraction (f_d) with two-meter temperature T in the tropics diagnosed from brightness temperatures (T_b) and ice water path (I) and from 4 K warming run of the GSRM aquaplanet simulations (Deutloff et al., 2026a). (**b**) Change of the diurnal cycle of f_d with T partitioned into land and ocean areas diagnosed from I. Shading marks the standard error of the linear regression.

C4 REDUCTION OF DAYTIME DEEP CONVECTION

We assess the change in f_d in response to surface warming by regressing detrended and deseasonalized timeseries of f_d against the corresponding two-meter temperature (T) from ERA5 (Hersbach et al., 2020). We normalise f_d at each timestep to exclude changes that are uniform across the day. Therefore, changes in f_d only account for a shift of the diurnal cycle and add up to zero (see Methods).

Deep convective clouds occur less during the day and more during the night in response to surface warming, confirming the result from GSRM aquaplanet experiments (Deutloff et al., 2026a) (Fig. C3a). This finding is robust, regardless of whether I or T_b are used to identify deep convective clouds. While the response of the diurnal cycle of f_d is similar in the GSRM and observations, the signal is larger in the observations. In the GSRM, the maximum decrease of f_d is -1.7 % K^{-1} at 13:30 local time, while it is -3.5 % K^{-1} at 13:30 for the I estimate and -5 % K^{-1} at 15:30 for the T_b estimate. One possible reason for the more pronounced change in the diurnal cycle diagnosed from T_b compared to the change diagnosed from I is the lower effective resolution of I (Sec. C2).

Changes in the diurnal cycle of deep convective clouds arise because the response of f_d to surface warming depends on local time. This becomes clear when we do not normalise f_d before regressing it against T, which reveals that deep convective clouds overall decrease, but more so during the day (Fig. C.S2). The overall decrease and the change in the diurnal cycle are of similar magnitude. Previous studies focusing on the change in high cloud amount, which includes deep convective clouds, missed the diurnal-cycle feedback since they only diagnosed the overall change in high cloud amount, and not how this decrease varies across the day (Sokol et al., 2024; McKim et al., 2024; Raghuraman et al., 2024; Wilson Kemsley et al., 2025).

The change in the diurnal cycle of deep convective clouds in response to surface warming is similar over land and ocean (Fig. C3b). This similarity is surprising, given

the vast differences in the mean diurnal cycle (Fig. C2) and points towards a shared driving mechanism that is independent of the surface type. It was speculated that a higher magnitude of cloud radiative heating in response to surface warming might drive the change in the diurnal cycle of deep convection (Deutloff et al., 2026a), but tailored mechanism-denial simulations will be necessary to test this hypothesis.

C5 POSITIVE DIURNAL-CYCLE FEEDBACK

Changes in the diurnal cycle of clouds only affect the shortwave part of the radiative balance, not the longwave part. The incoming shortwave radiation at the top of the atmosphere has a strong diurnal cycle, while the upwelling longwave radiation in clear-sky regions is almost constant in comparison (Fig. C.S3). Therefore, it is crucial at which local time a cloud occurs for the shortwave part of the radiative balance, while it is negligible for the longwave part. If clouds shift from daytime to nighttime in response to surface warming, more solar radiation is absorbed by the surface, which amplifies surface warming (Fig. C4).

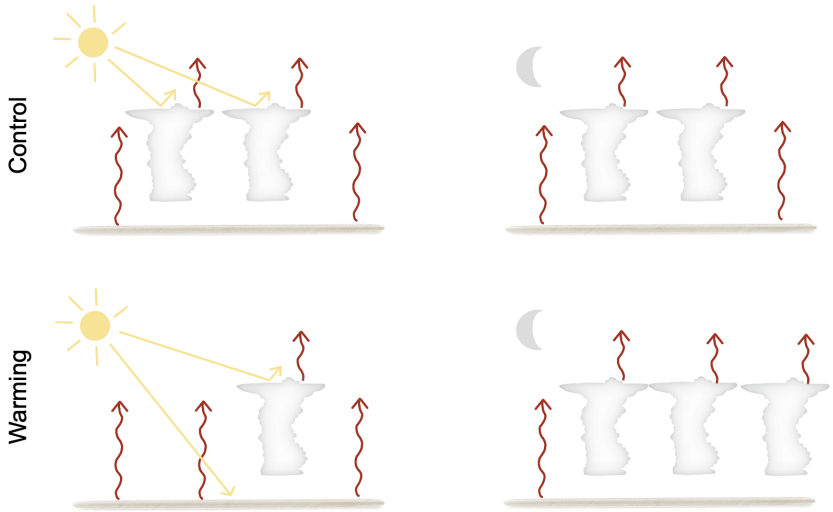


Figure C4: Schematic of the diurnal-cycle feedback. Red arrows represent the longwave radiative flux, yellow arrows represent the shortwave radiative flux. The upper row shows the control climate, while the bottom row shows a warmer climate.

To estimate the feedback from a reduction of daytime deep convection, we resolve cloud fraction f by cloud thickness measured by I to analyse how clouds with different thicknesses contribute to the total feedback. We include all clouds with $I > 0.1$ kg m^{-2} in our feedback estimate. Thinner clouds within this range might not be directly produced by deep convection, but still feel changes in the diurnal cycle of deep convection. As clouds become thinner than $I = 0.1$ kg m^{-2}, their albedo drops significantly (Fig. C.S4), hence they will not substantially contribute to the feedback.

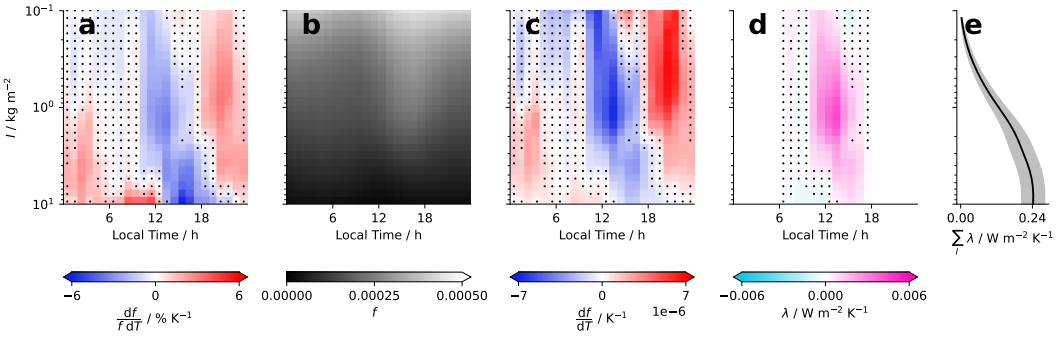


Figure C5: (**a**) Relative change in the diurnal cycle of f in response to surface warming, (**b**) temporal mean of f, (**c**) absolute change in diurnal cycle of f in response to surface warming, (**d**) feedback λ from changes in the diurnal cycle of f and (**e**) cumulative sum of λ over I. Dots indicate trends statistically insignificant at a 95% confidence level, and the shaded area in **d** visualises the standard deviation derived from bootstrapping.

We estimate the diurnal-cycle feedback (λ) by calculating the change in reflected solar radiation (R) caused by a change in the diurnal cycle of f. To this end, we approximate R as

$$R(l,I) = S(l) \cdot \alpha_{\mathrm{cl}}(l,I) \cdot f(l,I) + S(l) \cdot \alpha_{\mathrm{cs}} \cdot [1 - f(l,I)], \tag{2}$$

where α_{cl} is the cloud albedo, α_{cs} is the clear-sky albedo, S is the incoming solar radiation and l local time. The diurnal-cycle feedback λ is calculated as the change in R with T due to changes in the diurnal cycle of f and is defined as negative for increasing reflected radiation:

$$\lambda(l,I) = -\frac{\mathrm{d}R}{\mathrm{d}T}(l,I) = -S(l)\frac{\mathrm{d}f}{\mathrm{d}T}(l,I) \cdot [\alpha_{\mathrm{cl}}(l,I) - \alpha_{\mathrm{cs}}]\,. \tag{3}$$

We calculate $\alpha_{\mathrm{cl}}(l,I)$ and S from GSRM data (see Methods) and assume $\alpha_{\mathrm{cs}} = 0.1$. The change in the diurnal cycle of f with surface warming is derived from a linear regression of $f(l,I)$ against T in every (l,I) bin. Again, trends in $f(l,I)$ that are uniform across the day are excluded by normalising $f(l,I)$ for every timestep (see Methods). Since S is zero during the night, λ will also be zero at night. Clouds of all considered thicknesses occur less during the day and more during the night in response to surface warming (Fig. C5a). This signal is statistically significant for all clouds and strongest for the thickest clouds. The absolute change in f is derived by multiplying the relative change in f (Fig. C5a) with the mean f (Fig. C5b). Since clouds become less frequent the thicker they are, the absolute change in f is small for thick clouds (Fig. C5c).

Clouds around $I = 1$ kg m^{-2} contribute most to the positive feedback from the diurnal cycle change of deep convection (Fig. C5d). Thicker clouds are too few to produce a substantial λ, and as clouds become thinner than $I = 1$ kg m^{-2} their albedo starts to decrease (Fig. C.S4), which limits their ability to contribute to λ. That the majority of λ stems from clouds around $I = 1$ kg m^{-2} also becomes visible in the cumulative sum of λ over I, which has the largest slope at $I = 1$ kg m^{-2}.

The diurnal-cycle feedback is positive and of the same order of magnitude as other cloud feedbacks. We derive $\lambda = 0.24 \pm 0.04$ W m^{-2} K^{-1}, with the error estimate being derived from bootstrapping (see Methods). This is higher than the first estimates of the diurnal-cycle feedback from GSRM aquaplanet simulations (Deutloff et al., 2025a), which yield $\lambda = 0.2$ W m^{-2} K^{-1} for a 2 K surface warming and $\lambda = 0.1$ W m^{-2} K^{-1} for a 4 K surface warming. We scale our observational estimate of the diurnal-cycle feedback in the tropics to a global mean feedback by dividing the feedback value by two, since the tropics cover only half of the Earth's surface. The global mean diurnal-cycle feedback of $\lambda = 0.12 \pm 0.02$ W m^{-2} K^{-1} is of comparable magnitude to other cloud feedbacks, which range from 0.08 W m^{-2} K^{-1} to 0.25 W m^{-2} K^{-1} (Sherwood et al., 2020).

While internal variability within observations confirms the positive diurnal-cycle feedback found in idealised simulations, some questions remain open. It remains unclear whether the diurnal-cycle feedback diagnosed from internal variability is similar to the feedback acting on the long-term warming trend. Internal variability has been used before to assess the response of tropical high clouds to surface warming (Zelinka and Hartmann, 2011; Saint-Lu et al., 2022) and to constrain high-cloud feedbacks (McKim et al., 2024), but the similarity of the high-cloud response to warming from internal variability and the long-term trend has not yet been tested. A second open question is how the diurnal cycle of deep convection is impacted by CO_2 radiative forcing. If the mechanism causing the reduction of daytime deep convection depends on cloud radiative heating as hypothesised in (Deutloff et al., 2026a), it might be impacted by CO_2 directly.

C6 CONCLUSION

The diurnal cycle of tropical deep convection changes in response to surface warming, with deep convection occurring less during the day and more during the night. We confirm this finding from GSRM aquaplanet simulations (Deutloff et al., 2026a) by using the internal variability within satellite observations of ice water path. The response of the diurnal cycle of deep convection to surface warming is similar in the simulations and observations, but the magnitude of the response is about twice as large in the observations.

The change in the diurnal cycle of deep convection is remarkably similar over land and ocean, despite the mean diurnal cycle being much more pronounced over land. That daytime deep convection reduces similarly over land and ocean points towards a shared mechanism that is independent of the surface type. One proposed explanation is that a higher magnitude of cloud radiative heating in response to surface warming could alter the diurnal cycle of deep convection (Deutloff et al., 2026a). However, targeted mechanism-denial simulations are required to test this hypothesis.

The change in the diurnal cycle of clouds produced by deep convection results in a positive climate feedback that adds to previous assessments of the cloud feedback (Arias et al., 2021; Sherwood et al., 2020; Ceppi et al., 2017; Raghuraman et al., 2024; Zelinka et al., 2016; Zelinka et al., 2022), implying a higher climate sensitivity. Deep convective clouds and thick anvils reduce during the day, causing more solar radiation to be absorbed by the surface, which amplifies surface warming. Previous

studies targeting the feedback from tropical high clouds were not capturing this feedback because the diurnal cycle was averaged out in their analyses (Sokol et al., 2024; McKim et al., 2024; Wilson Kemsley et al., 2025; Raghuraman et al., 2024).

This study is one example of why it is necessary and timely to take climate science beyond the analysis of the mean state (Shaw and Stevens, 2025). It is timely because tools like machine learning and higher computational power enable datasets like CCIC (Amell et al., 2024; Pfreundschuh et al., 2025) and high-resolution simulations, which allow us to identify single deep convective cells and their diurnal cycle. It is necessary because otherwise important climate phenomena like the diurnal-cycle feedback would remain buried in the mean.

C7 METHODS

Our method is independent of whether I or T_b are used for identifying deep convective clouds. For simplicity, we only use I throughout the remainder of the methods section.

C7.1 *Histograms and Cloud Fraction*

At the heart of our analysis are histograms of I with three dimensions: local time in hours (l), I in $\mathrm{kg\ m^{-2}}$ and time (t) in months. For every month, we count the number of occurrences (N) within every I and l bin from the original I data, which has a 30-minute timestep and 0.036° horizontal grid spacing. The 3D histograms are calculated for the entire tropics (30°S to 30°N), as well as for tropical ocean and land areas separately.

We derive cloud fractions (f) averaged over the respective region from the histograms by division:

$$f(t,l,I) = \frac{N(t,l,I)}{\sum_{l=0}^{24}\sum_{I=0}^{\infty} N(t,l,I)}. \tag{4}$$

f should be interpreted as the area fraction covered by clouds within the respective (l,I) bin for a given month. The fraction of deep convective clouds (f_d) with $I > 1\ \mathrm{kg\ m^{-2}}$ for each local time is then calculated as

$$f_\mathrm{d}(t,l) = \sum_{I=1}^{\infty} f(t,l,I). \tag{5}$$

The total f_d is given by

$$f_\mathrm{d}(t) = \sum_{l=0}^{24} f_\mathrm{d}(t,l), \tag{6}$$

which should be interpreted as the cloud fraction with $I > 1\ \mathrm{kg\ m^{-2}}$ in the given month.

We neglect the dependence of grid cell area on the latitude in our calculation of N and hence also f. The I data is on a regular latitude longitude grid, so the grid cell area will decrease with $\cos(\phi)$, where ϕ is latitude. For our calculation of $N(t,l,I)$, we simply count the number of occurrences within every bin, without accounting

for the varying grid cell area by weighting with $cos(\phi)$. Implementing such an area weighting would complicate the calculation of $N(t,l,I)$ substantially. We regard this simplification as justified, since cos ϕ only varies from 0.87 to 1 within 30°S to 30°N.

C7.2 *Regression*

As the predictor for changes in f, we use the two-meter temperature (T) from ERA5 (Hersbach et al., 2020), which is area-weighted and averaged over the entire tropics, as well as over tropical land and tropical oceans separately. Since f has a monthly timestep, we use monthly means of T. The regression works the same for the 3D $f(t,l,I)$ and the 2D $f_\mathrm{d}(t,l)$. For simplicity, we only show equations for $f(t,l,I)$.

To isolate changes in the diurnal cycle of f from changes in f that are uniform across the diurnal cycle, we normalise cloud fractions with respect to local time, which we denote as $\bar{f}$:

$$\bar{f}(t,l,I) = \frac{f(t,l,I)}{\sum_{l=0}^{24} f(t,l,I)} \tag{7}$$

This ensures that $\sum_{l=0}^{24} \bar{f}_{I=x} = 1$ for every timestep, where $\bar{f}_{I=x}$ denotes the normalised cloud fraction at any I.

We detrend and deseasonalize $\bar{f}$ and T along the time dimension to isolate only El-Niño-driven internal variability (Fig. C.S5). To detrend the data, we subtract the linear trend over time. To deseasonalize the data, we subtract the mean annual cycle. The resulting timeseries of $\bar{f}$ and T are used to calculate their linear regression within every (l,I) bin. The slope (s) derived from the linear regression is used to calculate the relative change in the diurnal cycle of f as

$$\frac{\mathrm{d}f}{f\mathrm{d}T}(l,I) = \frac{s(l,I)}{\langle \bar{f}(t,l,I) \rangle} \cdot 100\%, \tag{8}$$

where $\langle \cdot \rangle$ denotes the temporal mean over the whole timeseries.

C7.3 *Feedback*

We calculate the diurnal-cycle feedback (λ) from clouds with $I > 0.1$ kg m^{-2} with Eq. 3. The cloud albedo (α_cl) used in Eq. 3 is calculated from the radiative fluxes of the GSRM aquaplanet control simulation described in (Deutloff et al., 2026a) using the method from (Deutloff et al., 2025a). That means α_cl is calculated from the all-sky albedo $\alpha_\mathrm{as} = R_\mathrm{as}/S$ with R_as being the reflected all-sky SW flux at the top of the atmosphere (TOA) and the clear-sky albedo $\alpha_\mathrm{cs} = R_\mathrm{cs}/S$ with R_cs being the reflected clear-sky SW flux at TOA:

$$\alpha_\mathrm{cl} = \frac{\alpha_\mathrm{as} - \alpha_\mathrm{cs}}{1 + \alpha_\mathrm{cs}(\alpha_\mathrm{as} - 2)}.$$

We bin α_cl by I and l to calculate the mean $\alpha_\mathrm{cl}(l,I)$ (Fig. C.S4).

The incoming solar radiation is also diagnosed from the aquaplanet GSRM simulations (Fig. C.S3). We use one day (2021-07-02) of the coupled ICON-C4 simulation

described in (Segura et al., 2025b) to calculate the upwelling longwave radiation in tropical clear-sky regions (Fig. C.S3). While this quantity is not necessary to calculate λ, we use it to argue why λ only acts in the shortwave spectrum (Sec. C5).

The total λ is calculated as

$$\lambda = \sum_{l=0}^{24} \sum_{I=0.1}^{\infty} \lambda(l, I). \tag{9}$$

C7.4 *Bootstrapping*

We estimate the uncertainty in λ using block bootstrapping applied to the linear regression between f and T. To account for the autocorrelation in T, which persists for up to three years (Fig. C.S5), we randomly sample three-year segments from the time series. We draw eight blocks to closely match the length (n) of the bootstrap and original time series. The starting indices i_k, $k = 1, \ldots, 8$, are randomly drawn from $\{0, 1, \ldots, n - 36\}$ without replacement. The bootstrapped time series are defined as

$$T_{\mathrm{bs}}(t) = \left\{ T(t_{i_k}, \ldots, t_{i_k+36}) \right\}, \tag{10}$$

$$f_{\mathrm{bs}}(t, l, I) = \left\{ f(t_{i_k}, \ldots, t_{i_k+36}, l, I) \right\}. \tag{11}$$

The bootstrapped time series $T_{\mathrm{bs}}(t)$ and $f_{\mathrm{bs}}(t, l, I)$ are then used to recompute $\mathrm{d}f/f\mathrm{d}T(l, I)$ via linear regression (Eq. 8), from which λ is calculated using Eq. 3. We calculate the mean and standard deviation of λ from 2000 bootstrap samples, which is the sample size for which λ converges (Fig. C.S6).

ACKNOWLEDGEMENTS

The authors thank Blaž Gasparini and James Ruppert for inspiring discussions.

FUNDING

This research was funded by the Deutsche Forschungsgemeinschaft (DFG, German Research Foundation) under Germany's Excellence Strategy – EXC 2037 'CLICCS - Climate, Climatic Change, and Society' – Project Number: 390683824. This work used resources of the Deutsches Klimarechenzentrum (DKRZ) granted by its Scientific Steering Committee (WLA) under project ID bm1183.

CODE AVAILABILITY

The code to reproduce the figures and numbers from this paper is available from `https://doi.org/10.5281/zenodo.19245767` (Deutloff, 2024).

DATA AVAILABILITY

The CCIC data was accessed on 2026-01-08 and is available from `https://registry.opendata.aws/ccic`. The brightness temperature data was accessed on 2025-11-19 and is available from `https://disc.gsfc.nasa.gov/datasets/GPM_MERGIR_1/`

`summary`. The data to reproduce the figures and numbers from this paper is available from `https://doi.org/10.5281/zenodo.19245784` (Deutloff, 2026b).

AUTHOR CONTRIBUTION

All authors contributed to designing the research. J.D. carried out the research and wrote the paper with input from all co-authors. J.W. designed the schematic (Fig. C4).

C.S1 SUPPLEMENT

C.S1.1 *Relation of Brightness Temperature and Ice Water Path*

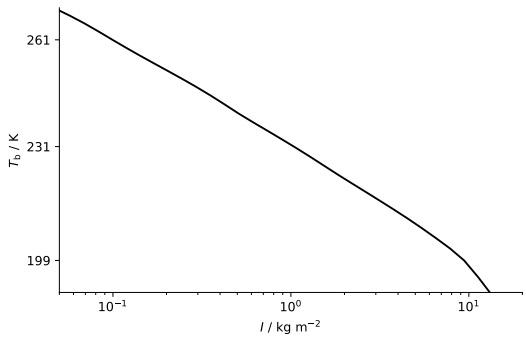


Figure C.S1: Brightness temperature (T_b) as a function of ice water path (I) derived from the area constraint.

C.S1.2 *Total Change in Deep Convective Clouds*

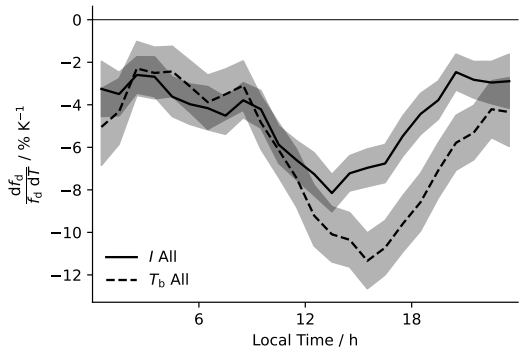


Figure C.S2: Change of the deep convective cloud fraction (f_d) with two-meter temperature T in the tropics diagnosed from brightness temperatures (T_b) and ice water path (I).

C.S1.3 *Diurnal Cycle of Radiative Fluxes*

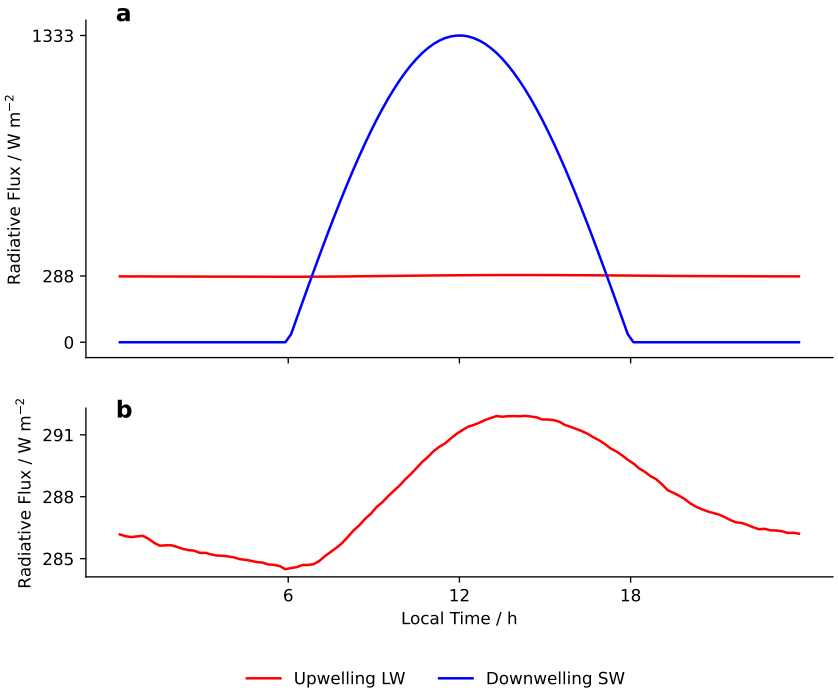


Figure C.S3: (**a**) Diurnal cycle of the downwelling shortwave (SW) flux and the upwelling longwave (LW) flux in tropical clear-sky regions. (**b**) Diurnal cycle of only the upwelling LW flux in tropical clear-sky regions.

C.S1.4 *Albedo*

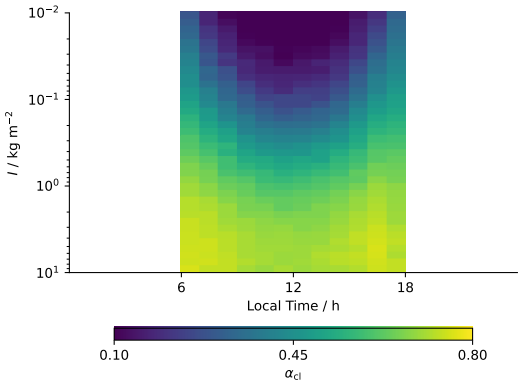


Figure C.S4: Cloud albedo (α_{cl}) binned by ice water path (I) and local time.

C.S1.5 *Bootstrapping of Regression*

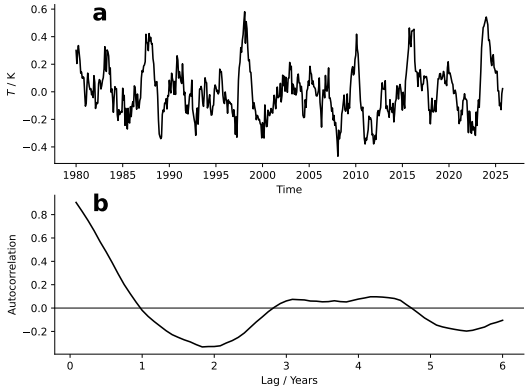


Figure C.S5: **a**) Deseasonalized and detrended time-series of monthly mean two-meter temperature (T) and (**b**) autocorrelation of T.

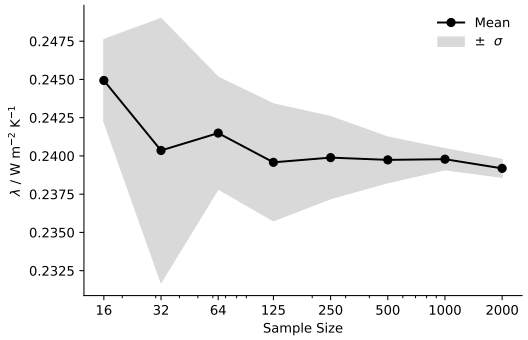


Figure C.S6: Feedback from changes in the diurnal cycle of deep convection (λ) for different bootstrap sample sizes. Dots mark the mean estimate from five bootstrap samples with the respective sample size. Grey shading visualises the standard deviation of the mean λ from the five samples.

D

WEAK POSITIVE FEEDBACK FROM OBSERVED REDUCTION OF TROPICAL ANVIL CLOUDS

This paper is currently in preparation.

Author Contributions: I conceptualised the study. S. A. Buehler, J. Windmiller and A. K. Naumann supervised the study and supported the conceptualisation. I conducted the analysis and wrote the manuscript with input from all co-authors.

Weak Positive Feedback from Observed Reduction of Tropical Anvil Clouds

Jakob Deutloff[1,2,3], Stefan A. Buehler[1,2], Julia Windmiller[4]
Ann Kristin Naumann[5]

[1]Earth System Sciences, Atmospheric Science, University of Hamburg, Hamburg, Germany.
[2]Earth and Society Research Hub (ESRAH), Hamburg, Germany.
[3]International Max Planck Research School on Earth System Modelling (IMPRS-ESM), Hamburg, Germany
[4]Monash University, Melbourne, Australia.
[5]Ludwig-Maximilians-Universität in Munich, Munich, Germany.

ABSTRACT

It was debated for more than two decades whether a strong negative climate feedback from a reduction of tropical anvil clouds exists. Two recent studies based on idealised simulations suggest that this feedback is neutral to weakly positive since the positive feedback from a reduction of thick, cooling clouds is largely cancelled by the negative feedback from a reduction of thin, warming clouds. Both studies resolve the spectrum of tropical high clouds by ice water path (I) as a measure of cloud thickness to derive this insight. We adopt their approach to test their result with four different satellite retrievals of I. All retrievals agree with the idealised simulations that tropical high clouds at the I range of anvil clouds reduce in response to surface warming, but the signal is more than two times stronger in the observations. The observations confirm that the feedback is weakly positive since the positive feedback from a reduction of thick, cooling clouds is largely cancelled by the negative feedback from a reduction of thin, warming clouds. We derive a total feedback of 0.05 ± 0.01 $\mathbf{W\ m^{-2}\ K^{-1}}$ from the observations, which is weak compared to other cloud feedbacks.

D1 INTRODUCTION

Limited understanding of the cloud response to global warming continues to cause uncertainty in climate sensitivity. Among all climate feedbacks, the cloud feedback is most uncertain (Arias et al., 2021). In an extensive review on climate sensitivity carried out as part of the World Climate Research Programme (WCRP), the feedback from changes in tropical anvil-cloud amount was identified as the main source of uncertainty in the total cloud feedback (Sherwood et al., 2020).

It was debated for more than two decades whether tropical anvil clouds would reduce in response to surface warming and thereby produce a strong negative feedback. This idea was first brought up by Lindzen et al. (2001), who claimed that precipitation efficiency will increase with surface warming, causing less cloud condensate to be available for the formation of anvil clouds. The reduced amount of anvil clouds was thought to cool the Earth since more longwave radiation could be emitted to space. They termed this negative feedback the infrared iris. The infrared iris was heavily debated (Hartmann and Michelsen, 2002; Lindzen et al., 2002; Fu et al., 2002; Lin et al., 2004; Chou and Lindzen, 2005; Mauritsen and Stevens, 2015; Lindzen and Choi, 2022) and eventually replaced by the stability iris as the common theory to explain the response of anvil clouds to warming (Bony et al., 2016). The stability iris explains the reduction of tropical anvil clouds in response to surface warming by an increase in atmospheric stability, which is backed by observations (Saint-Lu et al., 2020) and simulations (Bony et al., 2016; Saint-Lu et al., 2022). However, the stability iris only predicts a decrease of tropical anvil clouds in response to warming without quantifying the resulting feedback. The WCRP assessment estimated the feedback from changes in tropical anvil-cloud amount to be -0.2 ± 0.2 W m^{-2} K^{-1}, based on one observational study (Williams and Pierrehumbert, 2017).

The high uncertainty assigned to the tropical anvil-cloud amount feedback by the WCRP assessment has motivated several recent studies, which all conclude that this feedback is close to zero (McKim et al., 2024; Sokol et al., 2024; Wilson Kemsley et al., 2025; Raghuraman et al., 2024; Deutloff et al., 2026a). To understand the nature of the feedback from changes in tropical anvil-cloud amount, sorting all high clouds by their thickness, measured by ice water path (I), has proven to be a crucial (Sokol et al., 2024; Deutloff et al., 2026a; Deutloff et al., 2025a; Gasparini et al., 2023). Adopting this I perspective is necessary since the cloud radiative effect (C) strongly varies with I, being positive for thin clouds, and negative for thick clouds.

Resolving the I spectrum of high clouds reveals that high clouds in the I range of anvil clouds do reduce in response to surface warming, but with a near-neutral feedback since the positive feedback from a reduction of thick, cooling clouds is largely cancelled by the negative feedback from a reduction of thin, warming clouds. Cloud-resolving radiative-convective equilibrium (RCE) simulations from the RCEMIP experiment (Wing et al., 2018) have a weak positive anvil-cloud amount feedback since the positive feedback from the reduction of thick high clouds dominates (Sokol et al., 2024). The cancellation of positive and negative feedbacks is almost perfect in global storm-resolving aquaplanet simulations, resulting in a near-neutral anvil cloud-amount feedback (Deutloff et al., 2026a).

We use satellite observations of I to test whether anvil clouds reduce with a near-neutral feedback due to a cancellation of the positive feedback from a reduction of thin, warming clouds and the negative feedback from the reduction of thick, cooling clouds as predicted by idealised simulations. We find that this cancellation is confirmed, but the positive feedback from a reduction of thick, cooling clouds predominates, causing the total feedback to be weakly positive.

D2 ICE WATER PATH FRAMEWORK

Resolving the spectrum of tropical high clouds by I as a measure for cloud thickness is crucial for understanding the tropical high-cloud feedback since the cloud radiative effect (C) strongly varies with I. The I framework was introduced by Sokol et al. (2024), and further refined by Deutloff et al. (2025a). Within this framework, the total high-cloud radiative effect ($\overline{C}$) is calculated as

$$\overline{C} = \sum_I C(I) \cdot P(I),$$

where $C(I)$ is the high-cloud radiative effect at a given I and $P(I)$ is its frequency. The frequency $P(I)$ should be interpreted as the I resolved high-cloud fraction. The sum of $P(I)$ over a given I interval yields the area fraction covered by clouds within this interval. The feedback (λ) from changes in $P(I)$ is calculated as the change in $\overline{C}$ that is due to changes in $P(I)$ in response to surface warming

$$\lambda = \frac{\mathrm{d}\overline{C}}{\mathrm{d}P(I)} \frac{\mathrm{d}P(I)}{\mathrm{d}T} = \sum_I C(I) \frac{\mathrm{d}P(I)}{\mathrm{d}T}, \tag{1}$$

where T is the tropical mean surface temperature. We use $P(I)$ from four different observational datasets (Sec. D3), which are compared to the RCEMIP simulations (Sokol et al., 2024) and the ICON aquaplanet simulations (Deutloff et al., 2026a) (Fig. D1a). For $C(I)$, we use the estimate from the ICON aquaplanet control simulation (Deutloff et al., 2026a) (Fig. D1b). While thin clouds with $I < 0.2\ \mathrm{kg\ m^{-2}}$ have a positive $C(I)$, thick clouds have a negative $C(I)$. The reason for this shape of $C(I)$ is that for the thin clouds, the positive longwave $C(I)$ dominates, while thick clouds are more reflective and hence their negative shortwave $C(I)$ dominates (Deutloff et al., 2025a).

Sorting tropical high clouds by their I also allows us to distinguish different types of high clouds. The thickest clouds with $I > 1\ \mathrm{kg\ m^{-2}}$ are usually generated by deep convection, while anvils are of intermediate thickness with $1\ \mathrm{kg\ m^{-2}} \geq I > 0.01\ \mathrm{kg\ m^{-2}}$ and cirrus clouds are thinnest (Sokol and Hartmann, 2020; Deutloff et al., 2026a). Different responses of those three cloud types to surface warming are expected. The thickest deep convective clouds are expected to carry more ice as deep convection intensifies (Bolot et al., 2023), while anvils are expected to decrease in frequency (Bony et al., 2016).

D3 SATELLITE OBSERVATIONS OF ICE WATER PATH

The most accurate satellite observations of I make use of the synergy of collocated radar and lidar measurements (Eriksson et al., 2026). Optically thin clouds are often

only detected by the lidar since it is more sensitive than the radar. Optically thick clouds are fully detected by the radar, while the lidar only sees their cloud top due to attenuation. We use two retrievals of I that are based on the CloudSat radar (Stephens et al., 2002) and the CALIPSO lidar (Winker et al., 2010) measurements: 2C-ICE R05 (Deng et al., 2010) and DARDAR v3.1 (Cazenave et al., 2019). Both retrievals use the same radar and lidar measurements but employ different algorithms to retrieve I. The horizontal resolution of both retrievals is 1.1 km. Since CloudSat and CALIPSO fly on a sun-synchronous polar orbit, I from DARDAR and 2C-ICE is only available at 1:30 AM and 1:30 PM local time. Due to a battery anomaly, the CloudSat radar was limited to daytime-only observations after 2011. For consistency, we therefore only use the daytime retrievals of I from DARDAR and 2C-ICE, for the period of 2006-07 to 2019-06 and 2006-07 to 2018-12, respectively. To overcome the sparsity of direct I observations, we use two datasets that infer I from more abundant satellite observations with machine learning. We use the Chalmers Cloud Ice Climatology (CCIC) (Amell et al., 2024; Pfreundschuh et al., 2025) that uses a machine learning algorithm trained on 2C-ICE to infer I from the spatial structure of brightness temperature observed by geostationary satellites. The CCIC dataset has a horizontal grid spacing of 0.036°, a 30 minute timestep and is available for the 2000 to 2024 period. We also use SPARE-ICE (Holl et al., 2014), which employs a machine learning algorithm, also trained on 2C-ICE, to retrieve I from infrared and microwave radiances. We use the SPARE-ICE retrieval based on measurements from the MetOp A and MetOp B satellites, which fly on a sun-synchronous polar orbit with crossing times of 9:30 AM and 9:30 PM local time. The horizontal resolution of SPARE-ICE based on the MetOp A/B satellites is 20 km. We use MetOp A for the 2007-05 to 2020-01 period, and MetOp B for the 2020-01 to 2025-07 period.

The $P(I)$ derived from the four I retrievals differs substantially. They agree that $P(I)$ increases from high I to low I, but their agreement becomes worse with decreasing I (Fig. D1a). The two machine learning retrievals CCIC and SPARE-ICE do not stand out as especially unrealistic compared to DARDAR and 2C-ICE, since the latter also differ substantially, even though they are based on the same radar and lidar observations. Some differences in $P(I)$ between the retrievals are to be expected, since they observe different scenes. While 2C-ICE and DARDAR only include clouds at 1:30 PM local time, SPARE-ICE only includes clouds at 9:30 AM and 9:30 PM local time, while CCIC includes clouds in the entire tropics every 30 minutes. However, the differences in $P(I)$ seem to be mainly caused by differences in the retrieval algorithm. When CCIC is subsampled to local times around 1:30 PM to match the 2C-ICE and DARDAR observations, the differences between the retrievals remain (Figure 3b in Eriksson et al. (2026)).

The RCEMIP models (Sokol et al., 2024; Wing et al., 2018) and the ICON aquaplanet simulations (Deutloff et al., 2026a) agree with the observations on the general shape of $P(I)$ but have too few deep convective clouds with $I > 1\ \mathrm{kg\ m^{-2}}$. This seems to be a general bias of cloud-resolving models, which was also found in more realistic simulations (Turbeville et al., 2022).

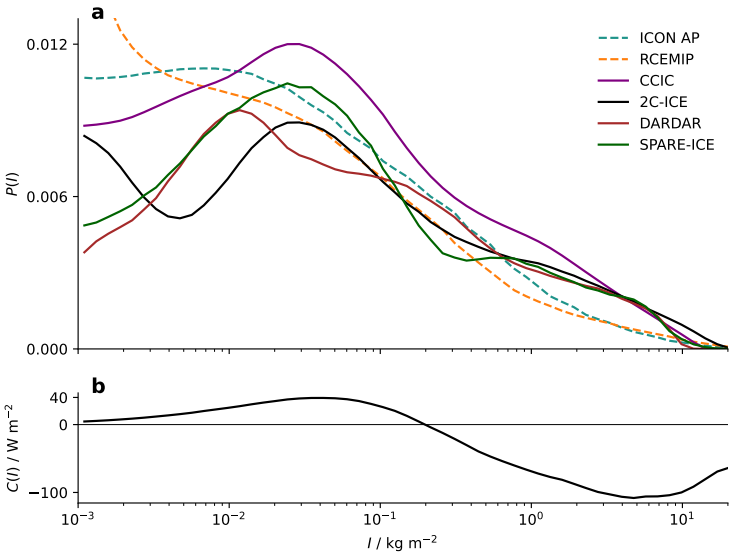


Figure D1: (**a**) Ice water path (I) frequency (P) from satellite retrievals for 2016, the ensemble mean of all RCEMIP models at 295 K (Sokol et al., 2024) and the ICON aquaplanet control simulation (Deutloff et al., 2026a). (**b**) High-cloud radiative effect (C) from the ICON aquaplanet control simulation (Deutloff et al., 2026a).

D4 REDUCTION OF ANVIL CLOUDS

We assess changes in $P(I)$ with warming by regressing $P(I)$ on the tropical mean two-meter temperature (T) from ERA5 (Hersbach et al., 2020) at a monthly time step (See Methods). Following the methodology of Bolot et al. (2023), we detrend and deseasonalize the data before performing the regression to isolate internal variability, which is mostly driven by the El Niño Southern Oscillation (ENSO).

The response of $P(I)$ to surface warming is similar for all I observations, but the differences between observations and the models are significant (Fig. D2a). The similarity of the response of $P(I)$ to surface warming among the observations is surprising, given the significant differences in their mean $P(I)$ (Fig. D1a). While the pattern of the change in $P(I)$ looks similar for observations and models, the magnitude of this response is more than twice as strong in the observations (Fig. D2a).

Simulations and observations agree that tropical high clouds in the I range of anvil clouds decrease in response to surface warming (Fig. D2a). This decrease is statistically significant for all observational datasets at a 95% confidence level between $I = 4$ kg m^{-2} and $I \approx 0.03$ kg m^{-2}, with the lower bound varying between the observational datasets (Fig. D2b). The maximum decrease in $P(I)$ is between $I = 0.05$ kg m^{-2} (2C-ICE) and $I = 0.7$ kg m^{-2} (SPARE-ICE) for the observations, at $I = 0.3$ kg m^{-2} for RCEMIP and at $I = 0.04$ kg m^{-2} for the ICON aquaplanets.

That the decrease of $P(I)$ is strongest in the I range of anvil clouds agrees with the decrease of tropical anvil clouds expected from the stability iris theory (Bony et al., 2016). The stability iris theory was confirmed before based on observations, but the clouds were not resolved by I (Saint-Lu et al., 2020). The increase in $P(I)$ at the highest I found in all observational datasets except for 2C-ICE agrees with

Bolot et al. (2023). They argue that deep convective updrafts become more intense and carry more ice at higher surface temperatures.

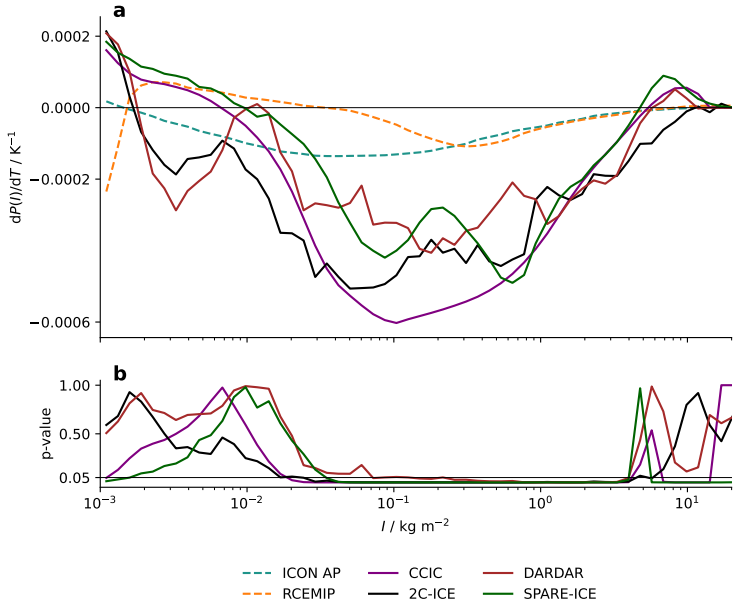


Figure D2: (**a**) Change of ice water path (I) frequency (P) with surface temperature T in the satellite observations calculated via linear regression, ensemble mean change in $P(I)$ from the RCEMIP simulations (Sokol et al., 2024) and change in $P(I)$ from ICON aquaplanet simulations (Deutloff et al., 2026a). (**b**) p-value of the linear regression used to derive $\mathrm{d}P(I)/\mathrm{d}T$ from observations.

D5 WEAK POSITIVE FEEDBACK

We calculate the feedback (λ) from changes in $P(I)$ by multiplying them with $C(I)$ (eq. 1). The resulting $\lambda(I)$ is the feedback in every I bin, and the sum of $\lambda(I)$ over I gives the total feedback.

The feedback from changes in $P(I)$ with surface warming is small because the positive feedback from a reduction of thick clouds with a negative $C(I)$ is largely cancelled by the negative feedback from a reduction of thin clouds with a positive $C(I)$ (Fig. D3a, b). This is true for all observational datasets and models, but the degree to which this cancellation holds differs. A negative λ is only found for the ICON aquaplanet simulations. The RCEMIP models and all observational datasets agree that λ is positive since the positive feedback from a reduction of thick, cooling clouds predominates.

The feedback from changes in tropical high-cloud frequency is weak compared to other cloud feedbacks. Vales of λ derived from the observations vary between 0.08 W m^{-2} K^{-1} (CCIC) and 0.13 W m^{-2} K^{-1} (SPARE-ICE). Since we calculate λ only for the tropics, it needs to be divided by two to be scaled to a global feedback as the tropics cover only half of the Earth's surface. Scaled to a global feedback, the mean and standard deviation of λ from the observational datasets is

$\lambda = 0.05 \pm 0.01$ W m^{-2} K^{-1}. The magnitude of other cloud feedbacks ranges from 0.08 W m^{-2} K^{-1} to 0.25 W m^{-2} K^{-1} (Sherwood et al., 2020)

To establish comparability to earlier studies, we decompose λ into a feedback from changes in high-cloud area and a feedback from changes in high-cloud opacity, following Sokol et al. (2024). The area feedback is calculated as the overall change in high-cloud fraction times $\overline{C}$. The area feedback is small because $\overline{C}$ is near-neutral, supporting the argument of McKim et al. (2024) against a strong area feedback. Our result of a near-neutral area feedback agrees with recent observational estimates (Raghuraman et al., 2024) and modelling studies (Wilson Kemsley et al., 2025). The opacity feedback arises since the change in high-cloud fraction is non-uniform across I, i.e. it describes the feedback from a shift in the balance between cooling and warming high clouds. That this opacity feedback is positive was first found by Sokol et al. (2024) based on the RCEMIP simulations, and is confirmed by our analysis of I observations. While this decomposition is necessary to establish comparability to earlier studies, we don't think it helps the intuition for the feedback from changes in high-cloud frequency. The cancellation from a reduction of thick, cooling and thin, warming is easily understood when calculating $\lambda(I)$, but gets harder to grasp when decomposing λ into an area and an opacity feedback.

Despite referring to it as the "tropical anvil cloud area feedback", the WCRP assessment does not distinguish between an area and an opacity feedback, and neither does Williams and Pierrehumbert (2017), which the WCRP estimate is based on. Therefore, λ can be directly compared to the WCRP feedback estimate of -0.2 ± 0.2W m^{-2} K^{-1}. Given that our estimate of λ is weakly positive in agreement with other recent studies (see above), the WCRP estimate seems highly unlikely.

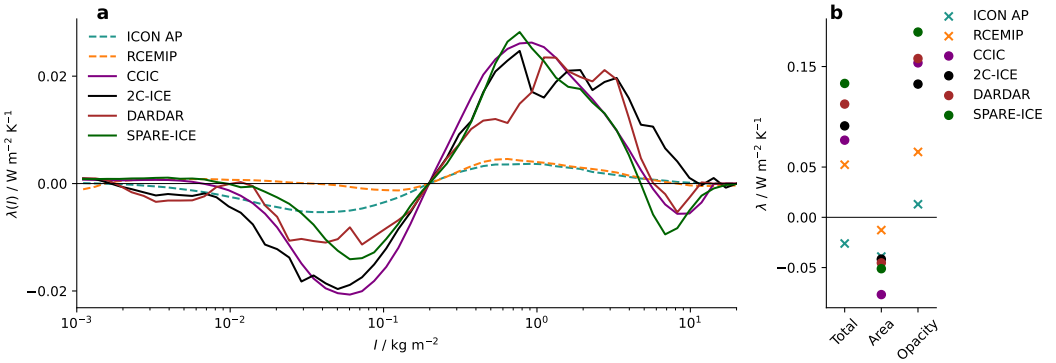


Figure D3: (**a**) Feedback (λ) from changes in ice water path (I) frequency as a function of I from the observations and from the ensemble mean of the RCEMIP simulations (Sokol et al., 2024) and the ICON aquaplanet simulations (Deutloff et al., 2026a). (**b**) The total λ and the total λ partitioned into the area feedback and the opacity feedback.

D6 LINGERING QUESTIONS

It remains unclear why the change in $P(I)$ is more than twice as strong in the observations compared to the models (Fig. D2a). One key difference between the observations and the models is that the warming from internal variability has a spatial

pattern, while the warming in the simulations is spatially uniform. Whether the response of tropical high clouds to warming depends on the warming pattern is unclear. Known biases of cloud-resolving models might also contribute to the disagreement of models and observations. Convective systems in cloud-resolving models are usually too small and short-lived, which is described as the "popcorn convection" bias (Becker et al., 2021; Feng et al., 2023).

We plan to analyse the spatial pattern of the change in $P(I)$ in the observations to better understand why their tropical mean change in $P(I)$ differs from the models. The influence of land might explain some of the differences, since the RCEMIP simulations (Sokol et al., 2024) and the ICON aquaplanet simulations (Deutloff et al., 2026a) are only representative of convection over the ocean, while we include the entire tropics in the observations.

We also plan to analyse how well the decrease in $P(I)$ in the I range of anvil clouds is explained by the stability iris theory (Bony et al., 2016). It was shown before that the stability iris theory explains the observed decrease of tropical anvil clouds in response to warming on an annual timescale (Saint-Lu et al., 2020). However, it remains unclear how well this theory applies across the I space, and if it also holds on the monthly timescale used in our study.

D7 CONCLUSION

Resolving the spectrum of tropical high clouds by I as a measure for cloud thickness is crucial to understand the feedback from changes in high-cloud frequency. The reason for this is that the cloud radiative effect strongly varies with I. While thin clouds have a positive cloud radiative effect, it becomes negative for thick clouds with $I > 0.2$ kg m^{-2}. Therefore, the feedback from changes in high-cloud frequency depends on whether thin or thick clouds are affected.

The four observational datasets of I agree that the frequency of clouds in the I range of anvil clouds will decrease, despite significant differences in their mean I frequency distribution. This agrees with RCEMIP (Sokol et al., 2024) and ICON aquaplanet simulations (Deutloff et al., 2026a), but the magnitude of the change is more than two times higher in the observations. The reduction of tropical anvil clouds is in line with the stability iris theory (Bony et al., 2016) and previous observations of tropical anvil cloud amount changes in response to warming (Saint-Lu et al., 2020).

The feedback from changes in tropical high-cloud frequency is weakly positive since the reduction of thick, cooling clouds is largely cancelled by the reduction of thin, warming clouds. This confirms the result from the RCEMIP simulations (Sokol et al., 2024), while the ICON aquaplanet simulations have a more negative feedback since thin, warming clouds reduce more strongly (Deutloff et al., 2026a). The global feedback from changes in tropical high-cloud frequency derived from the observations is $\lambda = 0.05 \pm 0.01$ W m^{-2} K^{-1}, which is small compared to other cloud feedbacks whose magnitudes range from 0.08 W m^{-2} K^{-1} to 0.25 W m^{-2} K^{-1} (Sherwood et al., 2020).

Our result of a weak positive feedback from changes in tropical high-cloud frequency is in line with other recent studies (Raghuraman et al., 2024; Sokol et al., 2024; Deutloff et al., 2026a; McKim et al., 2024; Wilson Kemsley et al., 2025). The

negative feedback of $-0.2 \pm 0.2\,\mathrm{W\ m^{-2}\ K^{-1}}$ from the WCRP assessment hence seems to be highly unlikely, implying a higher climate sensitivity.

D8 METHODS

D8.1 *Histograms of Ice Water Path*

We calculate histograms of I in the tropics (30°S to 30°N) with 63 bins evenly spaced in log-space from $0.001\ \mathrm{kg\ m^{-2}}$ to $100\ \mathrm{kg\ m^{-2}}$. For all four I retrievals, we calculate the number of occurrences within every I bin for the given month. The number of occurrences in every bin is normalised by the total sample size within the month to calculate $P(I)$ at a monthly timestep. The histograms of $P(I)$ from the simulations are interpolated to the same I bins to ensure comparability.

For 2C-ICE and DARDAR, the sample size is insufficient in some months due to missing data (Fig. D4). We chose a threshold of $1.9 \cdot 10^6$ in sample size. Months with fewer samples are ignored. For 2C-ICE, 50 months (32% of the timeseries) are below the sample size threshold and 28 months (18% of the timeseries) for DARDAR. The magnitude of λ diagnosed from 2C-ICE and DARDAR depends on the threshold in sample size, but not the sign of λ or the pattern of the change in $P(I)$ in response to surface warming.

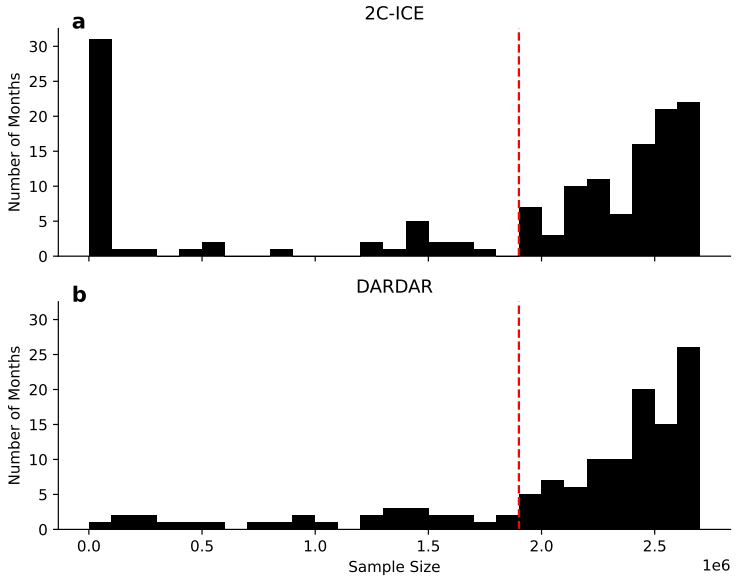


Figure D4: Total sample size within each month for (**a**) 2C-ICE and (**b**) DARDAR. The red dotted line marks the chosen threshold in the sample size. Months with fewer samples are ignored.

D8.2 *Change of Ice Water Path Frequency with Temperature*

As the predictor for changes in $P(I)$ from the observations, we use the tropical mean two-meter-temperature T from ERA5 (Hersbach et al., 2020). We detrend and deseasonalize the monthly timeseries of $P(I)$ from the four I retrievals and T to

isolate ENSO variability. To this end, we subtract the linear trend and the mean seasonal cycle from T and from $P(I)$ in every I bin. The resulting timeseries of $P(I)$ are regressed linearly against T in every I bin. The slope of the linear regression is used as a measure of $\frac{\mathrm{d}P(I)}{\mathrm{d}T}$.

For the ICON aquaplanet simulations (Deutloff et al., 2026a), we calculate $\frac{\mathrm{d}P(I)}{\mathrm{d}T}$ as the difference between $P(I)$ from the control and the warming run, normalised by their mean surface temperature difference. We use the mean $\frac{\mathrm{d}P(I)}{\mathrm{d}T}$ from the $+2\,\mathrm{K}$ and the $+4\,\mathrm{K}$ warming simulation.

For the RCEMIP simulations (Sokol et al., 2024), we calculate the ensemble mean $\frac{\mathrm{d}P(I)}{\mathrm{d}T}$ as the difference between the ensemble mean $P(I)$ at 295 K surface temperature and at 305 K surface temperature, divided by their surface temperature difference.

D8.3 *Feedback*

The feedback from $\frac{\mathrm{d}P(I)}{\mathrm{d}T}$ is calculated with eq. 1. We use $C(I)$ from the ICON aquaplanet control simulation (Deutloff et al., 2026a).

BIBLIOGRAPHY

Amell, A., S. Pfreundschuh, and P. Eriksson (2024). "The Chalmers Cloud Ice Climatology: retrieval implementation and validation." In: *Atmospheric Measurement Techniques* 17.14, pp. 4337–4368. DOI: 10.5194/amt-17-4337-2024.

Arias, P., N. Bellouin, E. Coppola, R. Jones, G. Krinner, J. Marotzke, V. Naik, M. Palmer, G.-K. Plattner, J. Rogelj, et al. (2021). "Technical Summary." In: *Climate Change 2021: The Physical Science Basis. Contribution of Working Group I to the Sixth Assessment Report of the Intergovernmental Panel on Climate Change*. Ed. by V. Masson-Delmotte, P. Zhai, A. Pirani, S. Connors, C. Péan, S. Berger, N. Caud, Y. Chen, L. Goldfarb, M. Gomis, et al. Cambridge, United Kingdom and New York, NY, USA: Cambridge University Press, pp. 33–144. DOI: 10.1017/9781009157896.002.

Arrhenius, S. (1896). "On the influence of carbonic acid in the air upon the temperature of the ground." In: *The London, Edinburgh, and Dublin Philosophical Magazine and Journal of Science* 41.251, pp. 237–276. DOI: 10.1080/14786449608620846.

Atlas, R. L., C. S. Bretherton, A. B. Sokol, P. N. Blossey, and M. F. Khairoutdinov (2024). "Tropical Cirrus Are Highly Sensitive to Ice Microphysics Within a Nudged Global Storm-Resolving Model." In: *Geophysical Research Letters* 51.1, e2023GL105868. DOI: https://doi.org/10.1029/2023GL105868. eprint: https://agupubs.onlinelibrary.wiley.com/doi/pdf/10.1029/2023GL105868.

Baldauf, M., A. Seifert, J. Förstner, D. Majewski, M. Raschendorfer, and T. Reinhardt (2011). "Operational Convective-Scale Numerical Weather Prediction with the COSMO Model: Description and Sensitivities." In: *Monthly Weather Review* 139.12, pp. 3887–3905. DOI: 10.1175/MWR-D-10-05013.1.

Becker, T., P. Bechtold, and I. Sandu (2021). "Characteristics of convective precipitation over tropical Africa in storm-resolving global simulations." In: *Quarterly Journal of the Royal Meteorological Society* 147.741, pp. 4388–4407. DOI: 10.1002/qj.4185.

Beer, C. G., J. Hendricks, and M. Righi (2024). "Impacts of ice-nucleating particles on cirrus clouds and radiation derived from global model simulations with MADE3 in EMAC." In: *Atmospheric Chemistry and Physics* 24.5, pp. 3217–3240. DOI: 10.5194/acp-24-3217-2024.

Bellenger, H., Y. N. Takayabu, T. Ushiyama, and K. Yoneyama (2010). "Role of Diurnal Warm Layers in the Diurnal Cycle of Convection over the Tropical Indian Ocean during MISMO." In: *Monthly Weather Review* 138.6, pp. 2426–2433. DOI: 10.1175/2010MWR3249.1.

Berry, E. and G. G. Mace (2014). "Cloud properties and radiative effects of the Asian summer monsoon derived from A-Train data." In: *Journal of Geophysical Research: Atmospheres* 119.15, pp. 9492–9508. DOI: 10.1002/2014JD021458.

Blackburn, M., D. L. Williamson, K. Nakajima, W. Ohfuchi, Y. O. Takahashi, Y.-Y. Hayashi, H. Nakamura, M. Ishiwatari, J. L. McGregor, H. Borth, et al. (2013). "The Aqua-Planet Experiment (APE): CONTROL SST Simulation." In: *Journal*

of the Meteorological Society of Japan. Ser. II 91A, pp. 17–56. DOI: 10.2151/jmsj.2013-A02.

Bolot, M., L. M. Harris, K.-Y. Cheng, T. M. Merlis, P. N. Blossey, C. S. Bretherton, S. K. Clark, A. Kaltenbaugh, L. Zhou, and S. Fueglistaler (2023). "Kilometer-scale global warming simulations and active sensors reveal changes in tropical deep convection." In: *npj Climate and Atmospheric Science* 6.1, pp. 1–8. DOI: 10.1038/s41612-023-00525-w.

Bony, S., B. Stevens, D. Coppin, T. Becker, K. A. Reed, A. Voigt, and B. Medeiros (2016). "Thermodynamic control of anvil cloud amount." In: *Proceedings of the National Academy of Sciences* 113.32, pp. 8927–8932. DOI: 10.1073/pnas.1601472113.

Brath, M., J. Petersen, S. A. Buehler, and P. Eriksson (2024). *Extending the Atmospheric Radiative Transfer Simulator (Arts) to Shortwave Radiation*. SSRN Scholarly Paper. Rochester, NY. DOI: 10.2139/ssrn.4968132.

Bretherton, C. S., P. N. Blossey, and C. Stan (2014). "Cloud feedbacks on greenhouse warming in the superparameterized climate model SP-CCSM4." In: *Journal of Advances in Modeling Earth Systems* 6.4, pp. 1185–1204. DOI: 10.1002/2014MS000355.

Buehler, S. A., J. Mendrok, P. Eriksson, A. Perrin, R. Larsson, and O. Lemke (2018). "ARTS, the Atmospheric Radiative Transfer Simulator – version 2.2, the planetary toolbox edition." In: *Geoscientific Model Development* 11.4, pp. 1537–1556. DOI: 10.5194/gmd-11-1537-2018.

Cariolle, D. and H. Teyssèdre (2007). "A revised linear ozone photochemistry parameterization for use in transport and general circulation models: multi-annual simulations." In: *Atmospheric Chemistry and Physics* 7.9, pp. 2183–2196. DOI: 10.5194/acp-7-2183-2007.

Cazenave, Q., M. Ceccaldi, J. Delanoë, J. Pelon, S. Groß, and A. Heymsfield (2019). "Evolution of DARDAR-CLOUD ice cloud retrievals: new parameters and impacts on the retrieved microphysical properties." In: *Atmospheric Measurement Techniques* 12.5, pp. 2819–2835. DOI: 10.5194/amt-12-2819-2019.

Ceppi, P., F. Brient, M. D. Zelinka, and D. L. Hartmann (2017). "Cloud feedback mechanisms and their representation in global climate models." In: *WIREs Climate Change* 8.4, e465. DOI: 10.1002/wcc.465.

Charney, J. G. (1963). "A Note on Large-Scale Motions in the Tropics." In: *Journal of the Atmospheric Sciences* 20.6, pp. 607–609. DOI: 10.1175/1520-0469(1963)020<0607:ANOLSM>2.0.CO;2.

Chen, T., J. Ge, C. Zhang, Y. Wu, Q. Mu, X. Han, J. Su, X. Hu, and Z. Zhu (2025). "Shifts in diurnal cycles of low and high clouds warm the climate: evidence from decadal satellite observations." In: *Environmental Research Letters* 20.9, p. 094040. DOI: 10.1088/1748-9326/adf23c.

Chou, M.-D. and R. S. Lindzen (2005). "Comments on "Examination of the Decadal Tropical Mean ERBS Nonscanner Radiation Data for the Iris Hypothesis"." In: *Journal of Climate* 18.12, pp. 2123–2127. DOI: 10.1175/JCLI3406.1.

Christopoulos, C. and T. Schneider (2021). "Assessing Biases and Climate Implications of the Diurnal Precipitation Cycle in Climate Models." In: *Geophysical Research Letters* 48.13, e2021GL093017. DOI: 10.1029/2021GL093017.

Covey, C., P. J. Gleckler, C. Doutriaux, D. N. Williams, A. Dai, J. Fasullo, K. Trenberth, and A. Berg (2016). "Metrics for the Diurnal Cycle of Precipitation: Toward Routine Benchmarks for Climate Models." In: *Journal of Climate* 29.12, pp. 4461–4471. DOI: 10.1175/JCLI-D-15-0664.1.

Delanoë, J. and R. J. Hogan (2010). "Combined CloudSat-CALIPSO-MODIS retrievals of the properties of ice clouds." In: *Journal of Geophysical Research: Atmospheres* 115.D4. DOI: 10.1029/2009JD012346.

Deng, M., G. G. Mace, Z. Wang, and H. Okamoto (2010). "Tropical Composition, Cloud and Climate Coupling Experiment validation for cirrus cloud profiling retrieval using CloudSat radar and CALIPSO lidar." In: *Journal of Geophysical Research: Atmospheres* 115.D10. DOI: 10.1029/2009JD013104.

Deutloff, J. (2024). *Conceptual Model Code and Evaluation Scripts (Version 1.1.0)*. DOI: 10.5281/zenodo.14059493.

— (2026a). *Code to accompany "Facets of the Tropical High-Cloud Feedback in a Global Storm-Resolving Model" by Deutloff et al., 2026.* Version 1.1. DOI: 10.5281/zenodo.17472875.

— (2026b). *Data to accompany "Facets of the Tropical High-Cloud Feedback in a Global Storm-Resolving Model" by Deutloff et al., 2026.* Version 2.0. DOI: 10.5281/zenodo.17472593.

Deutloff, J. and M. Brath (2024). *High-Cloud Radiative Effect Dataset*. DOI: 10.25592/uhhfdm.14753.

Deutloff, J., S. A. Buehler, M. Brath, and A. K. Naumann (2025a). "Insights on Tropical High-Cloud Radiative Effect From a New Conceptual Model." In: *Journal of Advances in Modeling Earth Systems* 17.2, e2024MS004615. DOI: 10.1029/2024MS004615.

Deutloff, J., S. A. Buehler, J. Windmiller, and A. K. Naumann (2026a). "Facets of the Tropical High-Cloud Feedback in a Global Storm-Resolving Model." Preprint, under revision at npj Climate and Atmospheric Science. DOI: 10.21203/rs.3.rs-9133974/v1.

— (2026b). "Observed Diurnal Cycle Change of Tropical Deep Convection Amplifies Surface Warming." Preprint, under revision at Nature Geoscience. DOI: 10.21203/rs.3.rs-9293749/v1.

— (2026c). "Weak Positive Feedback from Observed Reduction of Tropical Anvil Clouds." In preparation.

Deutloff, J., H. Held, and T. M. Lenton (2025b). "High probability of triggering climate tipping points under current policies modestly amplified by Amazon dieback and permafrost thaw." In: *Earth System Dynamics* 16.2, pp. 565–583. DOI: 10.5194/esd-16-565-2025.

Doms, G., J. Förstner, E. Heise, T. Reinhardt, B. Ritter, and R. Schrodin (2021). *A Description of the Nonhydrostatic Regional COSMO-Model*.

Duvel, J. P. (1989). "Convection over Tropical Africa and the Atlantic Ocean during Northern Summer. Part I: Interannual and Diurnal Variations." In: *Monthly Weather Review* 117.12, pp. 2782–2799. DOI: 10.1175/1520-0493(1989)117<2782:COTAAT>2.0.CO;2.

Eliasson, S., S. A. Buehler, M. Milz, P. Eriksson, and V. O. John (2011). "Assessing observed and modelled spatial distributions of ice water path using satellite

data." In: *Atmospheric Chemistry and Physics* 11.1, pp. 375–391. DOI: 10.5194/acp-11-375-2011.

Eriksson, P., A. Baró Pérez, N. Müller, H. Hallborn, E. May, M. Brath, S. A. Buehler, and L. Ickes (2026). "Advancements and continued challenges in observations and global modelling of atmospheric ice mass." In: *Atmospheric Chemistry and Physics* 26.4, pp. 2741–2768. DOI: 10.5194/acp-26-2741-2026.

Eyring, V., S. Bony, G. A. Meehl, C. A. Senior, B. Stevens, R. J. Stouffer, and K. E. Taylor (2016). "Overview of the Coupled Model Intercomparison Project Phase 6 (CMIP6) experimental design and organization." In: *Geoscientific Model Development* 9.5, pp. 1937–1958. DOI: 10.5194/gmd-9-1937-2016.

Feng, J., R. Menzel, and D. Paynter (2025). "Toward Transparency and Consistency: An Open-Source Optics Parameterization for Clouds and Precipitation." In: *Journal of Advances in Modeling Earth Systems* 17.3, e2024MS004478. DOI: 10.1029/2024MS004478.

Feng, Z., L. R. Leung, J. Hardin, C. R. Terai, F. Song, and P. Caldwell (2023). "Mesoscale Convective Systems in DYAMOND Global Convection-Permitting Simulations." In: *Geophysical Research Letters* 50.4, e2022GL102603. DOI: 10.1029/2022GL102603.

Field, P. R., A. J. Heymsfield, and A. Bansemer (2007). "Snow Size Distribution Parameterization for Midlatitude and Tropical Ice Clouds." In: *Journal of the Atmospheric Sciences*. DOI: 10.1175/2007JAS2344.1.

Forster, P., T. Storelvmo, K. Armour, W. Collins, J.-L. Dufresne, D. Frame, D. Lunt, T. Mauritsen, M. Palmer, M. Watanabe, et al. (2021). "The Earth's Energy Budget, Climate Feedbacks, and Climate Sensitivity." In: *Climate Change 2021: The Physical Science Basis. Contribution of Working Group I to the Sixth Assessment Report of the Intergovernmental Panel on Climate Change*. Ed. by V. Masson-Delmotte, P. Zhai, A. Pirani, S. Connors, C. Péan, S. Berger, N. Caud, Y. Chen, L. Goldfarb, M. Gomis, et al. Cambridge, United Kingdom and New York, NY, USA: Cambridge University Press, pp. 923–1054. DOI: 10.1017/9781009157896.009.

Fu, Q., M. Baker, and D. L. Hartmann (2002). "Tropical cirrus and water vapor: an effective Earth infrared iris feedback?" In: *Atmospheric Chemistry and Physics* 2.1, pp. 31–37. DOI: 10.5194/acp-2-31-2002.

Gasparini, B., G. Mandorli, C. Stubenrauch, and A. Voigt (2024). "Basic Physics Predicts Stronger High Cloud Radiative Heating With Warming." In: *Geophysical Research Letters* 51.24, e2024GL111228. DOI: 10.1029/2024GL111228.

Gasparini, B., P. N. Blossey, D. L. Hartmann, G. Lin, and J. Fan (2019). "What Drives the Life Cycle of Tropical Anvil Clouds?" In: *Journal of Advances in Modeling Earth Systems* 11.8, pp. 2586–2605. DOI: 10.1029/2019MS001736.

Gasparini, B., A. B. Sokol, C. J. Wall, D. L. Hartmann, and P. N. Blossey (2022). "Diurnal Differences in Tropical Maritime Anvil Cloud Evolution." In: *Journal of Climate* 35.5, pp. 1655–1677. DOI: 10.1175/JCLI-D-21-0211.1.

Gasparini, B., S. C. Sullivan, A. B. Sokol, B. Kärcher, E. Jensen, and D. L. Hartmann (2023). "Opinion: Tropical cirrus – from micro-scale processes to climate-scale impacts." In: *Atmospheric Chemistry and Physics* 23.24, pp. 15413–15444. DOI: 10.5194/acp-23-15413-2023.

Geer, A. J. and F. Baordo (2014). "Improved scattering radiative transfer for frozen hydrometeors at microwave frequencies." In: *Atmospheric Measurement Techniques* 7.6, pp. 1839–1860. DOI: 10.5194/amt-7-1839-2014.

Geleyn, J. and A. Hollingsworth (1979). "An economical analytical method for the computation of the interaction between scattering and line absorption of radiation." In: *Cont. Atmos. Phys.* 52, pp. 1–16.

Ghil, M. and V. Lucarini (2020). "The physics of climate variability and climate change." In: *Reviews of Modern Physics* 92.3, p. 035002. DOI: 10.1103/RevModPhys.92.035002.

Gray, W. M. and R. W. Jacobson (1977). "Diurnal Variation of Deep Cumulus Convection." In: *Monthly Weather Reviews*.

Hansen, J., A. Lacis, D. Rind, G. Russell, P. Stone, I. Fung, R. Ruedy, and J. Lerner (1984). "Climate Sensitivity: Analysis of Feedback Mechanisms." In: *Climate Processes and Climate Sensitivity*. American Geophysical Union (AGU), pp. 130–163. ISBN: 978-1-118-66603-6. DOI: 10.1029/GM029p0130.

Hartmann, D. L. (2016). "Tropical anvil clouds and climate sensitivity." In: *Proceedings of the National Academy of Sciences* 113.32, pp. 8897–8899. DOI: 10.1073/pnas.1610455113.

Hartmann, D. L., B. D. Dygert, P. N. Blossey, Q. Fu, and A. B. Sokol (2022). "The Vertical Profile of Radiative Cooling and Lapse Rate in a Warming Climate." In: *Journal of Climate* 35.19, pp. 6253–6265. DOI: 10.1175/JCLI-D-21-0861.1.

Hartmann, D. L., B. Gasparini, S. E. Berry, and P. N. Blossey (2018). "The Life Cycle and Net Radiative Effect of Tropical Anvil Clouds." In: *Journal of Advances in Modeling Earth Systems* 10.12, pp. 3012–3029. DOI: 10.1029/2018MS001484.

Hartmann, D. L. and K. Larson (2002). "An important constraint on tropical cloud - climate feedback." In: *Geophysical Research Letters* 29.20, pp. 12–1–12–4. DOI: 10.1029/2002GL015835.

Hartmann, D. L. and M. L. Michelsen (2002). "No Evidence for Iris." In: *Bulletin of the American Meteorological Society* 83.2, pp. 249–254. DOI: 10.1175/1520-0477(2002)083<0249:NEFI>2.3.CO;2.

Haslehner, K., B. Gasparini, and A. Voigt (2024). "Radiative Heating of High-Level Clouds and Its Impacts on Climate." In: *Journal of Geophysical Research: Atmospheres* 129.12, e2024JD040850. DOI: 10.1029/2024JD040850.

Hendon, H. H. and K. Woodberry (1993). "The diurnal cycle of tropical convection." In: *Journal of Geophysical Research: Atmospheres* 98.D9, pp. 16623–16637. DOI: 10.1029/93JD00525.

Hersbach, H., B. Bell, P. Berrisford, S. Hirahara, A. Horányi, J. Muñoz-Sabater, J. Nicolas, C. Peubey, R. Radu, D. Schepers, et al. (2020). "The ERA5 global reanalysis." In: *Quarterly Journal of the Royal Meteorological Society* 146.730, pp. 1999–2049. DOI: 10.1002/qj.3803.

Hohenegger, C., P. Korn, L. Linardakis, R. Redler, R. Schnur, P. Adamidis, J. Bao, S. Bastin, M. Behravesh, M. Bergemann, et al. (2023). "ICON-Sapphire: simulating the components of the Earth system and their interactions at kilometer and subkilometer scales." In: *Geoscientific Model Development* 16.2, pp. 779–811. DOI: 10.5194/gmd-16-779-2023.

Holl, G., S. Eliasson, J. Mendrok, and S. A. Buehler (2014). "SPARE-ICE: Synergistic ice water path from passive operational sensors." In: *Journal of Geophysical Research: Atmospheres* 119.3, pp. 1504–1523. DOI: 10.1002/2013JD020759.

Janowiak, J., B. Joyce, and P. Xie (2017). *NCEP/CPC L3 Half Hourly 4km Global (60S–60N) Merged IR V1*. Ed. by A. Savtchenko. Goddard Earth Sciences Data and Information Services Center (GES DISC), Greenbelt, MD. Accessed: 2026-01-27. DOI: 10.5067/P4HZB9N27EKU.

Janowiak, J. E., R. J. Joyce, and Y. Yarosh (2001). "A Real-Time Global Half-Hourly Pixel-Resolution Infrared Dataset and Its Applications." In: *Bulletin of the American Meteorological Society* 82.2, pp. 205–218. DOI: 10.1175/1520-0477(2001)082<0205:ARTGHH>2.3.CO;2.

Jeevanjee, N. (2022). "Three Rules for the Decrease of Tropical Convection With Global Warming." In: *Journal of Advances in Modeling Earth Systems* 14.11, e2022MS003285. DOI: 10.1029/2022MS003285.

— (2023). "Climate sensitivity from radiative-convective equilibrium: A chalkboard approacha)." In: *American Journal of Physics* 91.9, pp. 731–745. DOI: 10.1119/5.0135727.

Jeevanjee, N. and S. Fueglistaler (2020). "Simple Spectral Models for Atmospheric Radiative Cooling." In: *Journal of the Atmospheric Sciences* 77.2, pp. 479–497. DOI: 10.1175/JAS-D-18-0347.1.

Jeevanjee, N. and D. M. Romps (2018). "Mean precipitation change from a deepening troposphere." In: *Proceedings of the National Academy of Sciences* 115.45, pp. 11465–11470. DOI: 10.1073/pnas.1720683115.

Jenney, A. M., D. A. Randall, and M. D. Branson (2020). "Understanding the Response of Tropical Ascent to Warming Using an Energy Balance Framework." In: *Journal of Advances in Modeling Earth Systems* 12.6, e2020MS002056. DOI: 10.1029/2020MS002056.

Judt, F. and R. Rios-Berrios (2021). "Resolved Convection Improves the Representation of Equatorial Waves and Tropical Rainfall Variability in a Global Nonhydrostatic Model." In: *Geophysical Research Letters* 48.14, e2021GL093265. DOI: 10.1029/2021GL093265.

Kluft, L. (2023). *ICON Monsoon 2.0 Ensemble*.

Kraus, E. B. (1963). "The Diurnal Precipitation Change over the Sea." In: *Journal of the Atmospheric Sciences* 20.6, pp. 551–556. DOI: 10.1175/1520-0469(1963)020<0551:TDPCOT>2.0.CO;2.

L'Ecuyer, T. S., Y. Hang, A. V. Matus, and Z. Wang (2019). "Reassessing the Effect of Cloud Type on Earth's Energy Balance in the Age of Active Spaceborne Observations. Part I: Top of Atmosphere and Surface." In: *Journal of Climate* 32.19, pp. 6197–6217. DOI: 10.1175/JCLI-D-18-0753.1.

Lang, T., A. K. Naumann, B. Stevens, and S. A. Buehler (2021). "Tropical Free-Tropospheric Humidity Differences and Their Effect on the Clear-Sky Radiation Budget in Global Storm-Resolving Models." In: *Journal of Advances in Modeling Earth Systems* 13.11, e2021MS002514. DOI: 10.1029/2021MS002514.

Lin, B., T. Wong, B. A. Wielicki, and Y. Hu (2004). "Examination of the Decadal Tropical Mean ERBS Nonscanner Radiation Data for the Iris Hypothesis." In:

Journal of Climate 17.6, pp. 1239–1246. DOI: 10.1175/1520-0442(2004)017<1239:EOTDTM>2.0.CO;2.

Lindzen, R. S. and Y.-S. Choi (2022). "The Iris Effect: A Review." In: *Asia-Pacific Journal of Atmospheric Sciences* 58.1, pp. 159–168. DOI: 10.1007/s13143-021-00238-1.

Lindzen, R. S., M.-D. Chou, and A. Y. Hou (2001). "Does the Earth Have an Adaptive Infrared Iris?" In: *Bulletin of the American Meteorological Society* 82.3, pp. 417–432. DOI: 10.1175/1520-0477(2001)082<0417:DTEHAA>2.3.CO;2.

— (2002). "Comment on "No Evidence for Iris"." In: *Bulletin of the American Meteorological Society* 83.9, pp. 1345–1349.

Luo, H., J. Quaas, and Y. Han (2024). "Diurnally asymmetric cloud cover trends amplify greenhouse warming." In: *Science Advances* 10.25, eado5179. DOI: 10.1126/sciadv.ado5179.

Mapes, B. E. and R. A. Houze (1993). "Cloud Clusters and Superclusters over the Oceanic Warm Pool." In: *Monthly Weather Review*.

Matus, A. V. and T. S. L'Ecuyer (2017). "The role of cloud phase in Earth's radiation budget." In: *Journal of Geophysical Research: Atmospheres* 122.5, pp. 2559–2578. DOI: 10.1002/2016JD025951.

Mauritsen, T. and B. Stevens (2015). "Missing iris effect as a possible cause of muted hydrological change and high climate sensitivity in models." In: *Nature Geoscience* 8.5, pp. 346–351. DOI: 10.1038/ngeo2414.

McKim, B., S. Bony, and J.-L. Dufresne (2024). "Weak anvil cloud area feedback suggested by physical and observational constraints." In: *Nature Geoscience*, pp. 1–6. DOI: 10.1038/s41561-024-01414-4.

Medeiros, B., B. Stevens, and S. Bony (2015). "Using aquaplanets to understand the robust responses of comprehensive climate models to forcing." In: *Climate Dynamics* 44.7, pp. 1957–1977. DOI: 10.1007/s00382-014-2138-0.

Neale, R. B. and B. J. Hoskins (2000). "A standard test for AGCMs including their physical parametrizations: I: the proposal." In: *Atmospheric Science Letters* 1.2, pp. 101–107. DOI: 10.1006/asle.2000.0022.

Peinado Bravo, A., D. Klocke, and B. Stevens (2026). "Horizontal Grid Spacing Convergence of Aquaplanet Experiments Using a Global-Storm Resolving Model." In: *Journal of Advances in Modeling Earth Systems* 18.2, e2025MS005349. DOI: https://doi.org/10.1029/2025MS005349.

Pfreundschuh, S., J. Kukulies, A. Amell, H. Hallborn, E. May, and P. Eriksson (2025). "The Chalmers Cloud Ice Climatology: A Novel Robust Climate Record of Frozen Cloud Hydrometeor Concentrations." In: *Journal of Geophysical Research: Atmospheres* 130.6, e2024JD042618. DOI: 10.1029/2024JD042618.

Pincus, R., C. Hannay, S. A. Klein, K.-M. Xu, and R. Hemler (2005). "Overlap assumptions for assumed probability distribution function cloud schemes in large-scale models." In: *Journal of Geophysical Research: Atmospheres* 110.D15. DOI: 10.1029/2004JD005100.

Pörtner, H.-O., D. Roberts, H. Adams, I. Adelekan, C. Adler, R. Adrian, P. Aldunce, E. Ali, R. Ara Begum, B. Bednar-Friedl, et al. (2022). "Technical Summary." In: *Climate Change 2022: Impacts, Adaptation and Vulnerability. Contribution of Working Group II to the Sixth Assessment Report of the Intergovernmental*

Panel on Climate Change. Ed. by H. O. Pörtner, D. C. Roberts, M. Tignor, E. S. Poloczanska, K. Mintenbeck, A. Alegría, M. Craig, S. Langsdorf, S. Löschke, V. Möller, et al. Cambridge, UK and New York, NY, USA: Cambridge University Press. DOI: 10.1017/9781009325844.002.

Raghuraman, S. P., B. Medeiros, and A. Gettelman (2024). "Observational Quantification of Tropical High Cloud Changes and Feedbacks." In: *Journal of Geophysical Research: Atmospheres* 129.7, e2023JD039364. DOI: 10.1029/2023JD039364.

Ruppert, J. H. and C. Hohenegger (2018). "Diurnal Circulation Adjustment and Organized Deep Convection." In: *Journal of Climate*. DOI: 10.1175/JCLI-D-17-0693.1.

Ruppert, J. H. and R. H. Johnson (2016). "On the cumulus diurnal cycle over the tropical warm pool." In: *Journal of Advances in Modeling Earth Systems* 8.2, pp. 669–690. DOI: 10.1002/2015MS000610.

Ruprecht, E. and W. M. Gray (1976). "Analysis of satellite-observed tropical cloud clusters.: I. Wind and dynamic fields." In: *Tellus* 28.5. DOI: 10.3402/tellusa.v28i5.11309.

Saint-Lu, M., S. Bony, and J.-L. Dufresne (2020). "Observational Evidence for a Stability Iris Effect in the Tropics." In: *Geophysical Research Letters* 47.14, e2020GL089059. DOI: 10.1029/2020GL089059.

— (2022). "Clear-sky control of anvils in response to increased CO2 or surface warming or volcanic eruptions." In: *npj Climate and Atmospheric Science* 5.1, pp. 1–8. DOI: 10.1038/s41612-022-00304-z.

Sanderson, B. M., C. Piani, W. J. Ingram, D. A. Stone, and M. R. Allen (2008). "Towards constraining climate sensitivity by linear analysis of feedback patterns in thousands of perturbed-physics GCM simulations." In: *Climate Dynamics* 30.2, pp. 175–190. DOI: 10.1007/s00382-007-0280-7.

Satoh, M., B. Stevens, F. Judt, M. Khairoutdinov, S.-J. Lin, W. M. Putman, and P. Düben (2019). "Global Cloud-Resolving Models." In: *Current Climate Change Reports* 5.3, pp. 172–184. DOI: 10.1007/s40641-019-00131-0.

Schär, C., O. Fuhrer, A. Arteaga, N. Ban, C. Charpilloz, S. D. Girolamo, L. Hentgen, T. Hoefler, X. Lapillonne, D. Leutwyler, et al. (2020). "Kilometer-Scale Climate Models: Prospects and Challenges." In: DOI: 10.1175/BAMS-D-18-0167.1.

Segura, H., C. Bayley, R. Fievét, H. Glöckner, M. Günther, L. Kluft, A. K. Naumann, S. Ortega, D. S. Praturi, M. Rixen, et al. (2025a). "A Single Tropical Rainbelt in Global Storm-Resolving Models: The Role of Surface Heat Fluxes Over the Warm Pool." In: *Journal of Advances in Modeling Earth Systems* 17.7, e2024MS004897. DOI: 10.1029/2024MS004897.

Segura, H., X. Pedruzo-Bagazgoitia, P. Weiss, S. K. Müller, T. Rackow, J. Lee, E. Dolores-Tesillos, I. Benedict, M. Aengenheyster, R. Aguridan, et al. (2025b). "nextGEMS: entering the era of kilometer-scale Earth system modeling." In: *Geoscientific Model Development* 18.20, pp. 7735–7761. DOI: 10.5194/gmd-18-7735-2025.

Seidel, S. D. and D. Yang (2022). "Temperatures of Anvil Clouds and Radiative Tropopause in a Wide Array of Cloud-Resolving Simulations." In: DOI: 10.1175/JCLI-D-21-0962.1.

Shaw, T. A. and B. Stevens (2025). "The other climate crisis." In: *Nature* 639.8056, pp. 877–887. DOI: 10.1038/s41586-025-08680-1.

Sherwood, S. C., M. J. Webb, J. D. Annan, K. C. Armour, P. M. Forster, J. C. Hargreaves, G. Hegerl, S. A. Klein, K. D. Marvel, E. J. Rohling, et al. (2020). "An Assessment of Earth's Climate Sensitivity Using Multiple Lines of Evidence." In: *Reviews of Geophysics* 58.4, e2019RG000678. DOI: 10.1029/2019RG000678.

Smagorinsky, J. (1963). "General Circulation Experiments with the Primitive Equations: I. The basic Experiment." In: *Monthly Weather Review* 91.3, pp. 99–164. DOI: 10.1175/1520-0493(1963)091<0099:GCEWTP>2.3.CO;2.

Soden, B. J., A. J. Broccoli, and R. S. Hemler (2004). "On the Use of Cloud Forcing to Estimate Cloud Feedback." In: *Journal of Climate* 17.19, pp. 3661–3665. DOI: 10.1175/1520-0442(2004)017<3661:OTUOCF>2.0.CO;2.

Sokol, A. B. and D. L. Hartmann (2020). "Tropical Anvil Clouds: Radiative Driving Toward a Preferred State." In: *Journal of Geophysical Research: Atmospheres* 125.21, e2020JD033107. DOI: 10.1029/2020JD033107.

Sokol, A. B., C. J. Wall, and D. L. Hartmann (2024). "Greater climate sensitivity implied by anvil cloud thinning." In: *Nature Geoscience*, pp. 1–6. DOI: 10.1038/s41561-024-01420-6.

Song, J., F. Song, Z. Feng, L. R. Leung, C. Li, and L. Wu (2024). "Realistic Precipitation Diurnal Cycle in Global Convection-Permitting Models by Resolving Mesoscale Convective Systems." In: *Geophysical Research Letters* 51.13, e2024GL109945. DOI: 10.1029/2024GL109945.

Stauffer, C. L. and A. A. Wing (2023). "Explicitly Resolved Cloud Feedbacks in the Radiative-Convective Equilibrium Model Intercomparison Project." In: *Journal of Advances in Modeling Earth Systems* 15.11, e2023MS003738. DOI: 10.1029/2023MS003738.

Stephens, G. L., D. G. Vane, R. J. Boain, G. G. Mace, K. Sassen, Z. Wang, A. J. Illingworth, E. J. O'connor, W. B. Rossow, S. L. Durden, et al. (2002). "THE CLOUDSAT MISSION AND THE A-TRAIN." In: DOI: 10.1175/BAMS-83-12-1771.

Stevens, B., C. Acquistapace, A. Hansen, R. Heinze, C. Klinger, D. Klocke, H. Rybka, W. Schubotz, J. Windmiller, P. Adamidis, et al. (2020). "The Added Value of Large-eddy and Storm-resolving Models for Simulating Clouds and Precipitation." In: *Journal of the Meteorological Society of Japan. Ser. II* 98.2, pp. 395–435. DOI: 10.2151/jmsj.2020-021.

Stevens, B. and S. Bony (2013). "What Are Climate Models Missing?" In: *Science* 340.6136, pp. 1053–1054. DOI: 10.1126/science.1237554.

Takasuka, D., M. Satoh, T. Miyakawa, C. Kodama, D. Klocke, B. Stevens, P. L. Vidale, and C. R. Terai (2024). "A protocol and analysis of year-long simulations of global storm-resolving models and beyond." In: *Progress in Earth and Planetary Science* 11.1, p. 66. DOI: 10.1186/s40645-024-00668-1.

Taylor, K. E., R. J. Stouffer, and G. A. Meehl (2012). "An Overview of CMIP5 and the Experiment Design." In: DOI: 10.1175/BAMS-D-11-00094.1.

Turbeville, S. M., J. M. Nugent, T. P. Ackerman, C. S. Bretherton, and P. N. Blossey (2022). "Tropical Cirrus in Global Storm-Resolving Models: 2. Cirrus Life Cy-

cle and Top-of-Atmosphere Radiative Fluxes." In: *Earth and Space Science* 9.2, e2021EA001978. DOI: 10.1029/2021EA001978.

Vaillant de Guélis, T., H. Chepfer, R. Guzman, M. Bonazzola, D. M. Winker, and V. Noel (2018). "Space lidar observations constrain longwave cloud feedback." In: *Scientific Reports* 8.1, p. 16570. DOI: 10.1038/s41598-018-34943-1.

Wall, C. J. and D. L. Hartmann (2018). "Balanced Cloud Radiative Effects Across a Range of Dynamical Conditions Over the Tropical West Pacific." In: *Geophysical Research Letters* 45.20, pp. 11, 490–11, 498. DOI: 10.1029/2018GL080046.

Wetherald, R. T. and S. Manabe (1988). "Cloud Feedback Processes in a General Circulation Model." In: *Journal of the Atmospheric Sciences* 45.8, pp. 1397–1416. DOI: 10.1175/1520-0469(1988)045<1397:CFPIAG>2.0.CO;2.

Wieners, K.-H., T. Rackow, R. Aguridan, T. Becker, S. Beyer, S. K. Cheedela, N.-A. Dreier, J. F. Engels, M. Esch, C. Frauen, et al. (2024). *nextGEMS: Catalogs of full output of the production simulations for ICON and IFS*. Tech. rep. World Data Center for Climate (WDCC) at DKRZ.

Williams, I. N. and R. T. Pierrehumbert (2017). "Observational evidence against strongly stabilizing tropical cloud feedbacks." In: *Geophysical Research Letters* 44.3, pp. 1503–1510. DOI: 10.1002/2016GL072202.

Wilson Kemsley, S., P. Nowack, and P. Ceppi (2025). "Climate Models Underestimate Global Decreases in High-Cloud Amount With Warming." In: *Geophysical Research Letters* 52.7, e2024GL113316. DOI: 10.1029/2024GL113316.

Wing, A. A., K. A. Reed, M. Satoh, B. Stevens, S. Bony, and T. Ohno (2018). "Radiative–convective equilibrium model intercomparison project." In: *Geoscientific Model Development* 11.2, pp. 793–813. DOI: 10.5194/gmd-11-793-2018.

Winker, D. M., J. Pelon, J. A. Coakley, S. A. Ackerman, R. J. Charlson, P. R. Colarco, P. Flamant, Q. Fu, R. M. Hoff, C. Kittaka, et al. (2010). "The CALIPSO Mission: A Global 3D View of Aerosols and Clouds." In: *Bulletin of the American Meteorological Society* 91.9, pp. 1211–1230. DOI: 10.1175/2010BAMS3009.1.

Xu, K.-M. and D. A. Randall (1995). "Impact of Interactive Radiative Transfer on the Macroscopic Behavior of Cumulus Ensembles. Part II: Mechanisms for Cloud-Radiation Interactions." In: *Journal of the Atmospheric Sciences* 52.7, pp. 800–817. DOI: 10.1175/1520-0469(1995)052<0800:IOIRTO>2.0.CO;2.

Yang, G.-Y. and J. Slingo (2001). "The Diurnal Cycle in the Tropics." In: *Monthly Weather Review* 129.4, pp. 784–801. DOI: 10.1175/1520-0493(2001)129<0784:TDCITT>2.0.CO;2.

Yang, S. and E. A. Smith (2006). "Mechanisms for Diurnal Variability of Global Tropical Rainfall Observed from TRMM." In: *Journal of Climate*. DOI: 10.1175/JCLI3883.1.

Zelinka, M. D. and D. L. Hartmann (2010). "Why is longwave cloud feedback positive?" In: *Journal of Geophysical Research: Atmospheres* 115.D16. DOI: 10.1029/2010JD013817.

— (2011). "The observed sensitivity of high clouds to mean surface temperature anomalies in the tropics." In: *Journal of Geophysical Research: Atmospheres* 116.D23. DOI: https://doi.org/10.1029/2011JD016459. eprint: https://agupubs.onlinelibrary.wiley.com/doi/pdf/10.1029/2011JD016459.

Zelinka, M. D., S. A. Klein, and D. L. Hartmann (2012a). "Computing and Partitioning Cloud Feedbacks Using Cloud Property Histograms. Part I: Cloud Radiative Kernels." In: *Journal of Climate* 25.11, pp. 3715–3735. DOI: 10.1175/JCLI-D-11-00248.1.

— (2012b). "Computing and Partitioning Cloud Feedbacks Using Cloud Property Histograms. Part II: Attribution to Changes in Cloud Amount, Altitude, and Optical Depth." In: *Journal of Climate* 25.11, pp. 3736–3754. DOI: 10.1175/JCLI-D-11-00249.1.

Zelinka, M. D., S. A. Klein, Y. Qin, and T. A. Myers (2022). "Evaluating Climate Models' Cloud Feedbacks Against Expert Judgment." In: *Journal of Geophysical Research: Atmospheres* 127.2. DOI: 10.1029/2021JD035198.

Zelinka, M. D., C. Zhou, and S. A. Klein (2016). "Insights from a refined decomposition of cloud feedbacks." In: *Geophysical Research Letters* 43.17, pp. 9259–9269. DOI: 10.1002/2016GL069917.

EIDESSTATTLICHE VERSICHERUNG
DECLARATION ON OATH

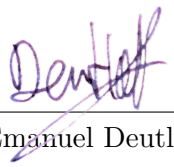
Hiermit erkläre ich an Eides statt, dass ich die vorliegende Dissertationsschrift selbst verfasst und keine anderen als die angegebenen Quellen und Hilfsmittel benutzt habe.

Sofern im Zuge der Erstellung der vorliegenden Dissertationsschrift generative Kuünstliche Intelligenz (gKI) basierte elektronische Hilfsmittel verwendet wurden, versichere ich, dass meine eigene Leistung im Vordergrund stand und dass eine vollständige Dokumentation aller verwendeten Hilfsmittel gemäß der Guten wissenschaftlichen Praxis vorliegt. Ich trage die Verantwortung für eventuell durch die gKI generierte fehlerhafte oder verzerrte Inhalte, fehlerhafte Referenzen, Verstöße gegen das Datenschutz- und Urheberrecht oder Plagiate.

I hereby declare and affirm that this doctoral dissertation is my own work and that I have not used any aids and sources other than those indicated.

If electronic resources based on generative artificial intelligence (gAI) were used in the course of writing this dissertation, I confirm that my own work was the main and value-adding contribution and that complete documentation of all resources used is available in accordance with good scientific practice. I am responsible for any erroneous or distorted content, incorrect references, violations of data protection and copyright law or plagiarism that may have been generated by the gAI.

Hamburg, den 04.05.2026



Jakob Emanuel Deutloff